

NASE Natural Sciences and Engineering Bulletin



e-ISSN: 3023-8293



Journal Owner

Gaziantep University

Editor-in-Chief

Prof. Dr. Çiğdem AYKAÇ
Gaziantep University, Gaziantep, Türkiye
Director of Graduate School of Natural and Applied Sciences
editornase@gaziantep.edu.tr

Associate Editors

Prof. Dr. Tolgay KARA
Gaziantep University, Gaziantep, Türkiye
editoreng@gaziantep.edu.tr

Assoc. Prof. Dr. Mine MENEKŞE YILMAZ
Gaziantep University, Gaziantep, Türkiye
editornat@gaziantep.edu.tr

Language Editor

Prof. Dr. Emrah CİNKARA
Gaziantep University, Gaziantep, Türkiye

Technical and Ethic Editors

Dr. Esra ÜNLÜ
Sibel TUTAR

Section Editors

Prof. Dr. Alkan ALKAYA	Mersin University Electrical and Electronics Engineering
Prof. Dr. Ömer BERKALP	İstanbul Technical University Textile Engineering
Assoc. Prof. Dr. Mehmet BULUT	Cumhuriyet University Department of Machine
Assoc. Prof. Dr. Melik KOYUNCU	Çukurova University Industrial Engineering
Assoc. Prof. Dr. Meriç ŞİMŞEK ASLANOĞLU	Osmaniye Korkut Ata University Food Engineering
Assoc. Prof. Dr. Mustafa SEVİNDİK	Osmaniye Korkut Ata University Department of Biology
Assoc. Prof. Dr. Nihan AKIN SÖNMEZ	Gazi University Department of Photonics
Assoc. Prof. Dr. Selahattin BOZKURT	Uşak University Dept. Medical Services and Techniques
Assoc. Prof. Dr. Semra KAYA	Uşak University Department of Mathematics
Assist. Prof. Dr. Esra Eylem KARATAŞ	Yıldız Technical University Civil Engineering

Scientific Board

Prof. Dr. Ali Fırat ÇABALAR	Gaziantep University Civil Engineering
Prof. Dr. Ali Hussien Mary KİNANİ	University of Baghdad Mechatronics Engineering
Prof. Dr. Ayşegül İYİDOĞAN	Gaziantep University Department of Chemistry
Prof. Dr. Canan CAN	Gaziantep University Department of Biology
Prof. Dr. Deniz ÇEKMECELİOĞLU	Penn State University Agricultural and Biological Engineering
Prof. Dr. Hüseyin TOKTAMIŞ	Gaziantep University Optic Engineering
Prof. Dr. İbrahim BÜYÜKYAZICI	Ankara University Department of Mathematics
Prof. Dr. Osman ERKMEN	İstanbul Arel University Department of Nutrition and Dietetics
Prof. Dr. Ömer EYERCİOĞLU	Gaziantep University Mechanical Engineering
Prof. Dr. Recep YUMRUTAŞ	Gaziantep University Mechanical Engineering
Prof. Dr. Remziye Aysun KEPEKÇİ	Gaziantep University Department of Biology
Prof. Dr. Sedat SAYAR	Mersin University Food Engineering
Prof. Dr. Sema KAYHAN	Gaziantep University Electrical and Electronics Engineering
Prof. Dr. Uğur GÜL	Hacettepe University Department of Mathematics
Assoc. Prof. Dr. Abdul Hafez ABDUL HAFEZ	King Faisal University Department of Computer Science
Assoc. Prof. Dr. Hüseyin YAĞLI	Gaziantep University Mechanical Engineering
Assoc. Prof. Dr. Mustafa Güven GÖK	Gaziantep University Material Science and Engineering
Assist. Prof. Dr. Muhammad Umair KHAN	Pakistan National University of Technology Computer Engineering

EDITORIAL



This new issue of Natural Sciences and Engineering Bulletin (NASE) contains five manuscripts from the disciplines of mathematics, mechanical engineering and electrical and electronics engineering. These manuscripts were first screened using plagiarism prevention software and then reviewed and corrected according to the reviewer's comments. I would like to express my gratitude to all our authors and contributing reviewers of this issue.

It is our great pleasure to welcome the new members of the Section Editors of NASE. We rely on their expertise for reviewing and accepting papers to the journal.

Indexing and abstracting services facilitate the widest dissemination of information by directing researchers to articles relevant to the field. With this issue, we are happy to announce that we were indexed by some multidisciplinary academic databases such as Academindex and Google Scholar.

As the Editor-in-Chief, I would like to express my gratitude to NASE Associate Editors Prof. Dr. Tolgay KARA and Assoc. Prof. Dr. Mine MENEKŞE YILMAZ for their valuable efforts. I would also like to thank Prof. Dr. Emrah CİNKARA, NASE Language Editor, and Dr. Esra ÜNLÜ and Sibel TUTAR, Technical and Ethical Editors, for their valuable contributions.

It's my pleasure to invite the researchers and scientists from all branches of science and engineering to join us by sending their papers for publication in Natural Sciences and Engineering Bulletin.

Prof. Dr. Çiğdem AYKAÇ

Editör-in-Chief

CONTENTS

Research Articles

- 1-9** **Effect of Number of Draw Frame Passages on Rotor-Spun Yarn Quality**
Ali Osman HAN, Halil İbrahim ÇELİK, Gökhan TANDOĞAN
- 10-25** **FFT-based CNN Classification for Schizophrenia Detection in EEG Recordings**
Zekeriya EDAHİL, Sema KOÇ KAYHAN
- 26-55** **Performance Evaluation of Flywheel, Battery and Superconducting Magnetic Energy Storage Systems on Frequency Regulation in the Context of Renewable Energy Integration**
Ahmet Mete Vural, Aliyu Garba Ibrahim
- 56-74** **New Approaches for Evaluation Indeterminate Limits for Multivariable Functions in Undergraduate Mathematics Courses**
Çiğdem DİNÇKAL
- 75-82** **Wear Behaviour of Non-Heat Treated, Hardened and PVD Coated Steel Cams**
Ersin ARSLANBULUT, Burhan SELÇUK

Effect of Number of Draw Frame Passages on Rotor-Spun Yarn Quality

Ali Osman HAN¹, Halil İbrahim ÇELİK^{2*}, Gökhan TANDOĞAN³

Keywords


*Draw frame,
Rotor spun yarn,
Yarn quality,
Abrage*


Abstract –This study investigates the effects of the number of passages for draw frame machines on the quality of rotor-spun yarn. In the presented study, the goal is to produce more cost-effective yarn with similar physical properties to those obtained with two drawing passages by reducing the number of drawing passages. Additionally, the study aims to achieve a lower carbon footprint and reduce the environmental impacts of production processes through lower energy consumption. Yarn samples of Ne 20/1 and Ne 10/1 with the same cotton fibre were produced by means of both single-passage and double-passage drawing machines. The unevenness and tensile properties of the produced yarns were measured using Uster Tester and Uster Tensorapid testing devices, while abrage control was evaluated in an abrage cabinet under ultraviolet light. Furthermore, the energy consumption of the eliminated drawing machine was measured using an energy analyzer. The yarn samples produced with the single passage drawing machine demonstrated better IPI (imperfections) values than those produced with the two-passage system, and the tensile strength values remained at comparable levels. Under UV light, no abrage differences were observed between the yarns from the two different production processes. Energy and raw material waste savings were achieved by eliminating one of the drawing machines. Additionally, considering a waste ratio of 0.6% for a single passage drafting machine, it is estimated that approximately 100 tons of cotton waste per year can be prevented in a rotor-spun facility producing 50 tons of yarn daily. The study revealed that the reduction in raw material and energy consumption enables the production process to be carried out with a lower carbon footprint, thereby making a significant contribution to sustainability. Furthermore, this approach results in a notable reduction in yarn production costs.

1. Introduction

Within the scope of the KYOTO protocol and the Paris Climate Agreement established against global warming, carbon footprint calculation that causes global warming has gained great importance, and carbon footprint evaluation has been made in many areas (Başoğlu et al, 2021). Energy, ecological and Carbon Footprint (CAI) in the textile sector were evaluated in general terms (Bevilacqua et al., 2011). According to the results obtained from the study on carbon footprint in the textile sector, it was observed that the biggest impact on greenhouse gases comes from electricity and thermal energy (Ozcan and Ozturk, 2019). Türkiye's textile industry commands the biggest percentage of the country's GDP and ranks first among all industrial sectors in terms of both production and exports (Evrin and Seyhun, 2022). Energy makes for 6 - 14 % of the sector's overall costs, whereas it accounts for 7.2% of the industry's total consumption (Hoffman, 2011, Maraşlıoğlu, 2018). Within the textile sector, there is a great deal of variation in both goods and process technology. This causes variations in the energy consumption structure and the energy's percentage of overall cost. In spinning-weaving companies, 50% of the energy used is for heat, and 50% is for electricity (Yılmaz, 2010). It is very important to use energy efficiently, especially in Türkiye, which is 70% dependent on foreign sources of energy (Doğan and Yılankırkan, 2015). Energy use is an important parameter that directly affects greenhouse gas emissions. Reducing energy use will play a significant role in reducing both carbon emissions and costs. Since energy is the main input that

¹Gaziantep University, Textile Engineering Department, Engineering Faculty, Gaziantep, Türkiye. E-mail: han@gantep.edu.tr  ORCID: 0009-0009-9143-3269

^{2*}**Corresponding Author.** Gaziantep University, Textile Engineering Department, Engineering Faculty, Gaziantep, Türkiye. E-mail: hcelik@gantep.edu.tr  ORCID: 0000-0002-1145-6471

³KIPAS Mensucat R&D Center, Kahramanmaraş, Türkiye. E-mail: gtandogan@kipas.com.tr  ORCID: 0009-0009-4999-4003

Citation: Han, A. O., Çelik, H. İ., and Tandoğan, G. (2025). Effect of number of draw frame passages on rotor-spun yarn quality. *Natural Sciences and Engineering Bulletin*, 2(1), 1-9.

creates the cost of textile products, studies on reducing energy use or energy recovery have been and are being carried out in every department of textile enterprises (Uçak, 2010).

In textiles, enhancing production efficiency through energy savings and process optimizations by reducing waste rates plays a crucial role in achieving sustainability. Energy is a critical input in all production processes. Improving energy efficiency not only reduces costs but also minimizes environmental impacts. Lower energy consumption contributes to reducing production costs, as well as carbon emissions and greenhouse gas effects, thereby making a positive impact in the fight against climate change. Energy savings in the textile industry are vital for sustainable production and environmental responsibility; through this, both economic and ecological benefits can be achieved, making the future of the textile industry more sustainable. When reviewing the literature, studies generally focus on energy efficiency in textile mills. Efforts have been made to increase efficiency by optimizing production lines. Various parameters of drawing machines, such as gauge settings, draft speeds, coil diameters, and the draft zone of the drawing frame, have been adjusted to examine their effects on the placement of fibers within the yarn diameter and overall yarn quality. Sert et al. (2017) examined various systems to enhance energy efficiency in integrated textile production, including compressed air systems, hotlines and surfaces, lighting systems, ring spinning machines, stenter machines, and steam and hot oil boilers. Şekkeli et al. (2017) implemented a heat recovery system to capture heat from the hot waste air discharged from the chimney of the stenter machine, using the recovered heat to warm the clean cold air, thus achieving a 30% energy saving. Can et al. (1995) concretely demonstrated the economics of heat recovery from waste fluids in textile and similar industries, highlighting the potential energy savings and positive contributions to the economy and environmental benefits in these sectors. In the study conducted by Chaudhari and Raichurkar (2016), the effects of the bottom roller gauge settings of drawing machines on yarn quality were examined. Experiments were carried out using 40/44 mm and 42/46 mm gauge settings in the production of 15 Tex (Ne 40) combed cotton yarn. The findings revealed that yarn defects (thin, thick places, and neps), unevenness (U %), and yarn strength varied depending on the bottom roller gauge settings. The 40/44 mm setting resulted in significant improvements in yarn quality, leading to the conclusion that proper gauge settings are critical for achieving high-quality yarn production. Ishtiaque et al. (2009) studied the effects of high-speed drafting frames and preparatory processes on the packing density and related structural characteristics of ring-spun yarn. The findings show that an increase in drafting speed and coil diameter leads to a reduction in helix twist, helix angle, and helix diameter, which in turn increases yarn packing density. However, an increase in card draft raises the helix twist and angle up to a certain point while reducing the packing density. Additionally, it was found that the packing density in the middle of the fiber was higher, indicating structural consistency. This article emphasizes the importance of process variables in yarn production. In the research carried out by Ramasamy et al. (2019), the modification of the drafting zone settings in the drawing frame was explored to enhance the quality of yarn. The study assesses the impact of various parameters involved in yarn production, particularly focusing on how drafting settings influence yarn quality. The authors noted significant improvements in fiber arrangement, packing density, and mechanical properties resulting from these modifications. The findings highlight the crucial role of optimizing process settings to achieve better yarn quality. This research offers practical strategies aimed at improving quality in yarn production. Kmansuri and Pathak (2022), emphasize the importance of yield percentage in the cotton spinning industry, noting that it directly influences performance and profitability. While the typical yield percentage is around 84%, even a slight increase of 1-2% can lead to significant profit gains. The study presents methodologies to enhance yield percentages, addressing the financial crises many spinning mills face due to their inability to meet quality standards, which adversely affects farmers, workers, and stakeholders in the industry. The research results indicate that ring yarns exhibit greater tenacity than rotor-spun yarns, although their elongation percentage is significantly lower. Additionally, hairiness tests reveal that rotor yarns are less hairy than conventional ring yarns. Ring yarns also show higher unevenness of mass and coefficients of variation compared to rotor yarns. Rotor-spun yarns have established strong applications in woven and knitted fabrics, particularly in home textiles such as terry products and upholstery fabrics, as well as in clothing items like socks and sweaters. Overall, enhancing yield and quality in cotton spinning is crucial for the industry's sustainability and economic impact.

The staple yarn spinning process comprises four critical stages: Blowroom, Carding, Drawing, and Spinning. Each stage plays a vital role in determining the final properties of the yarn, including its strength, uniformity, and

overall quality. Cotton fibers arrive at the spinning mill's blowroom department in the form of bales packaged from the ginning plant. These fibers typically contain 1-15% impurities, which must be removed during processing. In the blowroom, the fibers undergo opening, cleaning, and blending processes to be properly cleaned, separated, and aligned to prepare them for yarn formation. The fibers are then pneumatically transported to the carding machine, where they undergo further opening, cleaning, and carding. The carded fibers are formed into slivers and placed in cans for entry into the drawing machine. The drawing machine is where the processes of doubling (folding the fiber slivers) and drafting (elongating and thinning the fibers) take place. By doubling, a homogeneous mixture is achieved. In the cross-section of the slivers coming from the carding machine, there are approximately 30,000 fibers. The drafting function of the drawing machine is to reduce this number to around 100 fibers, making the slivers thin enough to be suitable for spinning. This function is carried out by rollers in the drawing machine that rotate at different speeds to ensure uniform yarn formation. This is one of the critical tasks performed by the drawing machine, as a thin section in the sliver could result in a very thin and weak area in the final yarn (Elhawary, 2015). In order to reduce similar errors, the use of three-passage drawing frames in spinning methods such as vortex, which utilize long and relatively more costly fibers, demonstrates the significant impact these machines have on quality.

Rotor spinning system is also a spinning system in which more production is taken into account besides quality compared to other spinning systems due to its production method and raw material properties. In the rotor spinning system, the fiber length is limited due to the physical properties of the rotor. The length of the fibers used cannot exceed the rotor diameter for the spinning process to succeed, which leads to the use of shorter fibers in rotor spinning compared to other spinning methods. Since fiber length is one of the important parameters that directly affect yarn quality, yarns produced by the rotor spinning system are of lower quality in terms of physical properties when compared to yarns produced by other spinning systems. This situation is valid not only for the final yarn but also for the intermediate product, the slivers. Controlling shorter fibers is more challenging in mechanical processes compared to longer fibers, which results in slivers produced from the carding machine having more neps and drawing slivers being more uneven. Due to the limited fiber length, machine settings can only optimize the quality up to a certain point. Since the rotor spinning system is known for its production speed, the quantity of production takes precedence over quality expectations. As the last machine before yarn formation, drawing frames, especially in rotor spinning systems, must operate at high speeds to supply the spinning machines ahead of them. As speed increases, fiber control becomes more difficult, leading to lower quality. Therefore, the impact of the drawing frame on yarn quality in rotor spinning is lower than in other spinning systems. Additionally, as the number of fibers in the yarn cross-section increases, fiber control in mechanical processes becomes more challenging, leading to greater mass variation per unit length in thicker yarns compared to finer yarns. In light of this information, the aim is to produce yarn of the same quality in rotor spinning by using a single regulated drawing frame instead of two-passage drawing frames, especially for thick yarns with higher unevenness values. In addition to quality, reducing one machine from the production line will save energy and time, lower yarn production costs, and contribute to sustainability by preventing fiber waste that typically occurs in the first passage drawing frame.

In this study, two different types of yarn, Ne 10/1 and 20/1, were produced as four different samples in a rotor spinning production facility using a two-passage drawing frame and, unlike in the literature, a production line with a single regulated drawing frame. The unevenness and tensile strength values of the produced samples were measured, and their abrade characteristics were examined and compared. The hourly energy consumption of the removed drawing frame was also measured. Thus, the feasibility of production with a lower carbon footprint and reduced energy costs was evaluated.

2. Materials and Methods

The cotton fiber was used as the raw material for the rotor spun yarn samples. The cotton fiber properties, such as average fiber length, strength, elongation percentage, and micronaire value, were measured using the Uster HVI 1000 fiber testing device, and they were determined as 28 mm, 27 g/tex, 6.57%, and 3.47, respectively. The cotton, arriving at the blowroom in bales, went through the Rieter A12 model bale opener, A49 metal detector,

B12 coarse cleaner, B76 mixer, B17 fine cleaner, and Uster Jossy foreign matter detector for opening, cleaning, and blending processes. The cotton fiber was then processed on a Rieter C70 carding machine with a licker-in speed of 1200 rpm, cylinder speed of 780 rpm, flat speed of 0.28 m/min, and an hourly production rate of 105 kg/h, resulting in a Ne 0.080 sliver after the carding process. The card slivers exiting in cans were then connected to the Rieter SB-D 45 first passage drawing frame in the normal production process with a doubling number of 6, draft adjustment of 37/41, and a production speed of 750 m/min, the first passage drawing frame produced slivers at Ne 0.100. These slivers were then connected to the regulated Rieter RSB-D 45 second passage drawing frame with a doubling number of 6, draft settings of 38/42, and a production speed of 750 m/min; sliver samples at Ne 0.100 were prepared by the second passage drawing frame. Using the same raw material and machine settings, sliver samples from the carding machine were directly connected to the second passage drawing frame, creating single-passage drawn sliver samples. The production lines used to prepare the samples are shown in Figure 1.

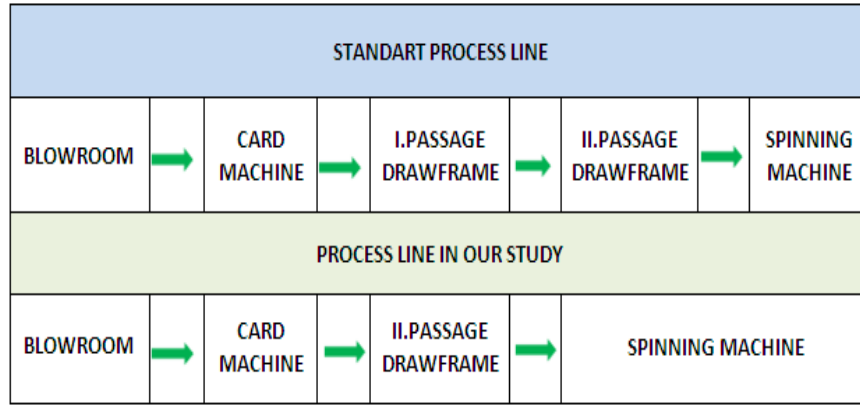


Figure 1. Production lines used in yarn sample production

Four yarn samples with Ne 10/1 and Ne 20/1 yarn counts were produced on the standard process line and study process line by using the same slivers with the parameters in Table 1. Yarn samples were produced with a Saurer Autocore 9 rotor spinning machine with Suessen spinning elements. Spinning elements used for sample production are given in Table 2.

Table 1. Yarn production parameters

Yarn Samples with Single Drawframe					
Sample	Count(Ne)	Twist Per Meter	Twist Coefficient(α)	Rotor Speed (Revolution/Meter)	Production Rate (Meter Per Minute)
1	10	505	4	103.000	204
2	20	860	4.9	146.000	170
Yarn Samples with Double Drawframe					
1	10	505	4	103.000	204
2	20	860	4.9	146.000	170

Table 2. Spinning elements

Sample	Drawframe	Rotor	Opening Roller Solidring	Torque Stop	Navel
Ne 10/1	I. Passage	T 633 BD	B 174 DN	GREEN	KSK4-A
Ne 10/1	II. Passage	T 633 BD	B 174 DN	GREEN	KSK4-A
Ne 20/1	I. Passage	G 628 BD	B 174 DN	GREEN	KSSA
Ne 20/1	II. Passage	G 628 BD	B 174 DN	GREEN	KSSA

The physical properties of yarn samples were measured after production. Yarn count measurements were done according to TS 244 EN ISO 2060 standard. Yarn unevenness measurements were done with Uster Tester 6 test device. Yarn strength measurements were done according to TS EN ISO 2062:2010 standard via Uster Tensorapid 4. Abrage control was made over the yarn bobbins under the UV light. Energy consumption of the eliminated drawframe was measured from energy monitoring system over the machine and calculated for 8 hours.

3. Results and Discussion

Yarn physical test results were given in Table 3 and they were analyzed in Figure 2.

Table 3. Yarn unevenness and tenacity results

Draw Frame	Yarn Count (Ne)	CVm	Thin Places -40%	Thin Places -50%	Thick Places +35%	Thick Places +50%	Neps +140%	Neps +200 %	Neps +280 %	Hairness	Tenacity (Rkm)
Double	10	11.25	8	0	80	3	108	5	0	5.43	12.61
Singe	10	11.00	13	0	70	0	54	0	0	5.43	12.36
Double	20	13.14	131	5	381	24	1046	88	5	4.53	12.47
Single	20	13.00	125	4	368	16	1068	60	4	4.58	12.85

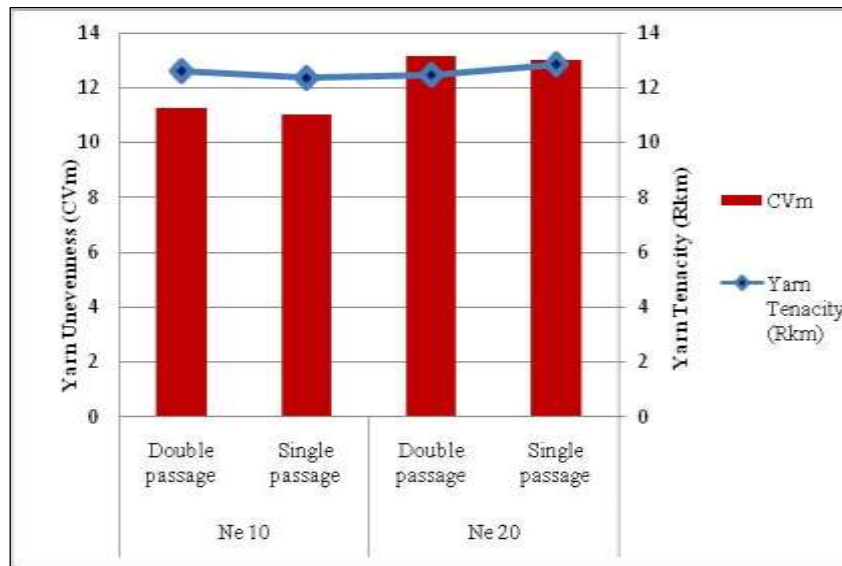


Figure 2. Yarn unevenness and tenacity results

IPI (imperfections) in yarn samples refers to the preference for defects or irregularities. IPI includes thick places, thin places and neps values. When the IPI results of the yarn samples were analyzed (Table 1), it was seen that fewer yarn irregularities were obtained with a single passage draw frame for both yarn counts. As seen from Figure 2, the unevenness values (CVm) of the single and double passage draw frame applications are close to each other for both yarn counts, but the single passage samples have slightly lower CVm values, so they have better yarn quality. The tenacity values are nearly the same and fall within the acceptable standard. Similar to unevenness (CVm) results, the Ne 20/1 yarn sample produced from the study process line has a higher tenacity value according to the double passage sample. Single passage samples for Ne 10/1 have shown slightly less tenacity.

In order to see the effect of passage number and yarn count on yarn tenacity (Rkm) and unevenness (CVm), multivariate analysis (ANOVA) was performed (Table 4). According to the multivariate analysis (ANOVA), it is seen that passage number has no significant effect on yarn tenacity (Rkm) ($p > 0.05$) and no significant effect on yarn unevenness (CVm) ($p < 0.05$). The same results were also obtained for the yarn count parameter.

Table 4. ANOVA results of the production parameters

Tests of Between-Subjects Effects						
Source	Dependent Variable	Type III Sum of Squares	df	Mean Square	F	Sig.
Passage Number	Rkm	0.011	1	0.011	0.308	0.594
	CVm	0.110	1	0.110	11.990	0.009
Yarn Count	Rkm	0.092	1	0.092	2.484	0.154
	CVm	11.310	1	11.310	1230.485	0.000
Passage Number *	Rkm	0.298	1	0.298	8.047	0.022
Yarn Count	CVm	0.009	1	0.009	0.987	0.350
Error	Rkm	0.296	8	0.037		
	CVm	0.074	8	0.009		
Total	Rkm	1898.013	12			
	CVm	1767.97	12			
Corrected Total	Rkm	0.697	11			
	CVm	11.503	11			

a. R Squared = 0.575 (Adjusted R Squared = 0.416)
b. R Squared = 0.994 (Adjusted R Squared = 0.991)

Since there was no significant difference between the two parameters in terms of tensile strength, similar Rkm values were obtained in both passage applications. Considering energy consumption and waste, the use of a single-passage drawing frame can be recommended. In terms of unevenness, as it has a significant effect, it presents a preferable option depending on the passage. As seen from Figure 2, when taking energy savings and waste reduction into account, the unevenness values of the single-passage are better, and the process provides higher quality yarn for both yarn counts.

The values of energy consumption and working conditions are taken by the machine energy monitoring system. This drawframe use 2.63 Kw/h electricity seen in Table 5, for 8 hours (one working shift) if the machine work with 780 rpm speed with 72.3 % efficiency.

Table 5. Energy consumption values of the eliminated drawframe for 8 Hours

Model	Efficiency For 8 Hours (%)	Speed(Rpm)	Output Sliver Number (Ne)	Energy Consumption In %100 Efficiency (Kw/H)
Rieter SB-D 45	72.3	600	0.100	2.63

Ne 10/1 yarn bobbin image under UV light is given in Figure 3. The yarn inside the red circular is produced from a normal process line, which contains a double drawframe and Ne 10/1 yarn. Outside of the red circular is the Ne 10/1 yarn produced from the study process line. It is obviously seen in Figure 3 that there is no abrage between the yarns

from two different process lines.

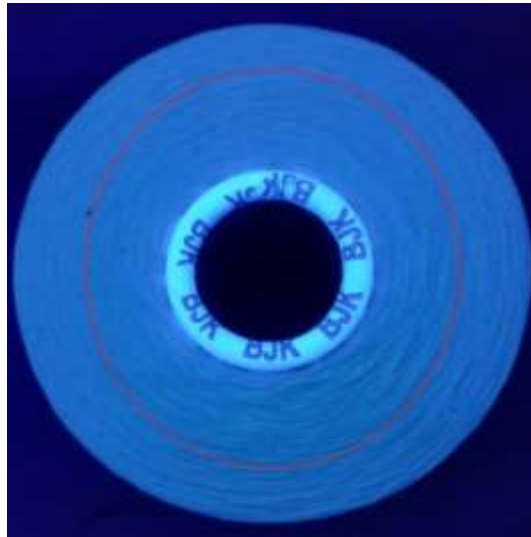


Figure 3. Image of the Ne 10/1 yarn bobbin under UV light

Ne 20/1 yarn bobbin image under UV light is given in Figure 4. The yarn inside the red circular produced from normal process line which contains double drawframe also Ne 20/1 yarn. Outside of the red circular is the Ne 20/1 yarn produced from study process line. It is obviously seen in Figure 4 that there is no abrage between the yarns from two different process line.

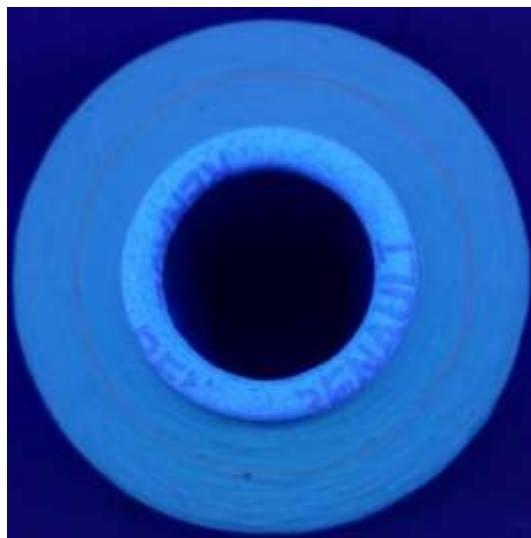


Figure 4. Image of the Ne 20/1 yarn bobbin under UV light

4. Conclusion

According to the European Green Deal announced in 2019 and European Union strategies for reducing greenhouse gas emissions and being carbon neutral, manufacturing enterprises need to follow strategies that will reduce carbon emissions in a short time. Energy is one of the big parameters that affect carbon emissions. This study aims to reduce carbon emissions by targeting energy saving by making process improvements. Furthermore, working with fewer machines means less waste. Saving raw materials significantly contributes to sustainability.

In this study, a machine used in the yarn production process was removed from the production line, and the settings of the other machines were optimized to produce the same quality yarn. At the same time, thanks to the machine removed from the production line, energy saved, waste material prevented and carbon emissions were reduced compared to standard production. The produced yarn was compared with the yarn properties produced in the standard process in terms of evenness and strength. Considering both test results, the yarns produced in the study gave better results in many respects. Based on the results of the multivariate analysis (ANOVA), the passage number has a major influence on unevenness but no significant effect on yarn tenacity. For the yarn number parameter, the same outcomes were likewise observed. Similar tenacity values were found in both passage applications because the two parameters' tensile strengths did not differ significantly. It may be advised to utilize a single-passage drawing frame in regard to waste and energy usage. It offers a better choice in terms of unevenness, depending on the passage, because it has significant consequences. Since the machine removed from production has an important role in the raw material mixture, the yarn produced as a result of the study was checked under UV light to see if there was a problem in terms of the mixture, and it was observed that the yarn produced in the study has no difference from the yarn produced in the normal process. Owing to the machine being removed from the production line, 2.63 kW of energy was saved in 1 hour and approximately 1800 kW in 1 month. Considering that there is an approximate use of between 40-50 of these machines in a rotor spinning mill with an average daily production of 60-70 tons, the amount of energy that will be saved is significant. Saving this amount of energy will help reduce serious carbon emissions. When the operational data for the eliminated drawing frame were examined, the calculated waste amount was 0.6%. Considering this, for a facility producing 60-70 tons of yarn daily, the amount of cotton saved from being wasted annually is approximately 4 tons.

Ethics Permissions

This paper does not require ethics committee approval.

Conflict of Interest

Authors declare that there is no conflict of interest for this paper.

Authors Contribution

Methodology, investigation and supervision were made by the author Halil İbrahim ÇELİK. Data curation, formal analysis, investigation and writing were made by the author Ali Osman HAN. Raw material supply, yarn production and performance tests were done by Gökhan TANDOĞAN.

References

- Baçoğlu, Y., Göksu, T. T., and Baran, M. F. (2021). Bir tekstil fabrikasının karbon ayak izinin değerlendirilmesi. *Avrupa Bilim ve Teknoloji Dergisi*, Ejosat 2021 Ek Sayı 1, 146-150.
- Bevilacqua, M., Ciarapica, F. E., Giacchetta, G., and Marchetti, B. (2011). A carbon footprint analysis in the textile supply chain. *International Journal of Sustainable Engineering*, 4(1), 24-36.
- Can, M. (1995). Endüstriyel atık akışkanların değerlendirilmesi ve ülke ekonomisine katkısı. *Ekoloji Dergisi*, Ekim, Kasım, Aralık, Sayı: 17.
- Chaudhari, V., and Raichurkar, P. P. (2016). Effect of draw frame bottom roller gauge setting on yarn quality. *International Journal on Textile Engineering and Processes*, 2(2), 29-30.
- Doğan, H., and Yılankırkan, N. (2015). Türkiye' nin enerji verimliliği potansiyeli ve projeksiyonu. *Gazi Üniversitesi Fen Bilimleri Dergisi*. Part: C, 375-383.
- Elhawary, I. A. (2015). Fibre to yarn: Staple-yarn spinning. In R. Sinclair (Ed.), *Textiles and Fashion* (pp. 191-212). Woodhead Publishing.
- Evrin, İ. E., and Seyhun, Ö. K. (2022). Sınırdaki karbon düzenleme mekanizması ve Türkiye' nin ihracatına olası etkileri. *Ege Stratejik Araştırmalar Dergisi*, 13(1), 1-13.
- Hoffman, A. J. (2011). The culture and discourse of climate skepticism. *Strategic Organization*, 9(1), 77-84.
- Ishtiaque, S. M., Mukhopadhyay, A., and Kumar, A. (2009). Impact of high-speed draw frame and its preparatory on packing and

related characteristics of ring spun yarn. *The Journal of the Textile Institute*, 100(8), 657-667.

Kmansuri, A., and Pathak, R. (2022). Yield and quality improvement of Asian spinning mill. *International Journal of Mechanical Engineering*, 7(4), 1-8. ISSN: 0974-5823.

Maraşlıoğlu, B. (2018). *Open-end İplik Tesislerinde Enerji Kalitesinin İncelenmesi*. (Master's Thesis) Kahramanmaraş Sütçü İmam Üniversitesi Fen Bilimleri Enstitüsü, Kahramanmaraş, Türkiye.

Ozcan, B., and Ozturk, I. (2019). Renewable energy consumption-economic growth nexus in emerging countries: A bootstrap panel causality test. *Renewable and Sustainable Energy Reviews*, 104, 30-37.

Ramasamy, K. M., Duraisamy, R., and Mammo, H. (2019). Improving yarn quality by modification on drafting zone settings of draw frame. *International Journal of Engineering Trends and Technology*, 67(11), 226-231.

Sert, M. Ö., Eyidoğan, M., Kiliç, F. Ç., and Kaya, D. (2017). *Bir Entegre Tekstil Üretim İşletmesinde Enerji Verimliliği Çalışması*, 1st International Conference on Energy Systems Engineering (pp. 246-250).

Şekkeli, M. and Keçecioglu, Ö. F. (2012). Scada Based an Energy Saving Approach to Operation of Stenter Machine in a Textile Plant Using Waste Heat Recovery System. *Journal of Textile & Apparel/Tekstil ve Konfeksiyon*, 22(3), 248-257.

Uçak, F. (2010). *Tekstil terbiye işletmelerinde ramöz makinasında enerji tasarrufu*. (Master's Thesis) Çukurova Üniversitesi Fen Bilimleri Enstitüsü, Adana, Türkiye.

Yılmaz, S. (2010). *Tekstil kurutma makinelerinin enerji verimliliğinin artırılması*. (Master's Thesis) Uludağ Üniversitesi Fen Bilimleri Enstitüsü, Bursa, Türkiye.

FFT-based CNN Classification for Schizophrenia Detection in EEG Recordings

Zekeriya EDAHIL^{1*}, Sema KOÇ KAYHAN²

Keywords

CNN,
EEG,
Schizophrenia,
FFT,
Classification

Abstract – Machine learning enhances computer-aided medical diagnosis by enabling accurate and swift decision-making. This study proposes a method for detecting schizophrenia (SZ) using electroencephalography, which measures brain electrical activity to diagnose neurological disorders. Schizophrenia is characterized by complex neural patterns, challenging to identify with traditional methods. This research employs deep learning algorithms to analyze EEG signals for schizophrenia detection, aiming to improve classification accuracy. The methodology involves preprocessing Electroencephalography (EEG) time series to extract spectral power features using Fast Fourier Transformation (FFT), which transforms time-domain signals into the frequency domain, revealing brain oscillatory activity. These features are converted into RGB images representing brain activity's spatial information. A convolutional neural network (CNN) is then used to classify these images. The proposed method achieved an average accuracy of 95.97% with FFT, indicating that FFT-based features are highly effective for classification in this context. The results underscore the importance of data representation when using CNN models for EEG signal analysis.

1. Introduction

EEG is a non-invasive diagnostic tool that records brain electrical activity through electrodes placed on the scalp (Figure 1). EEG captures continuous time-series data generated by synaptic currents, reflecting brain communication networks. The method relies on detecting voltage differences between electrodes and visualizing these patterns to assess brain function.

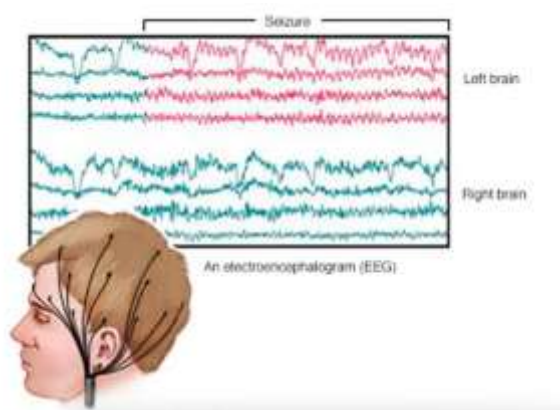




Figure 1. Electroencephalogram (EEG) brain activity

The standardized International 10–20 system ensures consistent electrode placement for data collection during EEG studies (Figure 2). This system correlates electrode positions with specific brain regions like the frontal, temporal, and occipital lobes, ensuring reliability in clinical and research applications (Oostenveld and Praamstra, 2001).

^{1*} **Corresponding Author.** Gaziantep University, Graduate School of Natural and Applied Sciences, Department of Electrical and Electronics Engineering, Division of Computer Science, Türkiye. E-mail: zekeriyaedahil@gmail.com  ORCID: 0009-0002-2297-5100

² Gaziantep University, Faculty of Engineering, Department of Electrical and Electronics Engineering, Division of Computer Science, Türkiye. E-mail: skoc@gantep.edu.tr  ORCID: 0000-0002-8129-7672

Citation: Edahil, Z., and Koç Kayhan, S. (2025). FFT-based CNN classification for schizophrenia detection in EEG recordings. *Natural Sciences and Engineering Bulletin*, 2(1), 10-25.



Figure 2. The 10-20 electrode placement system

EEG plays a vital role in the early detection of brain disorders due to its exceptional temporal resolution, surpassing techniques like fMRI in capturing rapid changes in brain activity. Its non-invasive approach, cost-effectiveness, and ability to track electrical patterns in real-time make it especially valuable for identifying abnormalities associated with conditions such as schizophrenia. Although imaging methods like MRI and CT provide detailed spatial data, they lack EEG's capability to continuously monitor brain activity, which is crucial for diagnosing a wide range of neurological disorders across different levels of consciousness (Niedermeyer and Lopez de Silva, 2005).

EEG offers high temporal resolution, making it ideal for capturing dynamic brain activity in real-time, which is particularly valuable for studying cognitive processes and diagnosing neurological disorders. Its cost-effectiveness and non-invasive nature make it accessible for clinical and research applications, especially in psychiatric conditions like schizophrenia. However, EEG has limitations, including low spatial resolution compared to techniques like fMRI and susceptibility to noise and artifacts, requiring rigorous preprocessing. Despite these challenges, EEG remains a powerful tool for understanding brain dynamics and developing diagnostic frameworks (Kwon and Carpenter., 2007).

SZ is a serious neuropsychiatric disorder characterized by disruptions in thought, emotion, and behavior, leading to psychosis, cognitive deficits, and impaired social functioning. Affecting approximately 24 million people globally, or 0.32% of the population, it typically emerges in late adolescence or early adulthood, with a higher incidence in males. Patients with schizophrenia face a 2-3 times higher mortality rate than that of healthy individuals due to preventable physical conditions like cardiovascular and metabolic diseases (Harrison et al., 2001). The disorder's widespread personal, social, and economic impact underscores the need for effective strategies to mitigate its challenges.

Schizophrenia presents a range of symptoms, disrupting both cognitive and perceptual functions. It includes positive symptoms like hallucinations and delusions, and negative symptoms such as emotional flatness and social withdrawal. Disorganized thoughts, impaired memory, and difficulty with attention are also typical. While some patients experience periods of remission, others face a decline in functioning, emphasizing the importance of early diagnosis and intervention. Common symptoms include disorganized thought processes, social withdrawal, cognitive impairments, and challenges in self-assessment (Harrison et al., 2001).

Schizophrenia is a complex neuropsychiatric disorder characterized by positive symptoms like hallucinations and delusions, and negative symptoms such as emotional withdrawal and cognitive impairments (Figure 3). Diagnosis primarily relies on clinical evaluations of symptoms, which can be subjective and prone to bias, highlighting the need for objective tools like EEG. Early intervention is critical, as addressing the disorder during its initial stages can significantly improve long-term outcomes and reduce residual disabilities (Harm et al., 2013).

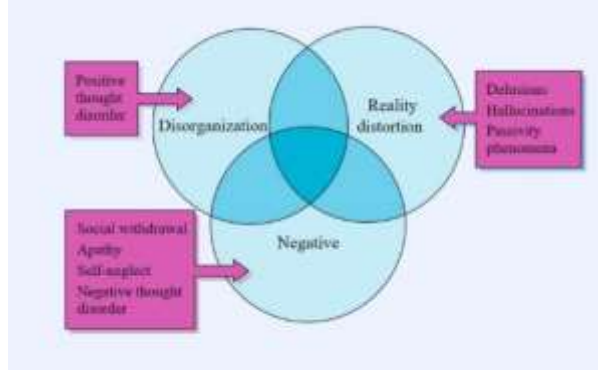


Figure 3. Syndromes of schizophrenia

The treatment of schizophrenia requires a comprehensive approach that combines medication to address neurochemical imbalances with additional therapies aimed at enhancing psychosocial skills. Despite available treatments, there are notable gaps in mental healthcare provision, especially in community settings. Institutional care often falls short in meeting the holistic needs of individuals with schizophrenia, highlighting the need for a shift towards community-based mental health services. Such services should integrate primary care, community mental health centers, housing and employment support, and outreach initiatives for in-home care. Active participation from patients, their families, and communities is essential in promoting recovery-focused care, where individuals are encouraged to take an active role in their treatment (World Health Organization, 2023).

The World Health Organization asserts that schizophrenia is manageable but acknowledges the heavy burden of prolonged treatment on healthcare systems and families. Early diagnosis and intervention play a crucial role in improving outcomes, as addressing schizophrenia at its onset can significantly reduce long-term impairments. Preventive early intervention strategies focus on engaging individuals during their first episode of psychosis, which is vital for slowing disease progression and mitigating residual disabilities. Effective early-stage interventions should include public education, streamlined referral processes from primary care, and efforts to combat stigma and discrimination, which often delay access to care (World Health Organization, 2023).

Managing schizophrenia goes beyond clinical care, requiring sustained support from mental health services, families, and communities. A holistic treatment strategy involving assisted living, employment opportunities, and supported housing is essential not only for improving the quality of life for those affected but also for fostering societal integration and reducing dependency on caregivers. This multidimensional approach emphasizes the need for a treatment plan that addresses both the medical and socio-economic challenges faced by individuals with schizophrenia (Jaeschke et al., 2021).

In the medical field, disease diagnosis generally relies on laboratory tests, biomarkers, and imaging techniques. However, for psychiatric disorders, the diagnostic process is primarily based on patient interviews, observed symptoms, and behavioral indicators (Savio et al., 2010). Traditionally, diagnosing schizophrenia has depended heavily on qualitative assessments like psychiatric history, current symptoms, and behavioral evaluations. However, these methods can be subjective, imprecise, and susceptible to bias, making the diagnostic process time-consuming and potentially unreliable. This has driven interest in more objective tools, such as neuroimaging and EEG, to enhance diagnostic accuracy for schizophrenia.

This study introduces a novel approach for schizophrenia detection using EEG signals, leveraging FFT for feature extraction and CNNs for classification. Spectral power features extracted via FFT are transformed into RGB images, preserving spatial representations of brain activity. These images are then classified using a CNN to achieve high diagnostic accuracy. The proposed method demonstrates a significant improvement in schizophrenia detection, achieving an average accuracy of 95.97%, and highlights the critical role of effective data representation in enhancing CNN-based EEG signal analysis.

2. Literature Review

Between 1993 and 2018, 184 studies were published, with 37 specifically focused on schizophrenia (Table 1). Among these studies, EEG recordings with eyes closed were prevalent, constituting 92% of the cases. The average

age of participants was 31 years, with females representing 33% of the sample. The median number of participants was 63, with a control group included in 54% of the studies. This body of research highlights common practices and methodologies in analyzing EEG signals in schizophrenia research (Newson and Thiagarajan, 2019).

Table 1. Overview of 184 Studies on Various Disorders (1993-2018) Highlighting 37 Schizophrenia Studies with Predominantly Eyes-Closed EEG Recordings

	No. of studies	Median N	% Controls	Average age (years)	% Females	% Eyes closed
ADHD (children)	56	76	45	11	25	75
ADHD (adults)	14	55.5	50	33	43	54
Schizophrenia	37	63	54	31	33	92
ASD/Autism	16	56	52	8.5	21	33
Depression	18	55	44	39	57	86
OCD	10	61.5	49	32	56	100
PTSD	13	74	50	40	37	67
Addiction	16	45	49	33	30	88
Panic disorder	4	79	44	35	69	50
Bipolar disorder	6	99.5	55	30	55	50
Anxiety	3	50	50	31	76	50

Deep learning distinguishes itself from traditional machine learning (ML) by eliminating the necessity for manual feature engineering, as models autonomously develop optimal features during the learning process. Unlike traditional ML, which involves multiple preliminary steps, deep learning integrates learning and classification into a single progression. This approach allows for adaptability to various data types through techniques like transfer learning.

While basic neural networks can approximate underlying truths, the inclusion of additional hidden layers refines models, enhancing accuracy. Despite its computational intensity and the need for large datasets, deep learning's challenges are sometimes alleviated by transfer learning, where pre-trained models on large datasets are adapted to classify new, limited data. This adaptability makes deep learning increasingly significant in medical and healthcare applications, including mental health and neuroimaging (Sharma et al., 2023).

The dynamic and transient nature of EEG signals necessitates sophisticated feature extraction methods for effective analysis. Machine learning techniques, including algorithms like Support Vector Machine (SVM), Linear Discriminant Analysis (LDA), and Adaptive Boosting (AdaBoost), must be paired with robust feature extraction practices. However, extracting nonlinear features from these signals, whether in the time or frequency domain, is intricate and labor-intensive. Such complexity renders conventional machine learning strategies less viable for processing extensive data from EEG signals for the timely identification of schizophrenia in patients (Upadhyay et al., 2015).

In the pursuit of utilizing EEG signals for schizophrenia diagnosis, various machine learning approaches have been adopted to distinguish between affected individuals and healthy controls. Techniques ranging from k-means clustering for grouping similar data points to spectral analysis for identifying characteristic signal patterns have been instrumental. Investigations into the alpha and gamma frequency bands offer insights into the disorder's pathophysiology and treatment response (Chen Z et al., 2019).

In the current landscape, deep learning (DL) strategies are increasingly preferred over conventional ML methods. DL models efficiently process large EEG datasets, making them suitable for real-time applications in clinical settings, including portable devices and hospital environments. Key deep learning models in this domain include CNNs, recurrent neural networks (RNNs), long short-term memory networks (LSTM), gated recurrent units (GRU), and autoencoder architectures (Figure 4).

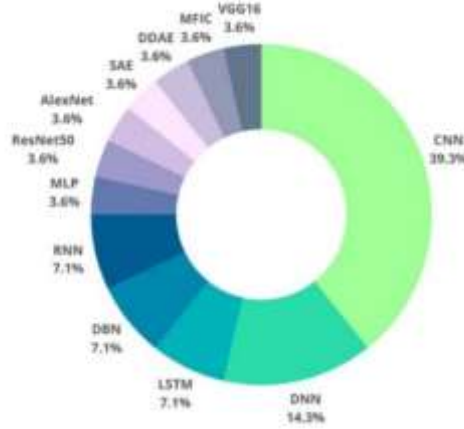


Figure 4. Different deep learning methods that are used by schizophrenia detection studies between (2016-2022)

Deep learning diverges from traditional ML by eliminating the need for manual feature engineering, with models instead developing optimal features autonomously through the learning process. This unified approach encompasses learning and classification in a singular progression, in contrast to the multiple preliminary steps required by traditional ML. Deep learning models can also adapt to a variety of data types through transfer learning. While simple neural networks can approximate underlying truths, incorporating additional hidden layers fine-tunes the models, enhancing precision. However, deep learning's computational demands are considerable, and it often necessitates substantial datasets for training, which can be scarce. This challenge is sometimes mitigated through transfer learning, leveraging models pre-trained on large datasets to categorize new, limited data. Hence, deep learning's versatility enables the automatic extraction of features across numerous applications, marking its rising significance in medical and healthcare domains, including mental health disorders and neuroimaging (Sharma et al., 2023).

The integration of machine learning in neuroimaging presents the opportunity to analyze complex neurological functions and decipher the pathophysiology of disorders like schizophrenia. Traditional ML, coupled with advanced feature extraction, has paved the way for analyzing the complexities of EEG signals. Recently, deep learning algorithms have demonstrated their superiority in medical imaging and signal processing, often outperforming established ML methods (Min et al., 2017). While deep learning models can excel with large datasets, they remain less explored in neuroimaging due to the typically smaller sample sizes. However, studies employing Deep Belief Networks (DBN) and CNNs have shown promising results in extracting meaningful information from EEG data, even with moderate dataset sizes (Plis et al., 2014). These studies suggest the potential advantages of deep learning in neuroimaging despite the absence of vast datasets (Figure 5). Yet, there is a need for models that can preserve the intricate spatial, temporal, and frequency structures inherent in EEG data, an area not fully explored in previous research.

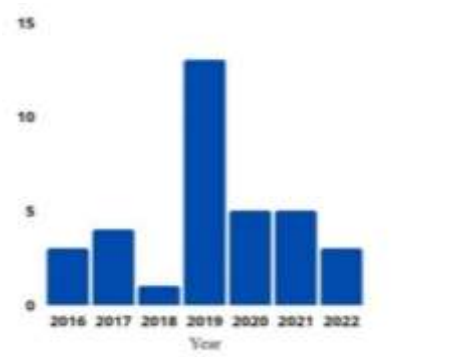


Figure 5. Annual distribution of 34 (25 involving DL, 9 involving combined DL and ML) EEG studies utilizing DL & ML for schizophrenia detection (Sharma et al., 2023).

Several studies using the NNCI dataset (45 schizophrenia cases, 39 healthy controls) have demonstrated the

effectiveness of deep learning models for schizophrenia diagnosis (Table 2). A CNN model with a Softmax classifier achieved 90% accuracy, while a CNN-LSTM hybrid model reached 98.56% accuracy using a Sigmoid classifier. Another approach utilizing DBN with a Softmax classifier reported 95% accuracy. These results highlight the effectiveness of the NNCI dataset in supporting the development of high-performing deep learning models for schizophrenia diagnosis.

Table 2. Comparison of other works in diagnosis of schizophrenia that used NNCI dataset

Work	Dataset	Methodology	Classifier	% Accuracy
“Classification of people who suffer schizophrenia and healthy people by EEG signals using deep learning” (Naira and Alamo, 2019)	NNCI	CNN	Softmax	90.00
“Classification of EEG-based effective brain connectivity in schizophrenia using deep neural networks” (Phang et al., 2019)		DBN	Softmax	93.06
“Spectral features based convolutional neural network for accurate and prompt identification of schizophrenic patients” (Singh et al., 2021)		CNN-LSTM	Sigmoid	94.08

3. Materials and Methods

3.1. Data collection and preprocessing

The study utilized EEG recordings from 84 adolescents (mean age 12.3 years), divided into two groups: healthy individuals (n=39) and those exhibiting schizophrenia symptoms (n=45). The data, hosted by the Laboratory for Neurophysiology and Neuro-Computer Interfaces (NNCI) at Lomonosov Moscow State University, consists of one-minute EEG recordings captured across 16 channels at a sampling rate of 128 Hz, following the traditional 10/20 electrode placement system (Figure 6) (Gorbachevskaya and Borisov, 2019). The recordings, free from psychoactive medication influence, were taken during a resting state with eyes closed. Diagnoses were confirmed using ICD-10 criteria at the Research Center for Psychological Disorders of the Russian Academy of Medical Sciences. This dataset, meticulously compiled and prepared by Prof. N.N. Gorbachevskaya and Borisov, supports the exploration of EEG patterns for schizophrenia diagnosis in adolescents, aiding in mental health research (Bonita et al., 2014).

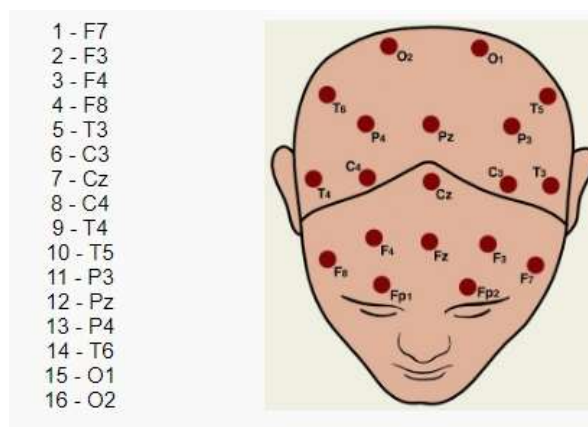


Figure 6. The topographical positions of the 16 channels

Data preprocessing in EEG analysis is a vital process that prepares raw EEG signals for in-depth examination, ensuring the data is clean and reliable for further analysis. The process begins by importing raw EEG data into specialized software tools like MATLAB's EEGLab, Brainstorm, FieldTrip, or MNE-Python, which also incorporate EEG electrode placement information. Preprocessing addresses the susceptibility of EEG signals to various forms of

noise and artifacts, crucially improving the signal-to-noise ratio and accurately reflecting brain activity, which is foundational for extracting meaningful insights from EEG recordings (Figure 7).

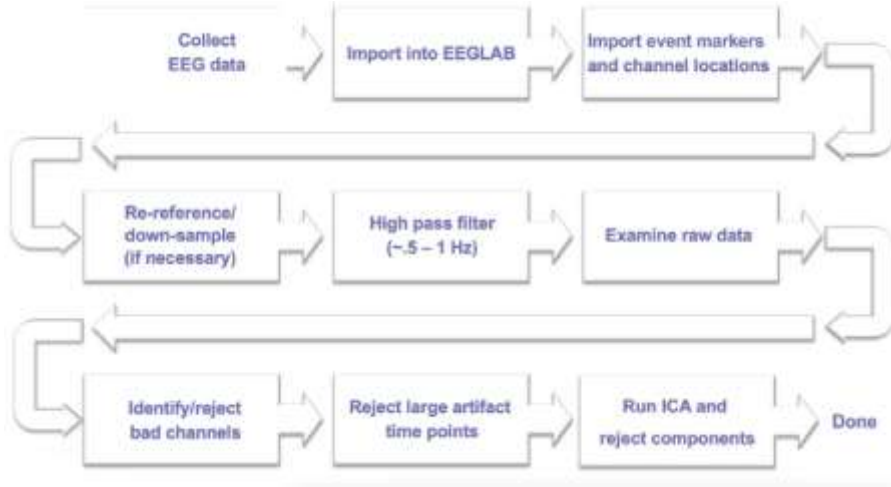


Figure 7. Pre-Processing pipeline in EEGLab (Delorme, 2019)

3.1.1. Filtering and artifact rejection

Filtering and artifact rejection are essential steps in EEG data preprocessing that significantly improve signal quality. A Band-Pass Filter, specifically a second-order Infinite Impulse Response (IIR) Butterworth filter, is applied to allow frequencies between 0.1 Hz and 64 Hz while attenuating those outside this range (Figure 8). Additionally, artifacts—unwanted signals not originating from cerebral activity—are manually identified and removed from each recording. This combination of filtering and artifact rejection minimizes external interference, producing cleaner EEG data that more accurately represents brain function.

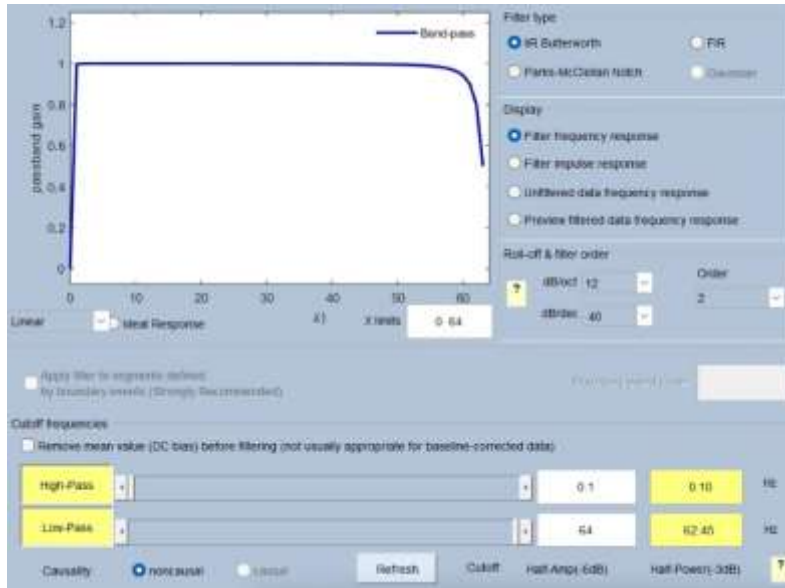


Figure 8. Infinite impulse response (IIR) butterworth filter of the 2nd order

3.1.2. Noise removal and signal enhancement

Noise removal and signal enhancement involve advanced techniques to clarify the recorded EEG signals. Independent Component Analysis (ICA) is a key computational method used to separate multivariate signals into independent components, allowing for the identification and exclusion of noise or artifacts. ICA is particularly useful for signals with a low signal-to-noise ratio, ensuring that the true neurological signals are not obscured. By enhancing the signal quality, ICA plays a critical role in preparing EEG data for detailed analysis (Ganesh and Kumar, 2011).

The integration of Bandpass Filters and ICA in EEG preprocessing exemplifies a strategic approach to refining and analyzing neurological signals. The Butterworth filter, known for its flat frequency response and sharp cutoffs, maintains the integrity of the desired frequencies while eliminating interference. In conjunction with ICA, which removes non-brain components based on their statistical independence, this synergy ensures that EEG signals are thoroughly prepared for accurate and insightful analysis, enhancing the reliability and depth of neurological studies (Kingphai and Moshfeghi, 2021).

3.2. Features extraction

FFT is a powerful algorithm for converting time-domain EEG signals into the frequency domain, helping to reveal relationships between frequencies and amplitudes. It computes the power spectrum, segmenting EEG data into major frequency bands—theta, alpha, beta and integrates spatial measurements from electrodes, producing a multidimensional feature vector essential for understanding brain functions and diagnosing disorders like schizophrenia (Sun et al., 2021).

FFT is preferred over the Discrete Fourier Transform (DFT) due to its computational efficiency, especially when processing large EEG datasets. The algorithm categorizes data into even and odd elements, using a recursive strategy to optimize DFT calculations. This decomposition allows for swift processing of EEG signals, a key feature of the FFT's utility in frequency-domain analysis.

The FFT method involves breaking a sequence of N data points (where N is a power of two) into smaller, recursive calculations, using the 'butterfly' operation to efficiently compute the DFT, as detailed in Equations 1 to 4 (Sun et al., 2021). This process highlights FFT's role in processing multidimensional EEG data, combining spatial, frequency, and temporal domains for comprehensive signal analysis.

$$X(k) = \sum_{n=0}^{N-1} x(n)e^{-\frac{2\pi i}{N}nk} \quad (1)$$

$$X(k) = \sum_{n=0}^{N/2-1} x(2n)W_N^{nk} + \sum_{n=0}^{N/2-1} x(2n+1)W_N^{(n+\frac{N}{2})k} \quad (2)$$

$$X(2r) = \sum_{n=0}^{N/2-1} g(n)W_{N/2}^{nr} \quad (3)$$

$$X(2r+1) = \sum_{n=0}^{N/2-1} h(n)W_{N/2}^{nr} \quad (4)$$

3.3. Azimuthal equidistant projection

The Azimuthal Equidistant Projection (AEP) offers a novel method for representing 3D EEG data on a 2D surface, minimizing distortion while preserving data integrity, particularly useful in EEG analysis (Wu and Yao, 2007). This technique involves converting EEG spatial data into geographical coordinates, and then projecting them onto a flat plane using AEP (Figure 9). Electrode positions are first translated into longitude and latitude and then mapped with the AEP formula (Equation 5), where λ , ϕ , and R represents longitude, latitude, and the sphere's radius, respectively.

$$x = R \cos(\lambda) \cos(\phi) ; y = R \sin(\lambda) \cos(\phi) \quad (5)$$

The method ensures that distances from a central point are accurately preserved, effectively capturing the spatial and temporal dimensions of EEG data on a single visual plane. While this approach maintains spatial relationships vital for EEG interpretation, it primarily preserves accuracy near the central point, with potential distortions in peripheral regions (Bashivan et al., 2016). AEP's strength lies in its capacity to present complex EEG data dynamically, offering an effective visualization of brain activity.

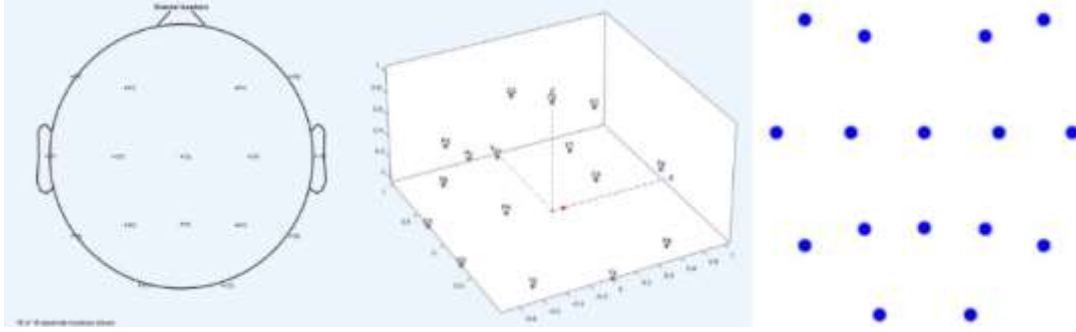


Figure 9. 2D Representation of 16 EEG electrodes placements based on the concept of the AEP

3.4. Transforming features into RGB images

The transformation of EEG signals into RGB images involves capturing the spatial, spectral, and temporal complexities of the data. Traditional methods that form vectors from electrode measurements fail to preserve these intricate structures, leading to the development of a two-dimensional imaging strategy. This approach not only maintains the spatial distribution of the EEG but also encodes spectral information through different color channels.

Using azimuthal equidistant projection, 3D electrode locations are mapped onto a 2D plane. This technique ensures that distances from a central point on the spherical model of the head are accurately reflected on the plane, although relative distances between electrode pairs may shift. The projection yields a spatial distribution of cortical activity, which is then interpolated onto a 32x32 grid using the Clough-Tocher scheme (Alfeld, 1984), optimizing the balance between signal resolution and computational efficiency.

Each frequency band produces a topographical map, and these maps are combined to create a tri-channel (RGB) image (Figure 10). This image, rich in spatial and spectral detail, is fed into a deep convolutional neural network for advanced analysis.

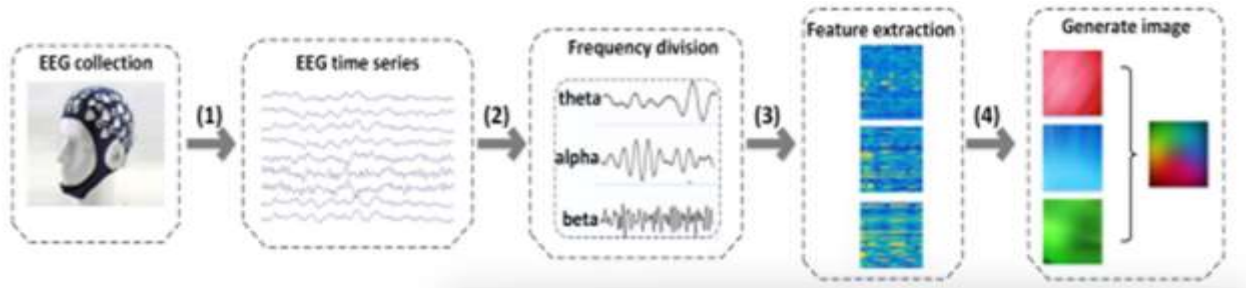


Figure 10. Image construction algorithm

3.5. CNN model architecture

CNN is highly effective in extracting relevant features from visual data by using specialized convolutional filters to identify patterns. The CNN architecture consists of three key layers: the convolutional layer, the pooling layer, and the fully connected layer. The convolutional layer applies filters (or kernels) to the input data, generating feature maps that capture significant data patterns. The pooling layer, particularly max pooling, reduces the dimensionality of these feature maps by selecting the maximum values, simplifying the data while retaining essential information.

Finally, the fully connected layer classifies the input into categories, such as healthy or pathological states, based on a trained dataset. The network's architecture includes an input layer followed by convolutional, pooling, and fully connected layers. Each pixel of the input image is processed through convolution, forming a feature map, and non-linearities are managed using ReLU layers. CNNs excel at extracting spatial features, such as color and edges, but struggle with time-series data, such as EEG signals, which include crucial temporal dynamics (Sharma, G. and Joshi, A, 2021).

Two CNN models were utilized in this study to classify EEG data represented as RGB images. Both models were designed to capture spectral and temporal features through convolutional and pooling layers. Model A, with a simpler architecture, processed the input images using fewer layers, while Model B incorporated additional

convolution and pooling layers for more complex feature extraction. In both models, dense layers were employed for classification, with regularization techniques such as dropout, early stopping, data augmentation, and 5-fold cross-validation applied to prevent overfitting. These models were used to analyze and classify EEG data into healthy or schizophrenia states based on the extracted features (Tables 3 and 4).

Table 3. Model A summary

Layer (type)	Output Shape	Parameters
input_layer (InputLayer)	(None, 256, 256, 3)	0
conv2d (Conv2D)	(None, 256, 256, 32)	896
conv2d_1 (Conv2D)	(None, 256, 256, 32)	9,248
max_pooling2d (MaxPooling2D)	(None, 128, 128, 32)	0
max_pooling2d_1 (MaxPooling2D)	(None, 64, 64, 32)	0
flatten (Flatten)	(None, 131072)	0
dense (Dense)	(None, 512)	67,109,376
dropout (Dropout)	(None, 512)	0
dense_1 (Dense)	(None, 256)	131,328
dropout_1 (Dropout)	(None, 256)	0
dense_2 (Dense)	(None, 1)	257
Total Parameters:	201,753,317	
Trainable Parameters:	67,251,105	
Optimizer Parameters:	134,502,212	

Table 4. Model B summary

Layer (type)	Output Shape	Parameters
input_layer (InputLayer)	(None, 256, 256, 3)	0
conv2d_2 (Conv2D)	(None, 256, 256, 32)	896
conv2d_3 (Conv2D)	(None, 256, 256, 32)	9,248
max_pooling2d_2 (MaxPooling2D)	(None, 128, 128, 32)	0
conv2d_4 (Conv2D)	(None, 128, 128, 64)	18,496
max_pooling2d_3 (MaxPooling2D)	(None, 64, 64, 64)	0
flatten_1 (Flatten)	(None, 262144)	0
dense_3 (Dense)	(None, 512)	134,218,240
dropout_2 (Dropout)	(None, 512)	0
dense_4 (Dense)	(None, 256)	131,328
dropout_3 (Dropout)	(None, 256)	0
dense_5 (Dense)	(None, 1)	257
Total Parameters:	403,135,397	
Trainable Parameters:	134,378,465	
Optimizer Parameters:	268,756,932	

3.6. Implementation and training

The implementation of the current study was performed on a system with an AMD Ryzen 7 7730U CPU, 16 GB RAM, AMD Radeon Vega 8 GPU, and Windows 10 OS. MATLAB was used for EEG data tasks such as loading, filtering, sampling, and visualization, while Google Colab was employed for training, validating, and classifying the RGB images using deep neural networks (DNNs). Multiple Python libraries, including Keras and TensorFlow, were utilized. The model's performance was assessed based on accuracy, precision, recall, F1 score, ROC AUC, and convergence speed.

Deep learning parameters like filter dimensions, output channel quantity, and network depth were optimized through experimental trials. Weight adjustments during training were guided by back-propagation, and performance was

enhanced using batch normalization and dropout techniques. The Adam optimizer with an initial learning rate of 0.0001 was employed, and the model was trained for 50 epochs with a batch size of 32. Binary cross entropy served as the loss function. The final approximate ratios for training, validation, and testing in this K-Fold cross-validation setup are Training: 72%, Validation: 8%, and Testing: 20%. This is achieved by dividing the data into 5 folds for K-fold cross-validation. Within each fold, 90% of the training data is used for actual training, and 10% is used for validation.

The network architecture included stacked convolutional layers with small 3×3 receptive fields, each using ReLU activation and one-pixel padding to maintain spatial resolution. Max-pooling layers with 2×2 windows followed the convolutional layers, gradually expanding the receptive field. The number of kernels doubled as the network deepened.

The dataset consisted of 12264 non-overlapping epochs from 84 patients (both healthy and schizophrenia), with each epoch converted into 256×256 RGB images using FFT. Data augmentation was performed by adding Gaussian noise (0.1 of σ), generating a total of 24528 RGB images (Figure 11).

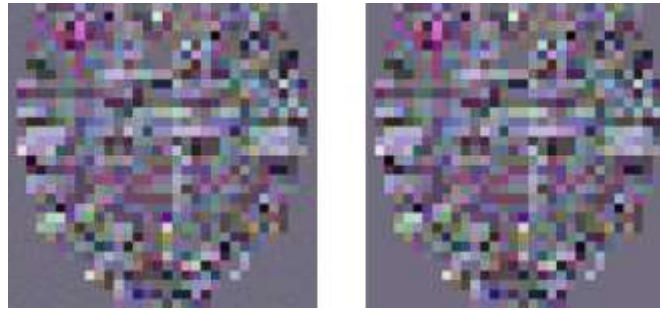


Figure 11. Augmented RGB image for FFT features (left), generated RGB image for FFT features (right)

4. Results

Power Spectral Density (PSD) was applied for FFT feature extraction on the EEG data, comparing the mean PSD values across three frequency bands (α , β , and θ) for healthy controls (HC) and SZ patients (Figure 12).

Model B achieved the best performance in terms of accuracy, precision, recall, F1 score, ROC AUC, and implementation time for FFT analysis, with the following metrics: Accuracy: 95.97%, Precision: 95.71%, Recall: 96.73%, F1: 96.22%, and ROC AUC: 95.91%. The detailed results are illustrated in Figures 13 to 16.

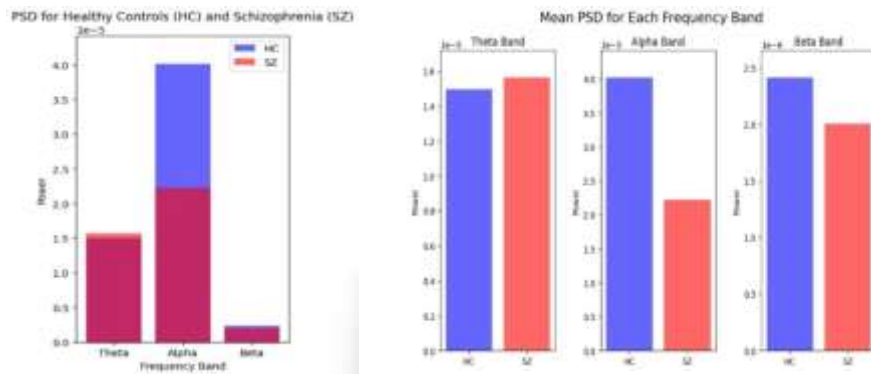


Figure 12. Comparison of PSD values for α , β and θ bands for HC and SZ (left), mean PSD values for each frequency band (right)

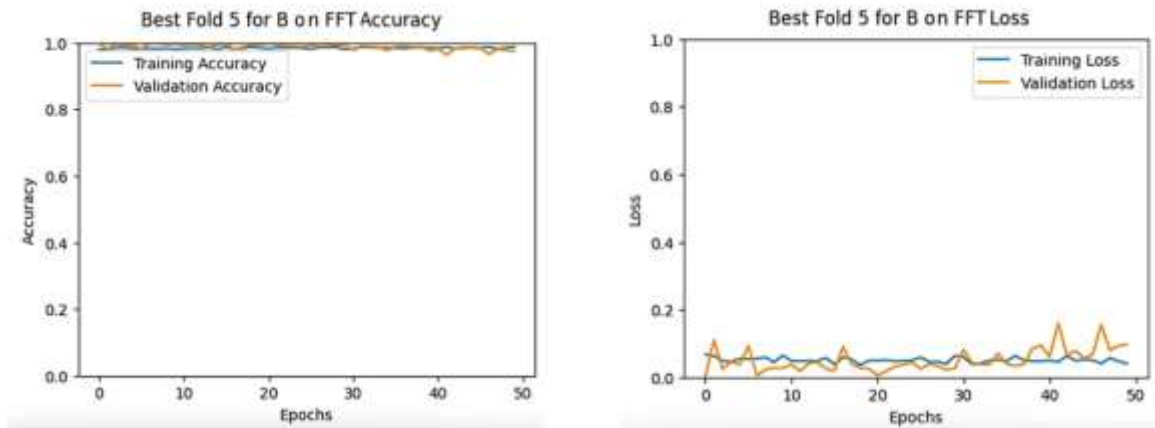


Figure 13 Training and validation accuracies for B model on FFT (left), training and validation losses for B model on FFT (right)

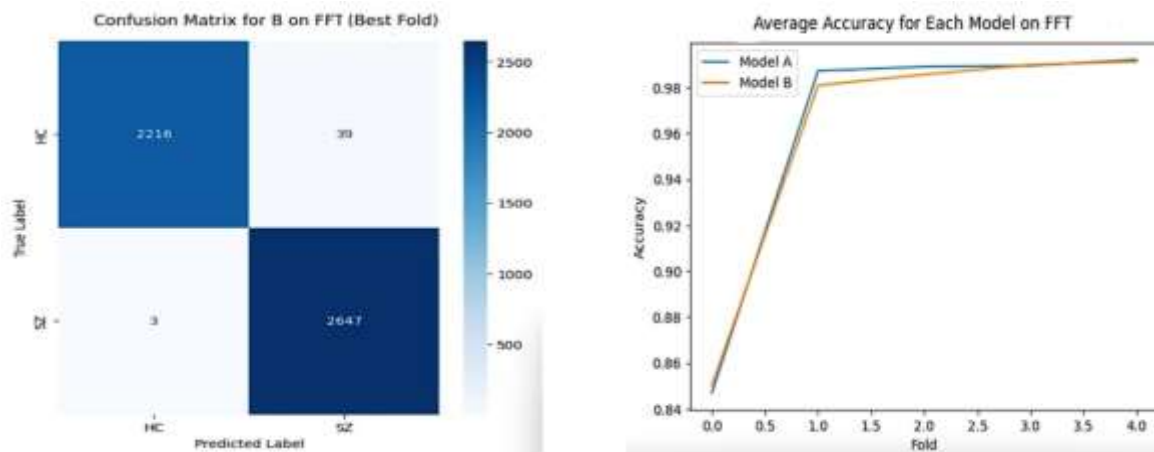


Figure 14. Model B confusion matrix on FFT (left), average accuracy for both models on FFT (right)

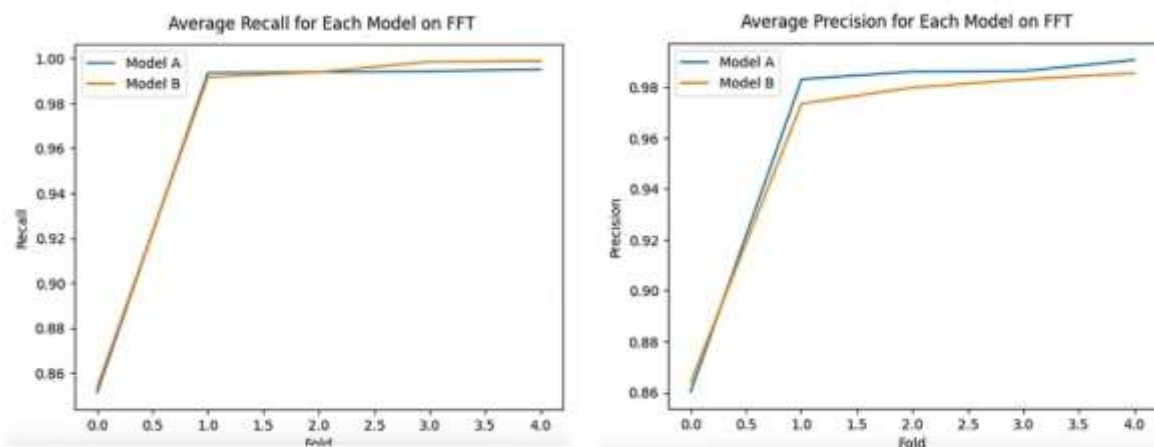


Figure 15. Average recall for both models on FFT (left), average precision for both models on FFT (right)

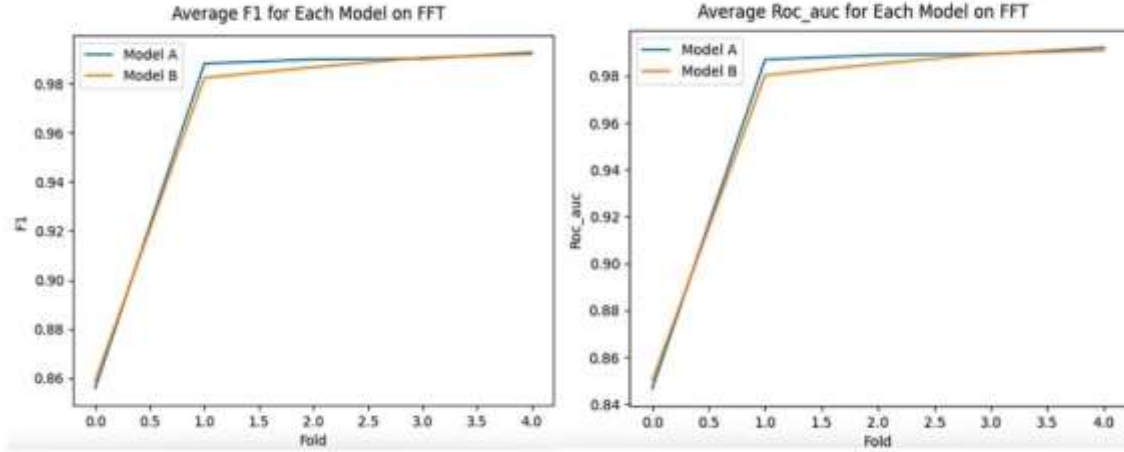


Figure 16. Average F1 for both models on FFT (left), average ROC AUC for both models on FFT (right)

5. Discussion

The findings of the current study highlight significant differences in the PSD of alpha, beta, and theta frequency bands between HC and SZ patients. These results are in agreement with previous studies, particularly the findings by (Murphy and Öngür, 2019), (Koshiyama et al., 2021) and others, which have documented abnormalities in the PSD and phase dynamics of alpha and theta oscillations in individuals with schizophrenia.

The results indicate a pronounced difference in the alpha band PSD, with healthy controls exhibiting significantly higher alpha power compared to schizophrenia patients. This aligns with the established literature, which reports a lower peak frequency and decreased alpha power in schizophrenia, particularly in regions such as the temporal and cingulate cortices. The study by Murphy and Öngür (2019) describes this phenomenon as "alpha slowing," where the peak frequency of alpha oscillations shifts leftward. This abnormality, widely distributed across multiple brain regions in schizophrenia patients, has been linked to disrupted neural synchrony and impaired cognitive functions.

In the current study, the reduced alpha PSD in schizophrenia patients could reflect a similar pathological mechanism, pointing to widespread cortical dysregulation. The robust nature of this finding warrants further exploration, as alpha oscillations are critical for various neural processes, including attention, memory, and sensory integration. The comparison with healthy controls further underscores the significance of alpha abnormalities as a biomarker for schizophrenia.

The consistent reduction in alpha PSD and the subtle differences in beta and theta PSD highlight the importance of frequency-specific analyses in understanding schizophrenia pathology. The widespread and robust alpha slowing observed in both the current and previous studies underscores its potential as a biomarker for schizophrenia. Future research could focus on regional-specific analyses to explore the spatial distribution of these abnormalities further. Moreover, integrating phase dynamics and functional connectivity analyses with PSD measures could provide a more comprehensive understanding of neural oscillatory disruptions in schizophrenia. Such approaches could pave the way for novel therapeutic targets and interventions aimed at restoring normal oscillatory dynamics in affected individuals.

The proposed CNN-Sigmoid model demonstrated superior performance compared to prior studies utilizing the same EEG dataset for schizophrenia classification. Achieving an accuracy of 95.97%, it surpassed the CNN model by Naira and Alamo (2019) with 90% accuracy, the DBN model by Phang et al. (2019) with 93.06%, and the CNN-LSTM model by Singh et al. (2021) with 94.08%. Sensitivity, a critical metric in medical diagnostics, was notably higher (96.73%) in the proposed model compared to the CNN-LSTM (92.70%). Additionally, the model achieved a ROC AUC of 95.91%, providing a robust measure of classification ability, which previous studies did not report. The precision (95.71%) and F1 score (96.22%) also outperformed Singh et al.'s model, indicating balanced and reliable predictions (Table 5).

Table 5. Comparison with other DL models' performances that used the same NNCI dataset

Work	Model	Classifier	% Accuracy	% Sensitivity	% ROC AUC	% Precision	% F1 Score
(Naira and Alamo, 2019)	CNN	Softmax	90.00	90.00	NA	NA	NA
(Phang et al., 2019)	DBN	Softmax	93.06	95.00	NA	NA	NA
(Singh et al., 2021)	CNN-LSTM	Sigmoid	94.08	92.70	NA	NA	93.62
The Proposed Method	CNN	Sigmoid	95.97	96.73	95.91	95.71	96.22

The improvements can be attributed to the model's architecture and feature extraction techniques, which effectively capture EEG data's spatiotemporal complexity. However, the reliance on deep learning methods poses challenges, such as computational demands and susceptibility to overfitting, particularly with limited dataset sizes. While regularization techniques were applied, further validation on larger, diverse datasets is needed.

Compared to other studies, the proposed model demonstrates higher predictive accuracy and sensitivity while addressing issues such as noise in EEG data. Despite these strengths, challenges related to class imbalance and generalizability persist, aligning with broader challenges in biomedical deep learning. Future efforts should focus on integrating techniques like transfer learning and explainability to enhance clinical applicability and reliability.

6. Conclusion

This study aimed to improve SZ diagnosis using EEG data and deep learning models, focusing on classification accuracy by extracting spectral power features via FFT and analyzing them with CNNs.

The proposed CNN model achieved an accuracy of 95.97%, outperforming previous studies that used the same dataset. Notably, it exceeded the 90% accuracy reported by Naira and Alamo (2019) with a CNN model, the 93.06% accuracy achieved by Phang et al. (2019) using a DBN, and the 94.08% accuracy obtained by Singh et al. (2021) with a CNN-LSTM model. This highlights the effectiveness of the proposed approach in improving classification performance for EEG-based schizophrenia detection.

Despite these advancements, limitations such as class imbalance, overconfidence in predictions, and high computational demands remain challenges. The reliance on a limited dataset further emphasizes the need for more comprehensive data collection in future research.

Future work should focus on alternative data representation, enhanced data augmentation, and larger, more balanced datasets. Addressing the underperformance of certain FFT-based models could further refine EEG-based diagnostic tools for schizophrenia and other neurological disorders.

Ethics Permissions

This paper does not require ethics committee approval.

Conflict of Interest

The authors declare that there is no conflict of interest for this paper.

Author Contribution

Sema Koç Kayhan identified the research problem, suggested methodological approach, and reviewed the manuscript. Zekeriya Edahil developed the software, tested the results and wrote the manuscript.

References

- Alfeld, P. (1984). A trivariate Clough-Tocher scheme for tetrahedral data. *Computer Aided Geometric Design*, 1(2), 169–181.
- Bashivan, P., Rish, I., Yeasin, M., and Codella, N. (2016). *Learning representations from EEG with deep recurrent-convolutional neural networks*, published as a conference paper at ICLR
- Bonita, J. D., Ambolode, L. C. C., Rosenberg, B. M., Cellucci, C. J., Watanabe, T. A. A., and Rapp, P. E. (2014). Time domain

measures of inter-channel EEG correlations: a comparison of linear, nonparametric and nonlinear measures. *Cogn Neurodyn*, 8, 1–15.

Chen, Z., Zhao, Y., Jin, C., & Zhao, W. (2019). A Review on EEG Based Emotion Classification. <https://doi.org/10.1109/iaeac47372.2019.8997704>

Delorme, A. (2019). EEG preprocessing in EEGLAB [PDF]. Swartz Center for Computational Neuroscience. https://sccn.ucsd.edu/github/wiki/files/eeGLAB2019_aspet_artifact_and_ica.pdf

Ganesh, R. N., and Kumar, D. K. (2011). An overview of independent component analysis and its applications. *Informatica*, 35(1).

Gorbachevskaya, N. and Borisov, S. (2019). EEG of healthy adolescents and adolescents with symptoms of schizophrenia (Database). http://brain.bio.msu.ru/eeG_schizophrenia.htm, 2019. (Accessed date: 7 January 2025).

Harm, M., Hope, M., and Household, A. (2013). Diagnostic and Statistical Manual of Mental Disorders. *American Psychiatric Association*. (5th ed. pp. 87-90).

Harrison, G., Hopper, K., Craig, T., Laska, E., Siegel, C., and Wanderling, J. (2001). Recovery from psychotic illness: A 15-and 25-year international follow-up study. *The British Journal of Psychiatry*, 178, 506-517.

Jaeschke, K., Hanna, F., Ali, S., Chowdhary, N., Dua, T., and Charlson, F. (2021). Global estimates of service coverage for severe mental disorders: Findings from the WHO Mental Health Atlas 2017. *Global Mental Health*, 8, e27.

Kingphai, K., and Moshfeghi, Y. (2021). On EEG Preprocessing Role in Deep Learning Effectiveness for Mental Workload Classification. 10.1007/978-3-030-91408-0_6.

Koshiyama, D., Miyakoshi, M., Tanaka-Koshiyama, K., Joshi, Y. B., Sprock, J., Braff, D. L., and Light, G. A. (2021). Abnormal phase discontinuity of alpha- and theta-frequency oscillations in schizophrenia. *Schizophrenia Research*, 231, 73–81. <https://doi.org/10.1016/j.schres.2021.03.007>

Kwon, J. S., and Carpenter, C. J. (2007). Electroencephalography in schizophrenia. *Schizophrenia Bulletin*, 33(2), 253-265.

Min, S., Lee, B., and Yoon, S. (2017). Deep learning in bioinformatics. *Briefings in Bioinformatics*, 18, 851–869

Murphy, M., and Öngür, D. (2019). Decreased peak alpha frequency and impaired visual evoked potentials in first episode psychosis. *NeuroImage. Clinical*, 22, 101693. <https://doi.org/10.1016/j.nicl.2019.101693>

Naira, C. A. T., and Alamo, C. J. L. D. (2019). Classification of People who Suffer Schizophrenia and Healthy People by EEG Signals using Deep Learning. *International Journal of Advanced Computer Science and Applications(IJACSA)*, 10(10). <http://dx.doi.org/10.14569/IJACSA.2019.0101067>

Newson, J. J., and Thiagarajan, T. C. (2019). EEG frequency bands in psychiatric disorders: A review of resting state studies. *Frontiers in Human Neuroscience*, 12, 521. <https://doi.org/10.3389/fnhum.2018.00521>

Niedermeyer, E., and Lopes da Silva, F. H. (2005). *Electroencephalography: Basic principles, clinical applications, and related fields* (6th ed., pp. 123-145, 200-210). Lippincott Williams & Wilkins.

Oostenveld, R., and Praamstra, P. (2001). The five percent electrode system for high-resolution EEG and ERP measurements. *Clinical Neurophysiology*, 112(4), 713–719.

Phang, C. R., Ting, C. M., Samdin S. B., and Ombao, H. (2019). *Classification of EEG-based Effective Brain Connectivity in Schizophrenia using Deep Neural Networks*. 9th International IEEE/EMBS Conference on Neural Engineering (NER), San Francisco, CA, USA. pp. 401-406, doi: 10.1109/NER.2019.8717087.

Plis, S. M., Hjelm, D. R., Salakhutdinov, R., Allen, E. A., Bockholt, H. J., Long, J. D., Johnson, H. J., Paulsen, J. S., Turner, J. A., and Calhoun, V. D. (2014). Deep learning for neuroimaging: a validation study. *Frontiers in Neuroscience*, 8(August):1–11. ISSN 1662-453X. <https://doi.org/10.3389/fnins.2014.00229>

Savio, A., Charpentier, J., Termenon, M., Shinn, A. K., and Graña, M. (2010). Neural classifiers for schizophrenia diagnostic support on diffusion imaging data. *Neural Network World*, 20, 935–949.

Sharma, G., and Joshi, A. (2021). *Novel EEG based Schizophrenia Detection with IoMT Framework for Smart Healthcare*. cornell university. <https://doi.org/10.48550/arxiv.2111.11298>

Sharma, M., Patel, R.K., Garg, A., SanTan, R., and Rajendra Acharya, U. (2023). Automated detection of schizophrenia using deep learning: A review for the last decade. *Physiological Measurements*, 44(03TR01). <https://doi.org/10.1088/1361-6579/acb24d>

Singh, K., Singh, S., and Malhotra, J. (2021). Spectral features based convolutional neural network for accurate and prompt identification of schizophrenic patients. Proceedings of the Institution of Mechanical Engineers, Part H: *Journal of Engineering in*

Medicine, 235(2), 167-184. doi:10.1177/0954411920966937

Sun, J., Cao, R., Zhou, M., Hussain, W., Wang, B., Xue, J., and Xiang, J. (2021). A hybrid deep neural network for classification of schizophrenia using EEG data. *Scientific Reports*, 11, 4706. <https://doi.org/10.1038/s41598-021-83350-6>

Upadhyay, R., Manglick, A., Reddy, D. K., Padhy, P. K., and Kankar, P. K. (2015). Channel optimization and nonlinear feature extraction for electroencephalogram signals classification. *Computers and Electrical Engineering*, 45, 222–234

World Health Organization. (2023). Schizophrenia. [Fact sheet]. World Health Organization. September 1. <https://www.who.int/news-room/fact-sheets/detail/schizophrenia>

Wu, D., and Yao, D. (2007). The azimuth projection for the display of 3-D EEG data. *Computers in Biology and Medicine*, 37(12), 1821-1826. <https://doi.org/10.1016/j.combiomed.2007.06.006>

Performance Evaluation of Flywheel, Battery and Superconducting Magnetic Energy Storage Systems on Frequency Regulation in the Context of Renewable Energy Integration

Ahmet Mete Vural^{1*}, Aliyu Garba Ibrahim²

Keywords

Battery energy storage,
Flywheel energy storage,
Superconducting energy storage,
Wind turbine,
Photovoltaic,
Artificial rabbit optimization,
Lightning search algorithm,
Whale optimization algorithm

Abstract – Frequency regulation is a crucial aspect of power system operation as it ensures that the power systems operate in a stable manner. Variations in load and renewable energy generation are the main causes of frequency instability due to weather uncertainty. This paper investigates the effects of variations in load and renewable energy generation on frequency control in power systems. Also, three different energy storage technologies (Flywheel, Battery, and Superconducting Magnetic Energy Storage) are integrated to test systems to investigate their effects on frequency control. To enhance the dynamic performance of the frequency controller, three recent optimization methods (Artificial Rabbit Optimization, Lightning Search Algorithm, and Whale Optimization Algorithm) are utilized when the test systems are subjected to different operating conditions and disturbances. The superiority of the Artificial Rabbit Optimization in comparison with other optimization methods is shown in effectively mitigating frequency oscillations in both single-area and two-area test systems. The energy storage solutions are evaluated in terms of damping effect, transient stability, and integral time absolute error index in two test systems. A compressive simulation study is conducted, and the results are presented and discussed.

1. Introduction

The world has seen a massive investment in renewable energy research and invention due to the living reality of global warming disasters such as acid rain, the recent wildest forest fire-like inferno, and drought. Renewable energy source (RES) is the only option out of this disaster and at the backbone of the RES. Energy storage system (ESS) stands to smoothen the integration and prevent power outages. Integrating ESSs and power-reserved synchronization is an effective solution for overcoming RES intermittency and fluctuating effects. On the other hand, frequency regulation is a key component of maintaining stability and reliability in electrical power systems. This process ensures that the system frequency remains within designated limits despite fluctuations in power demand and supply. These fluctuations are primarily caused by changes in consumer load and the unpredictable nature of RES, like wind and solar power. Advanced control strategies and optimization algorithms are necessary to mitigate frequency deviations when the power systems are faced with various disturbances such as sudden load variation, fault, and unpredictable RES generation. ESS provides frequency regulation by dynamically injecting/absorbing power to/from the grid in response to a decrease/increase in frequency. Due to fast response time, ESS technology can inject large amounts of power into the grid in the shortest period, which can be used as virtual inertia. The two most important aspects related to applying fast responsive energy storage technologies for frequency regulation services that, control and sizing, are discussed

^{1*}Corresponding Author. Electrical and Electronics Engineering Department, Gaziantep University, 27310 Gaziantep, Türkiye.

E-mail: mvural@gantep.edu.tr  ORCID: 0000-0003-2543-4019

²Graduate School of Applied and Natural Sciences, Gaziantep University, 27310 Gaziantep, Türkiye.

E-mail: aliyu.gibrahim@yahoo.com  ORCID: 0009-0000-4499-4324

Citation: Vural, A. M. and Ibrahim, A. G. (2025). Comparison of flywheel, battery and superconducting magnetic energy storage systems for frequency regulation. *Natural Sciences and Engineering Bulletin*, 2(1), 26-55.

in detail for both single and hybrid storage technologies (Akram et al., 2020). In the literature, frequency regulation studies are multifaceted in terms of the type of RES used, the type of controller, and the kind of system disturbance. An adaptive control strategy to coordinate the generator and the governor with an ESS in frequency regulation has been proposed (Ibrahim et al., 2022). The comparison between the ESS compensation with a conventional droop control and the proposed method has been used. The simulation results show that compared to the ESS with a fixed droop control scheme; and the proposed control scheme provides better results in regulating the frequency response by lowering the rate of change of frequency and improving the minimum frequency deviations during the generator tripping events. The droop control is not generally able to generate a large power output immediately after the disturbance, while it increases the power output with the increment of frequency deviation. In another research, superconducting magnetic energy storage system (SMES) and battery energy storage system (BESS) based hybrid energy storage systems are designed to reduce grid voltage fluctuations, and a new event-triggered control system is proposed for SMES to improve the microgrid's voltage and frequency stability (Vishnuvardhan and Saravanan, 2023). The multimachine system stability analysis of interconnected 375 MW hybrid wind and solar photovoltaic (PV) systems is connected with SMES energy storage. Analyzing the performance metrics of BESSs at different levels of penetrations of RES has been addressed (Li et al., 2023). By quantitatively evaluating the impact of BESSs with various energy-to-power ratios, it has been deduced that as the penetration of RES increases, the storage systems with higher energy-to-power ratio are favored. The effectiveness of BESS in providing primary frequency control has been addressed when applied to a weak grid system (Julius et al., 2022). The state of charge (SOC) restoration logic has been considered to ensure service continuity and effective frequency regulation. The optimal size of BESS installation to accomplish the goal has also been studied with a dynamic grid model. Research and inventions have been overflowing in the conventional proportional integral (PI) and proportional integral derivative (PID) types of controllers and their parameter optimization in power systems. The PID controller is tuned using different optimization methods with comparison and a novel genetic algorithm-fuzzy logic self-tuning technique is suggested (Ali et al., 2024). Results show the suggested method outperforms others in restoring power system stability. The artificial rabbit optimization (ARO) method is used to tune the controller parameters in a microgrid, ensuring stability under major disturbances (Khalil et al., 2023). Sensitivity analysis with $\pm 25\%$ parameter variations confirms the robustness of the approach. The study suggests a bat-inspired optimization algorithm which is modeled on animal echolocation behavior (Ramesh Kumar et al., 2013). This optimization approach is used to enhance load frequency control (LFC) in a two-area power system with SMES unit. Elsis et al., (2018), introduces the Gravitational Search Algorithm and Bat-inspired Algorithm as two techniques for designing model predictive controller for LFC. The power system is embedded with SMES and compressive energy storage. The study of Ray et al., (2019), proposes a hybrid firefly particle swarm optimization (PSO) technique to tune PID controller parameters for minimizing frequency deviation in a microgrid under varying wind speeds and load demands. Comparative analysis with PSO and firefly algorithms have been carried out using various performance indices. The integration of RES into power grids presents significant challenges, particularly in maintaining frequency stability due to their intermittent nature. Extensive research has been conducted on frequency control strategies for single renewable energy integration with standalone energy storage systems (Wang et al., 2022a; Yao et al., 2016) modeling ESS for grid (Hutchinson et al., 2024; Cansiz et al., 2017; Georgious et al., 2021; Hajiaghasi et al., 2019; Lin and Zamora, 2022; Peralta et al., 2018; Qu and Ye, 2023; Santhi et al., 2013; Worku, 2022) frequency regulation, and the economic comparison of different ESS technologies (McIlwaine et al., 2021; Moradi-Shahrbabak and Jadidoleslam, 2023; Ranjan Chakraborty et al., 2022; Rouniyar and Karki, 2021; Sassi et al., 2017). Additionally, studies have explored coordinated control strategies for hybrid storage systems (Nguyen-Huu et al., 2020), optimization-based enhancements for conventional controllers (Sahu et al., 2015), and the role of ESS in mitigating frequency fluctuations caused by hybrid RES penetration (Ibraheem et al., 2022; Mugyema et al., 2023). However, these studies often focus on isolated aspects of the problem rather than providing a comprehensive solution. This paper bridges these research gaps by integrating all these critical aspects into a unified framework. By combining modeling, economic considerations, control strategies, and optimization techniques with extensive simulation cases, this study presents a holistic approach to frequency regulation, offering a more robust and practical solution for modern power grids facing increasing renewable energy penetration.

The main contributions of this paper are:

1. LFC of single-area and two-area systems to achieve a high level of stability and robustness due to the penetration of RES such as PV and wind turbine (WT) is realized.
2. The contribution of FESS, BESS, and SMES in the LFC is evaluated by comparison.
3. The comparison of optimization methods such as ARO, LSA, and WOA in enhancing the controller parameters for effective mitigation of frequency instability during severe disturbances is carried out.

The paper is structured as follows: After the introductory section, Section 2 presents the modeling of a single-area power system, the relevant parts, and their transfer functions. The introduction of the RES, such as PV and WT, and the role they play in the system in a different weather condition and their transfer function. A dedicated subsection will provide detailed information about the ARO algorithm, the leading algorithm in this work, for better optimization and enhancing the PID parameter. The third subsection is for results and discussion of the simulations, which presents the simulation results obtained from both test systems under different operating scenarios. The detailed discussion is also made on the obtained results. The PID parameter tuning performances of ARO, lighting search algorithm (LSA), and whale optimization algorithm (WOA) methods are evaluated in detail, together with the effects of various ESSs in the frequency control operation under optimized parameters of ARO. The general conclusions are drawn at the end.

2. Materials and Methods

2.1. Modeling of the single-area system

The transfer function model of the single-area power system is illustrated in Figure 1. The generator inertia constant is defined by $H=5$. The turbine acts as the mechanical power source with its dynamics defined by a time constant $T_t=0.5s$. The governor with the time constant, $T_g=0.2 s$ detects speed changes and modulates the turbine input to restore the steady-state operation. The governor's typical speed regulation is defined as $R=20$, the percentage change of speed from no-load to full-load. The inertia load, incorporating both rotating masses and the connected load is quantified by the proportionality constant $D=0.8$, which represents the percentage change in load per percentage change in frequency (Ray et al., 2019).

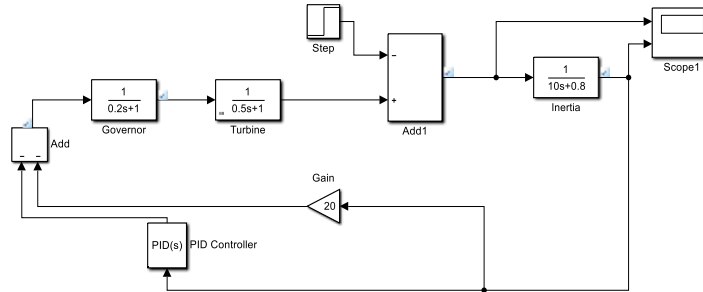


Figure 1. Transfer function representation of the single-area power system

2.2. Modeling of the two-area system

The two-area power system is usually modelled as two separate generation locations, each of which is modelled using an ideal AC voltage source and a reactance connected in series. Then, the outputs of these locations are connected with a tie line. By this way, the steady-state behavior of this system can be modelled in its simplest form. The tie-line active power flow from area-1 to area-2 when neglecting losses can be calculated,

$$P_{12} = \frac{|E_1||E_2|}{X_{12}} \sin\phi_{12} \quad (1)$$

where, E_1 and E_2 respectively represent the output voltage of each generator, X_{12} is the tie-line reactance, and ϕ_{12} is the phase angle difference between each generator output. The tie line power deviation is represented by (2), which is perceived as an increase in load in one area and a corresponding decrease in the other, depending on the flow's direction. This direction is determined by the difference in phase angle between the two areas. For instance, if $\Delta\phi_1 - \phi$ is positive, the active power flows from area 1 to 2. P_s is the synchronizing power

coefficient. The conventional LFC relies on tie-line bias control as shown in (3), where each control area aims to minimize the area control error (ACE) to zero. The ACE in each area is a combination of frequency deviation and tie-line power flow error.

$$\Delta P_{12} = P_s (\Delta \varphi_1 - \Delta \varphi_2) \quad (2)$$

$$ACE_i = \sum_{j=1}^n \Delta p_{ij} + k_i \Delta f \quad (3)$$

The area bias k_i determines the level of interaction between neighboring areas during a disturbance. Optimal performance is achieved when k_i is set to the frequency bias factor of that area, $B_i = \beta_i + D_i$. For a two-area system, the ACE equations are given as,

$$ACE_1 = \Delta P_{12} + B_1 \Delta F_1 \quad (4)$$

$$ACE_2 = \Delta P_{21} + B_2 \Delta F_2 \quad (5)$$

B_1 and B_2 are known as frequency bias factors, ΔP_{12} and ΔP_{21} are changes in power output in both areas. Each area is modeled with an equivalent turbine and governor, and the incremental power balance is controlled by the tie-line bias control which is the ACE. In this study, the parameters of the two-area system are listed in Table 1 (Saadat, 1999). The synchronizing power coefficient P_s is taken as 2.0 p.u. The transfer function representation of the two-area power system is depicted in Figure 2.

Table 1. Parameters of the two-area power system

Parameter Name	Area-1	Area-2
Speed Regulation (R)	0.05	0.0625
Frequency Load Coefficient (D)	0.6	0.9
Inertia constant (H)	5	4
Base power(s)	1000MVA	1000MVA
Governor Time Constant (T_g)	0.2	0.3
Turbine Constant (T_t)	0.5	0.6
Integrator gain (K_I)	0.3	0.3
Nominal frequency	60Hz	60Hz

2.3. PV and WT models

The PV model can be expressed as the product of three transfer functions as given in (6) (Ibraheem et al., 2022). This model provides sufficient small signal behavior to capture the power dynamics of the PV system. The parameters are $T_{pv}=1.8$, which indicates the speed response of the PV system, $T_{in}=0.04$, which is the time constant that represents how quickly the inverter dynamics react to changes from the PV system, and $T_{1/c}=0.004$, which represents a control filter that smooths out the signal from the inverter.

$$\Delta P_{pv} = \frac{1}{T_{pv}s + 1} \times \frac{1}{T_{in}s + 1} \times \frac{1}{T_{1/c} + 1} \quad (6)$$

The wind turbine can be represented as a first-order transfer function as given in (7) (Ibraheem et al., 2022). The time constant $T_{WT}=1.5$ defines how the wind turbine's power output responds to changes in the input signal. In LFC, this model regulates the active power output, manages the frequency response, and controls the pitch angle or rotor speed of the wind turbine to optimize power generation.

$$\Delta P_{WT} = \frac{1}{T_{WT}s + 1} \quad (7)$$

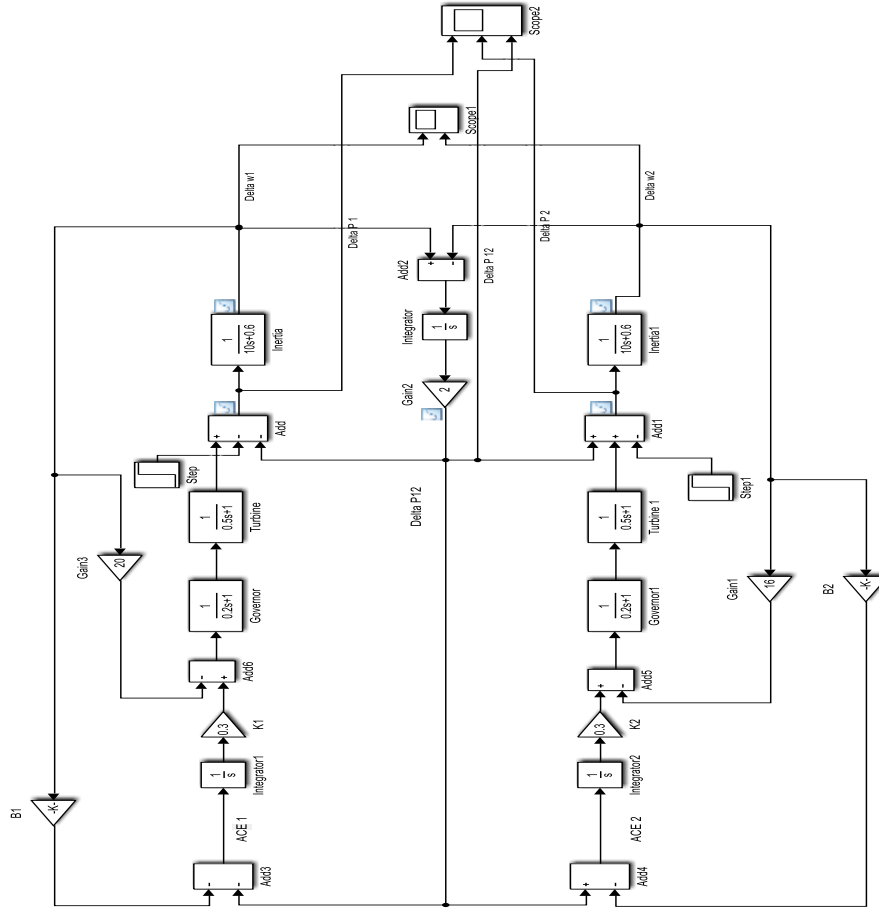


Figure 2. Transfer function representation of the two-area power system

2.4. Modeling of ESSs

For LFC studies, ESSs are considered ancillary services to provide or absorb active power to maintain system stability. The charging and discharging states are usually evaluated in contributing frequency stability. The change in the power output of BESS (ΔP_{BESS}) can be expressed as a first-order transfer function, given in (8) (Patel et al., 2019). The time constant of the BESS can be defined as $T_{BESS}=0.1s$. Similarly, the change in the power output of FESS (ΔP_{FESS}) can be expressed as a first-order transfer function, given in (9) (Ibraheem et al., 2022). For the flywheel energy storage system (FESS), the time constant T_{FESS} can be defined as 0.01s. For SMESS, (10) shows the change in the inductor voltage ΔE_d , where $K_d=1$ is the gain of the control loop and $T_d=0.03s$ is the time delay associated with the power system converter (El-Saady et al., 2018).

$$\Delta P_{BESS} = \frac{1}{T_{BESS}s + 1} \quad (8)$$

$$\Delta P_{FESS} = \frac{1}{T_{FESS}s + 1} \quad (9)$$

$$\Delta E_d(s) = \frac{K_d}{T_d s + 1} \quad (10)$$

The deviation in the inductor current (ΔI_d) in SMESS can be calculated as in (11). $L=2$ Henry stands for the inductance of the SMESS coil. The deviation in the SMESS unit's power flow (ΔP_{SMES}) is shown in (12), where $I_{d0}=5A$ is the initial value of the inductor current.

$$\Delta I_d = \frac{\Delta E_d}{sL} \quad (11)$$

$$\Delta P_{SMES} = I_{do} \times \Delta E_d + \Delta E_d \times \Delta I_d \quad (12)$$

A comprehensive analysis of FESS, BESS, and SMES is essential to understand their respective efficiencies, costs, and response times. This analysis enhances the practical value of energy storage studies by informing technology selection based on specific application requirements.

2.4.1. Comparative analysis of ESS

Each energy storage technology presents unique advantages and limitations. FESS offer high efficiency and rapid response but may incur higher costs depending on the materials used. BESS, particularly Li-ion batteries, provide high efficiencies and fast response times but are associated with significant capital cost. SMES deliver exceptional efficiency and the fastest response times; however, their high cost can restrict their practical application. A detailed comparative analysis of these technologies is given in Table 2. Considering efficiency, cost, and response time, can significantly enhance the practical value of energy storage studies by guiding the selection of the most appropriate technology for specific applications.

Table 2. Comparative analysis of energy storage technologies

BESS	FESS	SMES
<ul style="list-style-type: none"> Efficiency: Lithium-ion (Li-ion) batteries, a common type of BESS, have efficiencies between 85% and 95% Cost: the capital costs for BESS can be high, which impacts their economic viability. Response Time: BESS can provide a fast response, making them suitable for various grid services, including frequency regulation and energy arbitrage (Jaffal et al., 2024). Economics Impacts: Particularly lithium batteries, have seen significant cost reductions, enhancing their economic attractiveness. They provide benefits like grid stabilization, energy arbitrage, and deferred infrastructure investments. However, factors such as a life span and degradation rates influence their overall economic viability. (Simpa et al., 2024) Environmental Impacts: Production involves mining and processing of raw materials, leading to environmental concerns. Life cycle assessments indicate that lithium-ion batteries have life cycle greenhouse gas emissions ranging from 625 to 659kg-CO_2eq/MWh, depending on the application scenario. (Zhang et al., 2025) 	<ul style="list-style-type: none"> Efficiency: FESS typically exhibits high efficiencies, ranging from 90% to 95%. Cost: the cost FESS varies depending on the materials used. For instance, a flywheel made from Carbon AS4C material cost approximately \$313 for a 10kg unit. Response Time: FESS is capable of rapid response times, making them suitable for applications requiring immediate power delivery (Altayf et al., 2024). Economic Impacts: Typically have high initial capital costs due to advanced materials and precision engineering requirements. However, they offer long operational lifespans and minimal maintenance needs, potentially leading to favourable life cycle costs. Environmental Impacts: FESS is environmentally friendly, as they do not involve chemical reactions, thereby eliminating risks of hazardous material leakage. Their primary environmental consideration is the energy consumed during manufacturing and operational losses. (Oskouei et al., 2022) 	<ul style="list-style-type: none"> Efficiency: SMES is known for their high efficiencies, typically around 90% to 97%. Cost: SMES has relatively costs, which can be a limiting factor for widespread adoption. Response Time: SMES offers extremely rapid response times, often in the range of milliseconds, making them ideal for applications requiring instantaneous power delivery (Moradi-Shahrbabak and Jadidoleslam, 2023). Environmental Impacts: the environmental footprint of SMES is primarily associated with the production and maintenance of superconducting material and the energy requirements for cooling. While operational emissions are minimal, the overall environmental impact depends on the energy sources used for cooling and maintenance. Economic Impacts: SMES is characterized by high efficiency and rapid response time but entail substantial costs due to the need for superconducting materials and cryogenic cooling systems. These factors currently limit their widespread economic feasibility. (Lu, 2022)

2.5. Optimization methods

2.5.1. Artificial rabbit optimization (ARO)

ARO is a recently developed metaheuristic algorithm introduced in 2022. It draws inspiration from the foraging and hiding behavior of a real rabbit, incorporating their energy dynamics that facilitate transitions between these strategies (Wang et al., 2022b). One of the key strengths of ARO is its compliance with the global search convergence theorem, which guarantees that the algorithm will not overlook the global optimum during the search process. Consequently, ARO proves to be an efficient and reliable approach for solving complex optimization problems, as demonstrated in this study. The pseudocode of the ARO method is shown in Figure 3. This method can be utilized to optimize the PID controller parameters (Khalil et al., 2023). Rabbits prioritize distant areas and disregard nearby resources during the foraging, consuming grass randomly in other regions rather than their own. This behavior, termed “detour foraging,” is emulated in the ARO algorithm. Each rabbit in the swarm is assumed to occupy its region containing grass and d burrows, while also visiting the positions of the other rabbits randomly for foraging. In practice, rabbits tend to explore around a food source to secure sufficient sustenance. Consequently, the detour foraging behavior in ARO reflects the tendency of each search agent to update its position toward a randomly selected individual within the swarm, incorporating a perturbation for variability (Khalil et al., 2023). The mathematical representation of this behavior is as follows:

$$\vec{V}_i(t+1) = \vec{x}_j(t) + R \cdot (\vec{x}_i(t) - \vec{x}_j(t)) + \text{round}(0.5 \cdot (0.05 + r_1)) \cdot n_1, i, j = 1, \dots, n \text{ and } j \neq i \quad (13)$$

$$R = L \cdot c \quad (14)$$

$$L = \left(e - e^{\left(\frac{t-1}{T}\right)^2} \right) \cdot \sin 2\pi r_2 \quad (15)$$

$$c(k) = \begin{cases} 1, & \text{if } k == g(l) \\ 0, & \text{else} \end{cases} \quad k = 1, \dots, d \text{ and } l = 1, \dots, [r_3 \cdot d] \quad (16)$$

$$g = \text{randperm}(d) \quad (17)$$

$$n_1 \sim N(0,1) \quad (18)$$

where $\vec{V}_i(t+1)$ is the candidate position of the i^{th} rabbit at the time $t+1$, while $\vec{x}_j(t)$ represents its position at iteration t . n represents the total number of the rabbit population, d corresponds to the dimension of the problem. T is the maximum number of the iteration, $[\cdot]$ is the ceiling function, round indicates rounding to the nearest integer, randperm returns a random permutation of the integers from 1 to d . Additionally, r_1, r_2 , and r_3 are three random numbers in the range of $(0,1)$. The parameter L denotes the running length, which quantifies the step size when performing the detour foraging, and n_1 follows a standard normal distribution.

In (13), the perturbation may assist ARO to avoid local extrema and perform a global search. And (15), the running length L , can generate a longer step during the initial iterations. It selects one of the burrows for hiding to decrease the probability of being attacked. To escape from predators, a rabbit typically digs multiple burrows around its nest as potential hiding spots. In this algorithm, at each iteration, a rabbit always constructs d burrows along each dimension of the search space. The j^{th} burrow of the i^{th} rabbit is generated by.

$$\vec{b}_{i,j} = \vec{x}_i(t) + H \cdot g \cdot \vec{x}_i(t), i = 1, \dots, n \text{ and } j = 1, \dots, d \quad (19)$$

$$H = \frac{T - t + 1}{T} \cdot r_4 \quad (20)$$

$$n_2 \sim N(0,1) \quad (21)$$

$$g(k) = \begin{cases} 1, & \text{if } k == j \\ 0, & \text{else} \end{cases} \quad k = 1, \dots, d \quad (22)$$

According to (19), the d burrows are generated within the proximity of a rabbit along each dimension. H is the hiding parameter which decreases linearly from 1 to $1/T$ over the course of iteration, incorporating a random perturbation. Initially, these burrows are generated in a bigger neighborhood around the rabbit. However, as the iterations rise, this neighborhood shrinks too.

In the wildlife of a rabbit, a chase is a norm, so to survive, the rabbit needs a hiding place. As a result, they are inclined to stochastically select a burrow from their burrows for sheltering to avoid getting caught. The hiding strategy can be formulated mathematically from (23-25).

$$\vec{v}_i(t+1) = \vec{x}_i(t) + R \cdot (\vec{r}_4 \cdot \vec{b}_{i,r}(t) - \vec{x}_i(t)), i = 1, \dots, n \quad (23)$$

$$g_r(k) = \begin{cases} 1, & \text{if } k == [r_5 \cdot d] \\ 0, & \text{else} \end{cases} \quad k = 1, \dots, d \quad (24)$$

$$\vec{b}_{i,r}(t) = \vec{x}_i(t) + H \cdot g_r \cdot \vec{x}_i(t) \quad (25)$$

Here, $\vec{b}_{i,r}$ denotes a randomly selected burrow for hiding among the d available burrows, and r_4 and r_5 are two random numbers in (0,1). Based on (23), the i^{th} Search individual attempts to update its position toward the selected burrow.

After one of both detour foraging and random hiding is achieved, i^{th} rabbit will be updated as follows:

$$\vec{x}_i(t+1) = \begin{cases} \vec{x}_i(t), & f(\vec{x}_i(t)) \leq f(\vec{v}_i(t+1)) \\ \vec{v}_i(t+1), & f(\vec{x}_i(t)) > f(\vec{v}_i(t+1)) \end{cases} \quad (26)$$

In ARO, at the initial phase, rabbits often conduct detour foraging while frequently performing random hiding in the later phase of iteration. The energy of the rabbit is what drives the mechanism but it shrinks over the course of the iterations. Therefore, the energy factor in ARO is formulated as follows:

$$A(t) = 4 \left(1 - \frac{t}{T} \right) \ln \frac{1}{r} \quad (27)$$

An energy factor is calculated to regulate the transition from exploration to exploitation in ARO. The parameter r represents a random variable. In ARO, when the energy factor $A(t) > 1$, the rabbit tends to search different foraging spaces randomly within the phase of the exploration.

```

Randomly initialize a set of rabbits  $X_i$  (solutions) and evaluate their fitness  $F_i t_i$  and  $X_{best}$  is the best solution found so far
While the stop criterion is not satisfied do
  For each individual  $X_i$  do
    Calculate the energy factor  $A$  using Eq. (27).
    If  $A > 1$ 
      Choose a rabbit randomly from other individuals.
      Calculation  $R$  using Eqs. (14)-(18)
      Perform detour foraging using Eq. (13)
      Calculate the fitness  $F_i t_i$ 
      Update the position of the current individual using Eq. (26)
    Else
      Generate  $d$  burrows and randomly pick one as hiding using Eq. (25)
      Perform random hiding using Eq. (23).
      Calculate the  $F_i t_i$ 
      Update the position of the individual using Eq. (26).
    End if
  End For
  Update the best solution found so far  $X_{best}$ 
End While
Return  $X_{best}$ 

```

Figure 3. The pseudocode of the ARO method

2.5.2. Lightning search algorithm (LSA)

One of the newest metaheuristic algorithms developed by Shareef et al., (2015) has been crafted from the lightning phenomenon. The application of this method is cast across numerous fields of research and inventions such as computer science, engineering, and mathematics, to mention but a few. The idea of lightning can be attributed to the gaseous atoms namely; nitrogen, oxygen, and hydrogen in the thundercloud. As water molecules freeze within the thundercloud, the parts that cannot incorporate into the lattice, are propelled at high velocities. Imagine these ejected particles as tiny seeds “Just as seeds provide the foundation for plant development, these high-speed projectiles create the initial ionized channel that facilitates the step leader’s progression, ultimately leading to a lightning strike”. As they travel through the air, they collide with other molecules, creating a pathway for the lightning bolt to follow. This initial pathway is like the first step in creating the lightning bolt, similar to how the first seeds planted in a field are the starting point for a garden. The flowchart of the LSA is given in Figure 4.

$$V_p = [1 - (\frac{1}{\sqrt{1 - (\frac{V_0}{c})^2}} - sf_i/mc^2)^{-2}]^{-1/2} \quad (28)$$

Where V_p and V_0 are the final and initial velocity of the projectile; c is the speed of light; f_i is the constant ionization rate; m is the mass of the projectile; and s is the length of the path traveled. Equation (28) proves that the projectile velocity is a function of leader tip position and projectile mass. Henceforth, Hydrogen with the lower atomic mass has little potential to ionize or explore a large space compared to Oxygen. Therefore, the exploration and exploitation capabilities of the algorithm can be guided using the relative energies of the step leaders.

To improve the algorithm’s exploration capabilities, the concept of “forking” is designed. Projectile emits two symmetrical channels similar to the phenomenon of lightning forking. In this algorithm, forking is defined in two ways. Equation (29) presents the mathematical expression of the symmetrical channels that define nuclei collision which leads to the creation of symmetrical channels.

$$\vec{p}_i = x + y - p_i \quad (29)$$

Where \vec{p}_i and p_i are the opposite and original projectiles, and x and y are the boundary limits in one dimension. This mechanism aims to improve the quality of less successful solutions within the population. Otherwise, one of the channels at the forking tip emerges to balance the c . Equation (30) demonstrates that the shaping parameter (α) exerts a significant influence over the trajectory. In the lightning search algorithm, the value of α for a specific space projectile p^s is dynamically determined by its distance from the current lead projectile P^l . This distance-dependent relationship directly influences the movement of the space projectile, as expressed;

$$p_{i_{new}}^s = p_i^s \pm \text{exprand}(\alpha_i) \quad (30)$$

If the calculated new position P_{new}^s of the space projectile is negative, it indicates a movement in the opposite direction. However, simply moving in the opposite direction doesn’t guarantee successful channel formation. For successful propagation, the space projectile’s energy $E_{p_i}^s$ must exceed the energy of the existing step leader E_i^{sl} . Only then can the space projectile extend the existing channel. If the new position $P_{i_{new}}^s$ leads to a successful channel extension, the corresponding step leader s_i^l is extended to this new position, and the space projectile’s position is updated accordingly. Otherwise, both the space projectile and the step leader remain in their previous positions. If a particular space projectile successfully extends the step leader beyond the current longest leader in the system, it is then designated as the new lead projectile. Following Shareef et al., (2015), Analogous to the generation of space projectiles, the position of the lead projectile can be updated probabilistically. This update incorporates a random component generated from a normal distribution. The probability density function of the normal distribution can be expressed as:

$$f(x^l) = \frac{1}{\sigma\sqrt{n\pi}} e^{-\frac{(x^l-\alpha)^2}{2\sigma^2}} \quad (31)$$

Equation (31) demonstrates that the shaping parameter (α) significantly influences the directional exploration of the space projectile. In the LSA context, the parameter α^i for a specific space projectile P_i^s is dynamically determined by its proximity to the current lead projectile. This distance-dependent parameter governs the search behavior of the space projectile, influencing its movement within the solution space. The position of the space projectile P_i^s as shown in (32) at the subsequent step can be mathematically expressed as

$$P_{i_{new}}^L = p_i^L \pm \text{normrand}(\mu_L, \sigma_L) \quad (32)$$

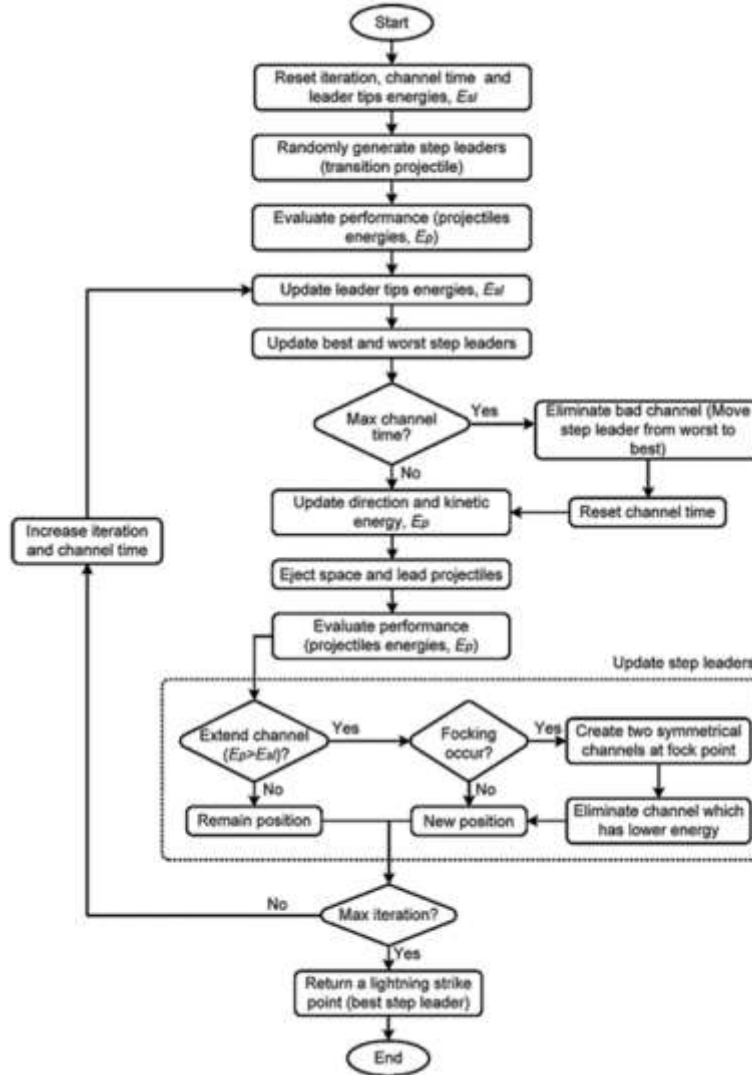


Figure 4. Flowchart of the LSA (Shareef et al., 2015)

2.5.3. Whale optimization algorithm (WOA)

Humpback whales' bubble-net feeding is a stunning display of cooperation and ingenuity in the natural world, as illustrated in Figure 5. This fascinating behavior involves whales diving beneath a school of fish and swimming in a spiral while releasing bubbles, creating a net that corrals the fish and forces them towards the surface. Inspired by this remarkable feeding strategy, WOA has been developed as a computational technique to solve complex optimization problems (Mirjalili and Lewis, 2016). This algorithm is designed based on the nature and tactics used by a whale to hunt and can be classified into three methodologies: encircling prey, bubble-net

attacking method, and searching for prey. These methodologies were used in designing the algorithm based on the following equations:

$$\vec{P} = |\vec{Q} \cdot \vec{R} * (t) - \vec{R}(t)| \quad (33)$$

$$\vec{R}(t+1) = \vec{R} * (t) - \vec{V} \cdot \vec{W} \quad (34)$$

where t denotes the current iteration, the vectors ' V ' and ' Q ' are coefficient vectors that dynamically adjust throughout the optimization process. ' R ' represents the position vector of the current best solution within the search space. The operation ' $|$ ' signifies the absolute value, while ' \cdot ' Denotes element-wise multiplication. It is crucial to note that the ' R ' vector must be updated iteratively to reflect the discovery of any superior solutions during the optimization process.

$$\vec{V} = 2\vec{a} \cdot \vec{r} - \vec{a} \quad (35)$$

$$\vec{Q} = 2 \cdot \vec{r} \quad (36)$$

where \vec{r} is a random vector, and \vec{a} is linearly decreasing within the iteration from 2 to 0. The WOA mimics the bubble-net feeding behavior by employing mathematical models to simulate the whales' spiral and bubble-net patterns, effectively navigating through a search space to locate optimal solutions. This tactic can be categorized into two ways; shrinking encircling or spiral updating position. Just as the whales' coordinated efforts result in successful feeding, the WOA's iterative process and intelligent mechanisms aim to achieve high-quality solutions in various scientific and engineering applications. The pseudo-code of the WOA algorithm is given in Figure 6 (Mirjalili and Lewis, 2016).

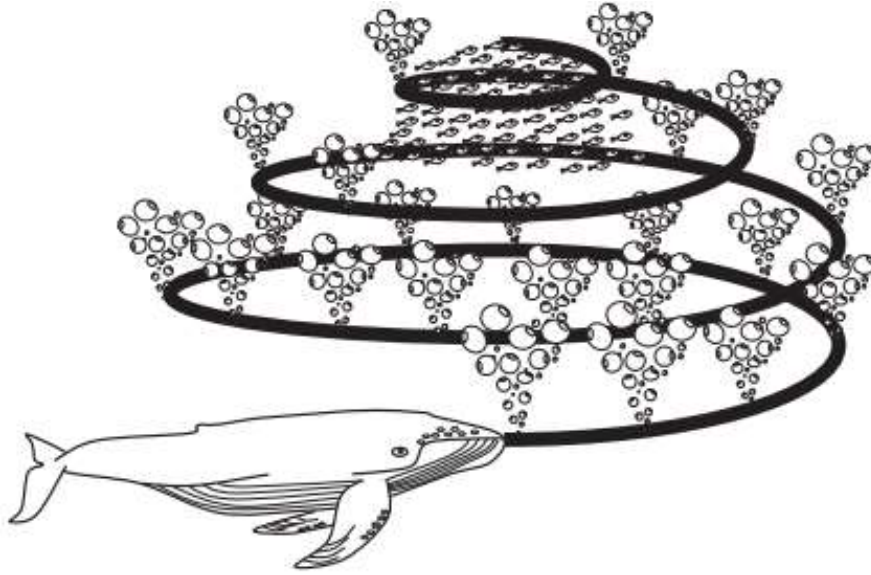


Figure 5. A bubble-net feeding behavior of humpback whales (Mirjalili and Lewis, 2016)

Shrinking encircling tactic is achieved by gradually reducing the magnitude of the coefficient vector ' V ' in (35). Concurrently, the range of possible values for ' V ' is also diminished by a factor of ' a ' within the interval $[-a, a]$, where the value of ' a ' decreases linearly from 2 to 0 throughout the iterative process. The search space is progressively narrowed down by confining the value of ' a ' within this decreasing range. Consequently, the new position of a search agent can be determined within a region bounded by its original position and the position of the current best solution. The potential positions are within the bounded region for a two-dimensional space. Assuming $0 \leq V \leq 1$. Spiral updating position tactic is inspired by the unique foraging behavior of humpback whales. This phase involves calculating the Euclidean distance between the current position of the whale (R, Y) and the position of the prey (R, Y). Subsequently, a spiral equation is derived to simulate the helical movement of the whale toward the prey, mirroring the observed behavior of humpback whales during bubble-net feeding.

$$\vec{R}(t+1) = \vec{W} \cdot e^{bl} \cdot \cos(2\pi l) + \vec{R} * (t) \quad (37)$$

Where $\vec{P} = |\vec{R} * (t) - \vec{R}(t)|$ and indicate the distance of the i^{th} whale to prey, b is a constant that defines the shape of the spiral, l is a stochastic number in $[-1,1]$, and $*$ is an element-by-element product.

The exploration phase of the WOA leverages variations in the V vector to simulate the process of prey searching. Humpback whales exhibit random search patterns based on their relative positions. In this context, V values greater than 1 or less than -1 are employed to drive search agents away from a reference whale, promoting diverse exploration. Unlike the exploitation phase, where the search agent updates their positions relative to the best solution found, the exploration phase updates based on a randomly selected search agent. This mechanism, combined with the condition $|\vec{V}| > 1$, enhances global search capabilities, ensuring broader exploration of the solution space. The corresponding mathematical model is as follows:

$$\vec{P} = |\vec{Q} \cdot \overrightarrow{R_{rand}} - \vec{R}| \quad (38)$$

$$\vec{R}(t+1) = \overrightarrow{R_{rand}} - \vec{V} \cdot \vec{P} \quad (39)$$

where $\overrightarrow{R_{rand}}$ is a random position vector chosen from the current position

```

Initialize the whale population  $R_i$  ( $i = 1, 2, \dots, n$ )
Calculate the fitness of each search agent
 $R^*$  = the best search agent
While ( $t < \text{maximum number of iterations}$ )
    For each search agent
        Update  $V, w, C, l$ , and  $a$ 
        if 1 ( $w < 0.5$ )
            if 2 ( $|V| < 1$ )
                Update the position of the current search agent by Eq. (33)
            Else if 2 ( $|V| \geq 1$ )
                Select a random search agent ( $R_{rand}$ )
                Update the position of the current search agent by Eq. (39)
            End if 2
        Else if 1 ( $w \geq 0.5$ )
            Update the position of the current search agent by Eq. (37)
        End if 1
    End for
    Check if any search agent goes beyond the search space, and amend it
    Calculate the fitness of each search agent
    Update  $R^*$  if there is a better solution
     $t = t + 1$ 
end while
return  $R^*$ 

```

Figure 6. Pseudo-code of the WOA algorithm (Mirjalili and Lewis, 2016)

3. Results and Discussion

3.1. Case I

In this case study, the single area-system is operated with a conventional PID controller ($K_p = 8.6147, K_i = 10, K_d = 4.1436$) without any RES or ESS integration. This system is simulated under a perturbation of step load change of 0.2 p.u applied at 0 second. The comparison of the system's change in frequency with and

without PID controller is shown in Figure 7. It is noted that the system frequency has a steady-state value of -0.0096 p.u. at 9.6 seconds when the PID controller is not activated. With the proper tuning of the PID controller, zero steady-state error in frequency change is attained at 12 seconds. Figure 8 shows that the system's power output is stabilized at 0.2 p.u. in a duration of around 8.3 seconds, which is equivalent to the load demand. Without PID controller, it is observed that the system's power output remains below the load demand.

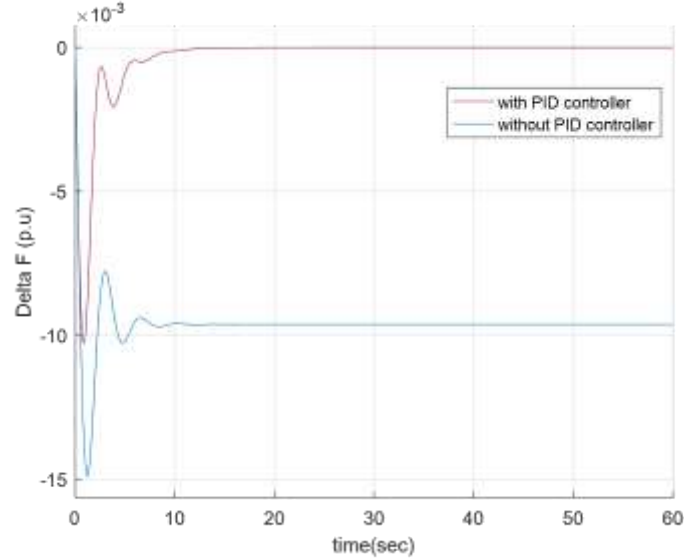


Figure 7. Comparison of the system's change in frequency with and without PID controller

Figure 7 presents the frequency deviation of the single-area under the influence of the PID controller, and the equivalent power output deviation under the same PID parameters is depicted in Figure 8.

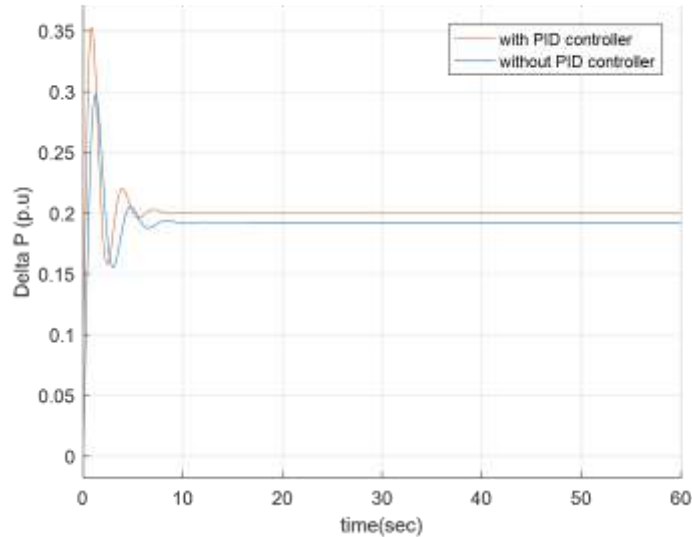


Figure 8. Comparison of the power output of the system with and without PID controller

It is clearly noted that the difference resulted in the output frequency and power stability at the nominal value in the shortest possible time due to the tuning effect of the PID controller. PID Tuning is important and an easier way to find the proper PID values.

3.2. Case 2

In this case study, PV and WT systems are added to the single-area system as shown in Figure 9. The system is exposed to severe load and irradiation variations as shown in Figure 10. At 2 s, the load increases from 0 to 0.1

p.u., then at 10 s, it drops to -0.05 p.u. The PID controller parameters are optimized using the aforementioned optimization methods (ARO, LSA, and WOA) which are simulated for 100 iterations, with 0 as the lower boundary and 10 as the upper boundary. For all, the population size is set as 50. The optimization results are presented in Table 3 when only PV system is activated. On the other hand, Table 4 shows the optimization results when only WT system is enabled. The optimization methods give the lowest settling time of 22.1 s for PV compared to 22.7 s for WT. Figure 11 compares three optimization methods for PID parameter tuning under constant irradiation. On the other hand, Figure 12 compares three optimization methods for PID parameter tuning under constant WT and variable load. In these figures, at 2s, the system experiences a big overshoot and the subsequent drop and a small overshoot at 10 s. ARO tuned PID controller causes fewer oscillations, the least settling time, and the smallest overshoot.

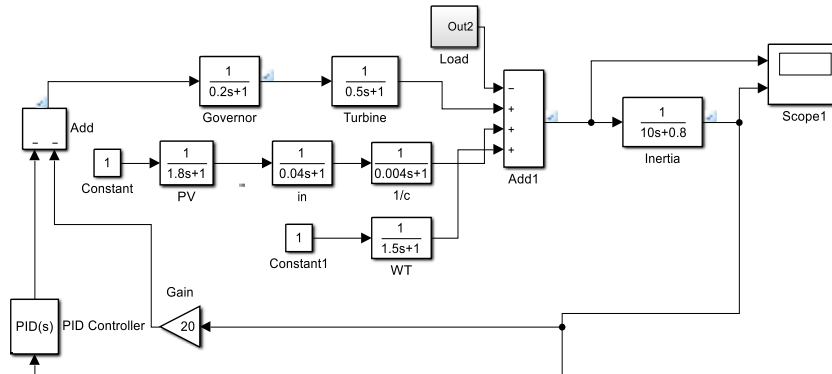


Figure 9. Transfer function representation of the single-area system with PV and WT integration

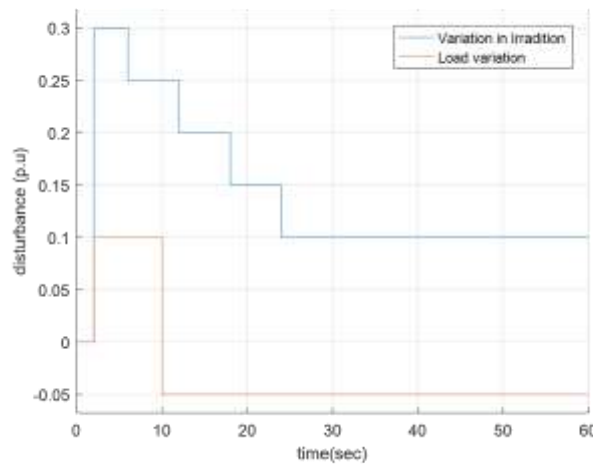


Figure 10. Load and irradiation variation applied to the system

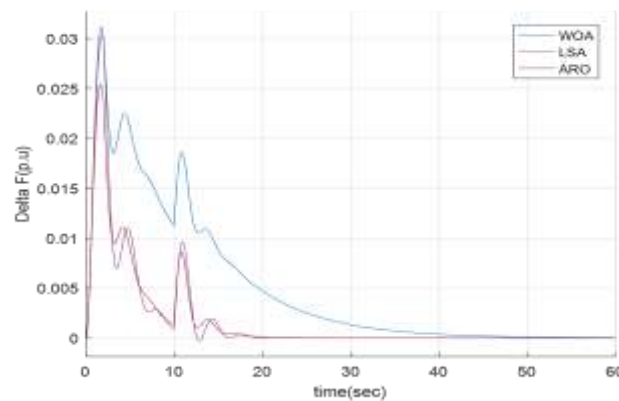


Figure 11. Comparison of ARO, LSA, and WOA under constant irradiation

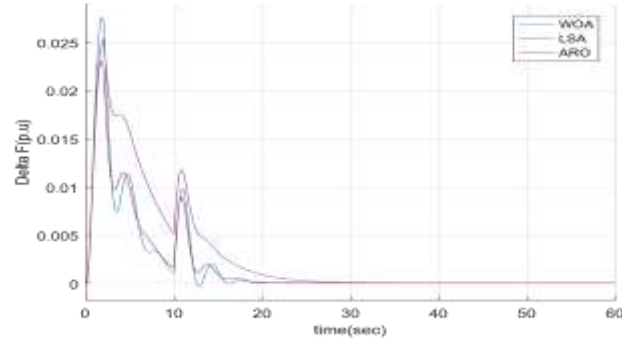


Figure 12. Comparison of ARO, LSA, and WOA under constant WT and variable load

Table 3. Optimization results for PID parameters for single-area system under constant irradiation

Optimization method	ITAE	Overshoot	undershoot	Settling time	PID parameters (K , K_i , and K_d)
ARO	0.5494	0.023	0	22.1	8.6147, 10, 4.1436
WOA	0.5269	0.028	-0.00038	22.1	4.7109, 9.8305, 1.7877
LSA	1.194	0.025	0	34	5.8375, 5.9462, 5.6458

Table 4. Optimization results for PID parameters for single-area system under constant wind speed

Optimization method	ITAE	Overshoot	Undershoot	Settling time	PID parameters (K , K_i , and K_d)
ARO	0.5174	0.025	0	22.7	8.8427, 10, 4.3477
WOA	3.21	0.0301	0	60	7.5469, 3.3712, 2.3995
LSA	0.5147	0.0312	0	23.2	4.3118, 9.4766, 1.8173

3.3. Case 3

The performance of the three optimization algorithms ARO, WOA, and LSA has been evaluated for a single-area power system integrated with constant PV and WT. The simulation results, shown in Table 5, highlighted the effectiveness of each optimization method in enhancing the system's stability by minimizing frequency deviations caused by load disturbances. ARO achieved the lowest integral time absolute error (ITAE) value of 0.5985, indicating superior performance in reducing the overall system error. Undershoot and overshoot are critical in evaluating system stability, as they indicate how much the system deviates from the desired steady-state frequency. While WOA has the lowest undershoot, the balance between undershoot and overshoot makes ARO more favorable in terms of overall stability. The proportional and integral gains are higher in ARO which contributes to faster system stability, while the derivative is tuned to reduce oscillations. Figure 13 shows the ARO curve with minimal oscillations and achieves steady-state frequency faster than the other two.

3.4. Case 4

The wind turbine is considered to have an input of white noise generating random numbers. This is closer to reality since the wind blows continuously and is unstable as shown in Figure 14. The solar irradiation is

increased to 0.3 p.u at 2 s according to Figure 13, and then began to decrease by -0.05 p.u step by step at 6, 12, 18, and 24 s until it is reduced to 0.1 p.u. Figure 15, shows the frequency response of the system, and all optimization methods respond well especially ARO as it shows better damping of oscillations compared to WOA and LSA, indicating faster adaptation to random noise and solar variations, and better frequency stability during the stepwise decrease in solar irradiation. LSA struggles to handle the noise effectively, leading to large and more persistent oscillation. WOA performs moderately well but shows slightly higher oscillation.

Table 5. Optimization results for PID parameters for single-area system under constant irradiation and constant wind speed

Optimization method	ITAE	Undershoot $\times 10^{-3}$	Overshoot $\times 10^{-3}$	Settling time	PID parameters (K , K_i , and K_d)
ARO	0.5985	0.454	4.944	15.12	10, 10, 3.0713
WOA	0.9747	0.026	4.59	17.1	9.4301, 6.5550, 6.2250
LSA	4.285	7.5	2.61	39.1	3.1908, 5.9219, 7.7052

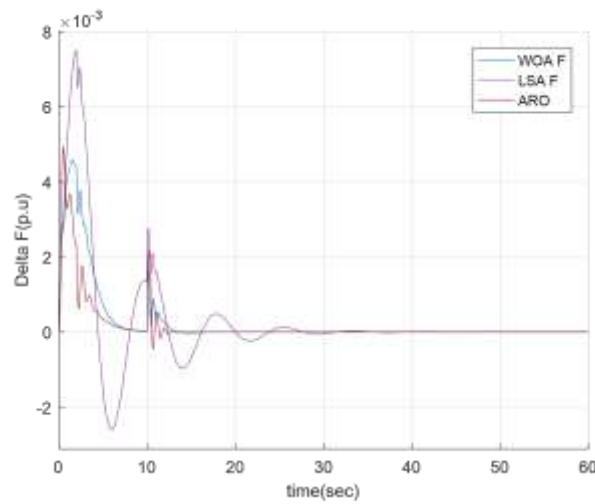


Figure 13. Comparison of ARO, WOA, and LSA under constant RES in a single-area system

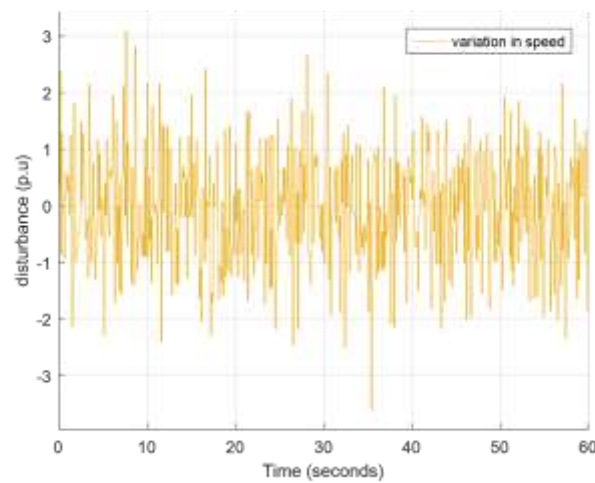


Figure 14. White noise is used as a variation in the speed of WT

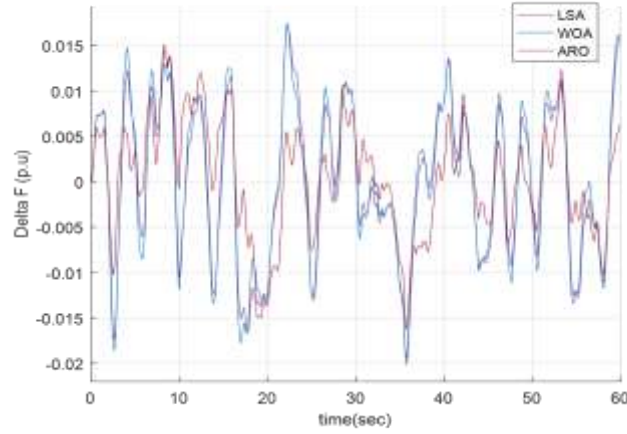


Figure 15. Comparison of ARO, LSA, and WOA under severe disturbances

3.5. Case 5

The two-area power system is simulated using the parameters listed in Table 1 in the following case studies. Several simulation scenarios are rendered to thoroughly investigate the system stability with respect to steady-state frequency and power output. The optimization performance of the aforementioned optimization methods on PID controller parameter tuning is also investigated. Different types of ESSs are employed in the system to play a stability control role. A load disturbance of 2% is applied in Area-1 and 1.5% in Area-2, each at 2 s. Figure 16 illustrates the steady-state frequency of the system in both areas. Long undershoots and short overshoots right at 2 s are observed, then the system reaches a steady-state condition at 21.8 s as indicated in Table 6. These results show the effectiveness of the LFC under an area control error strategy in which each load demand is compensated by the governor assigned to that area. On the other hand, Figure 17 shows the output power of the two-area system and the two overshoots at 2 s confirm the surge in the load in both areas. The subsequent steady-state at zero shows the system stability and effectiveness of the automatic LFC approach. To further enhance the system's stability and steady-state frequency, ESSs are tested to investigate their effects. Figures 18 and 19 present the steady-state frequency due to each ESS. Table 7 offers the performance indices, where the FESS has the shortest undershoot in both areas followed by BESS and then SMESS. The overshoots seem to die out except for SMESS, and the settling time is a disadvantage for all the ESSs. Figures 20 and 21 show the steady-state power output of both areas in response to the step load perturbation of 0.2 p.u for Area-1 delivered at 2 s and 0.15 p.u for Area-2 at 2 s. FESS shows a significant improvement in the overshoots of the system followed by BESS, SMESS as reported Table 7. However, the settling time is seen to be disadvantageous for the ESSs in both areas. in a nutshell, ESSs are seen to dampen the oscillations and increase the settling time. Figure 22 represents the tie-line steady-state power output due to the ESSs.

Table 6. Comparison of ESS performances on the two-area system

ESS type	Overshoot $\times 10^{-3}$		Undershoot $\times 10^{-3}$		Settling time (s)	
	Area-1	Area-2	Area-1	Area-2	Area-1	Area-2
No ESS	2.8	1.9	-14.6	-14.9	21.8	28.1
FESS	0	0	-8.3	-6.85	32.4	43.1
SMESS	0	-3	-10.1	-8.7	29.8	35.6
BESS	0	0	-8.8	-7.22	35.5	43.5

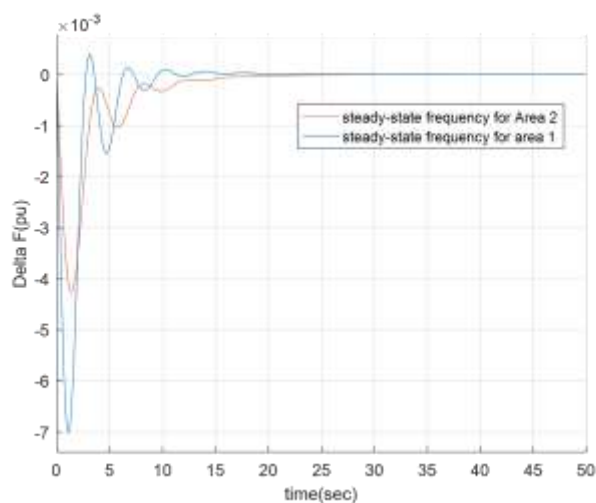


Figure 16. Frequency deviation of the system tested under different load surges in Areas 1-2

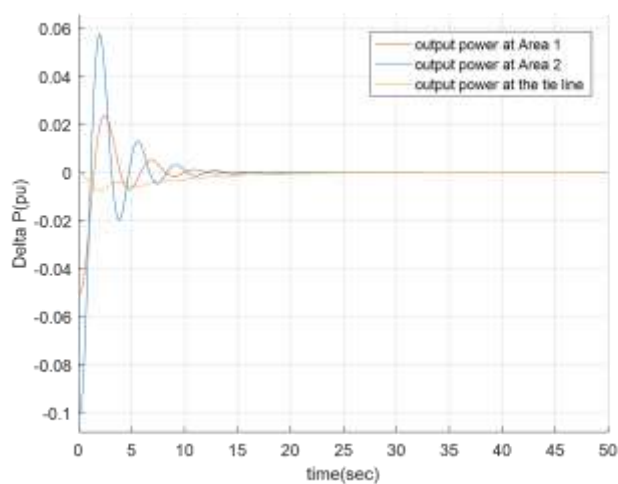


Figure 17. The power output produced by the two areas and the tie line

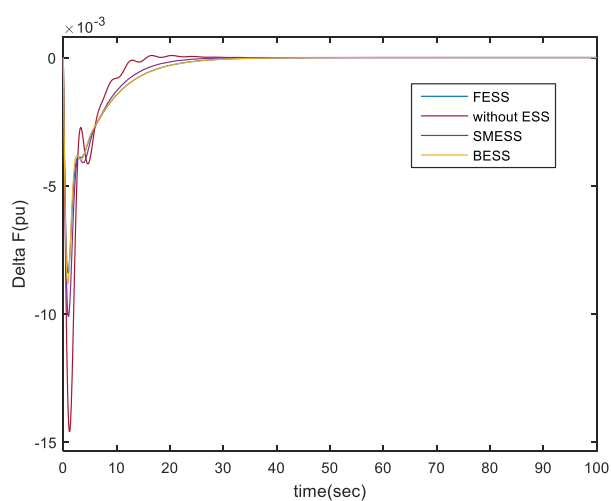


Figure 18. Comparison of the frequency deviation in Area-1 due to the ESS

Table 7. Comparison of power output parameters due to ESS

ESS type	Overshoot $\times 10^{-3}$		Undershoot $\times 10^{-3}$		Settling time (s)	
	Area-1	Area-2	Area-1	Area-2	Area-1	Area-2
No ESS	182	125	136	110	43.1	28.1
FESS	327	281	158	86	27.1	28.1
SMESS	220	159	148	120	35.6	28.1
BESS	187	127	132	107	43.1	28.1

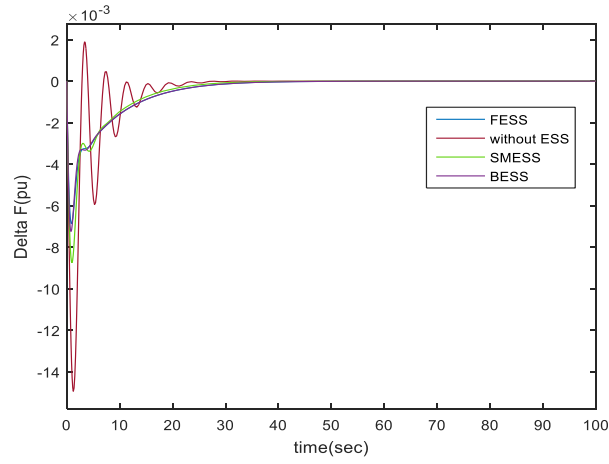


Figure 19. Comparison of frequency deviation in Area-2 due to ESS

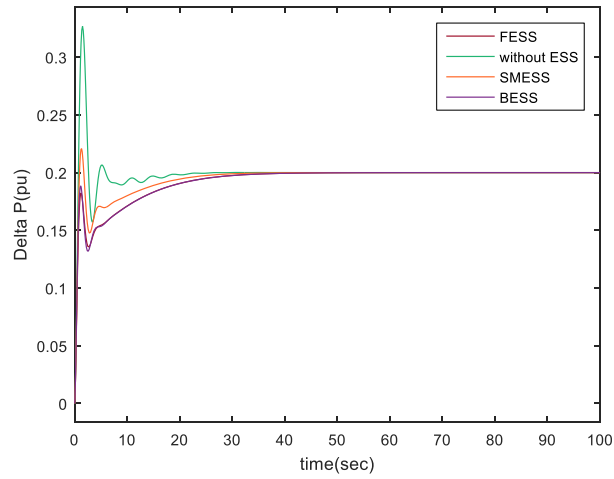


Figure 20. The power output due to ESS at Area-1

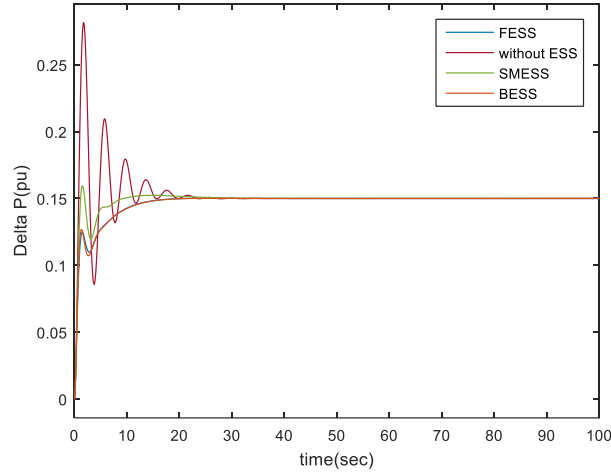


Figure 21. The power output due to ESS in Area-2

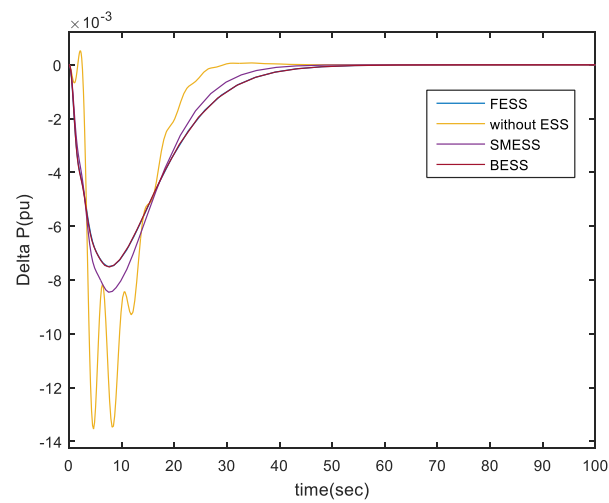


Figure 22. The tie-line steady-state power output due to the ESSs.

3.6. Case 6

RES, such as PV and WT systems, are activated in the two-area system. Figure 23 shows the model configuration. This study is evaluated based on the optimization techniques and the indices upon which the selection of the best technique depends is the popular error criteria namely “ITAE” and then the overshoot, undershoot as well as the settling time. The system responds to the significant load perturbation as illustrated in Figure 10. A load of 0.2 p.u delivered at 2s and the subsequent load value falls of 0.05 p.u. at 10 s. The overshoot at the corresponding times can be observed in Figures 24 and 25, representing Area-1 and 2. The ARO is seen to have a minimum ITAE of 0.2126 in Area-1 and 0.6035 in Area-2 compared to WOA and LSA as can be seen in Table 8. The ARO has also the least overshoot and undershoot in both areas. These results prove the superiority of ARO method on the overall basis compared to the LSA and WOA methods.

Table 8. Comparison of optimized parameters for the two-area system under constant RES

Optimization Method	ITAE1	ITAE2	Overshoot $\times 10^{-3}$		Undershoot $\times 10^{-3}$		Settling time (s)	
			Area-1	Area-2	Area-1	Area-2	Area-1	Area-2
LSA	0.4809	27.04	3.9	2.97	0	0	100	100
WOA	0.406	0.2221	8.1	3.93	-1.2	-0.24	16.9	26.4
ARO	0.2126	0.6035	2.4	2.22	-0.8	-0.42	29.8	21.4

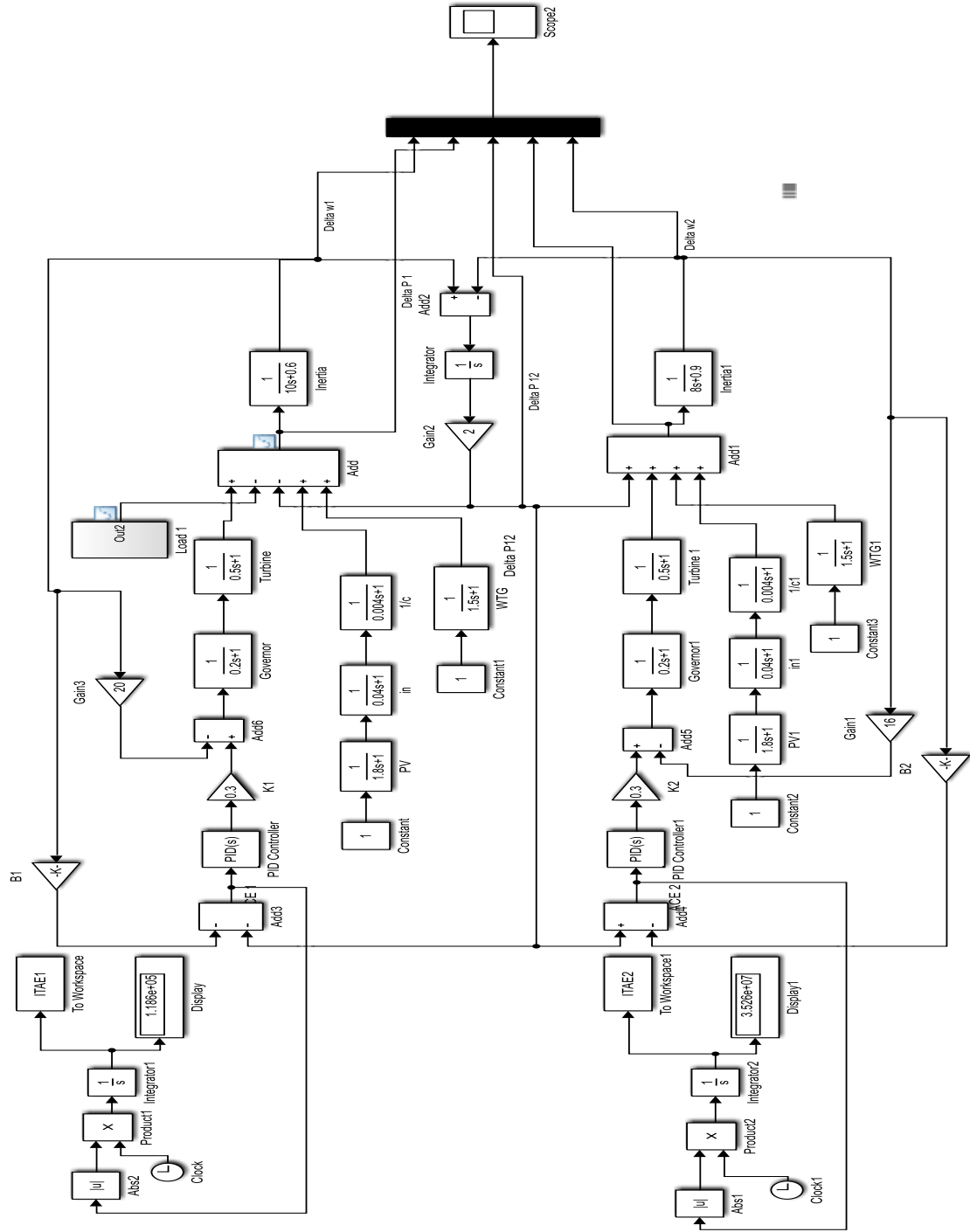


Figure 23. Renewable energy penetration with a constant input in both areas

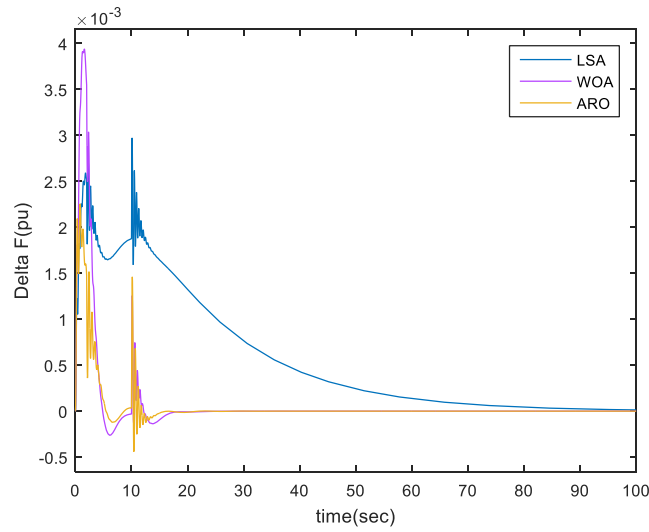


Figure 24. The frequency deviation of Area-1 under constant PV, WT, and variable load

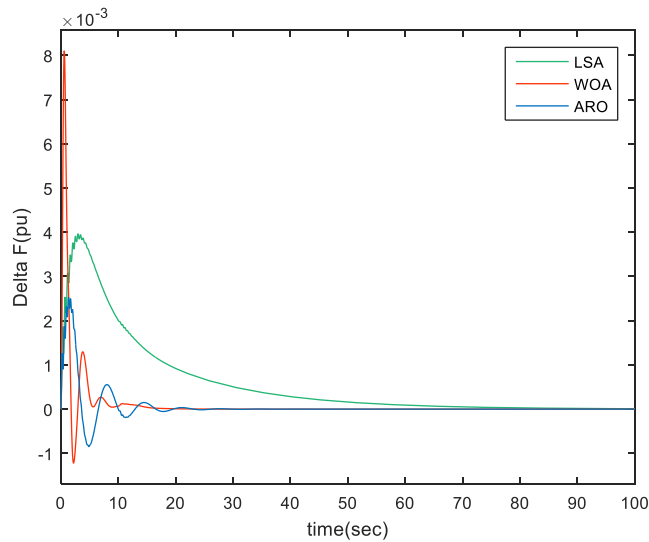


Figure 25. Comparison of frequency deviation of Area-2 under constant PV, WT, and no load

3.7. Case 7

The configuration of the overall system constituting PV, WT, and the load is shown in Figure 26. The main aim of this case is to examine the superiority of ARO in subduing a complex disturbance in the system due to the severe disturbances from the PV, WT, and the load as illustrated in Figure 27. The load surges at 2 s to 0.1 p.u and then drops to -0.05 p.u at 10 s. This fluctuation is reflected at the corresponding time in Figure 28 since the load is only applied to Area-1. Both PV and WT systems have a steady increment in disturbance of 0.05 p.u at 0,7,11,16 and 20 s. The only difference is that there is an abrupt fall of WT speed at 20 s to -0.05 p.u. Under these disturbances. The optimization techniques are applied to improve the PID controller parameters. Table 9 provides the quantitative analyses of Figures 28 and 29 which represent Area-1&2. The ARO method has the lowest ITAE of 0.3431 for Area-1 and 0.2642 for Area-2, providing a minimum settling time of 33.1 s.

Table 9. Parameters due to optimizations under variable load and ESS in both areas

Optimization Method	ITAE1	ITAE2	Undershoot $\times 10^{-4}$		Overshoot $\times 10^{-4}$		Settling time (s)	
			Area-1	Area-2	Area-1	Area-2	Area-1	Area-2
WOA	0.9458	0.5858	-10.3	-2.74	19.5	2.75	30.1	43.7
LSA	3.943	2.386	-5.6	-1.8	16.2	6.43	51.8	100
ARO	0.3431	0.2642	-9.5	-4.67	15.3	2.55	25	33.1

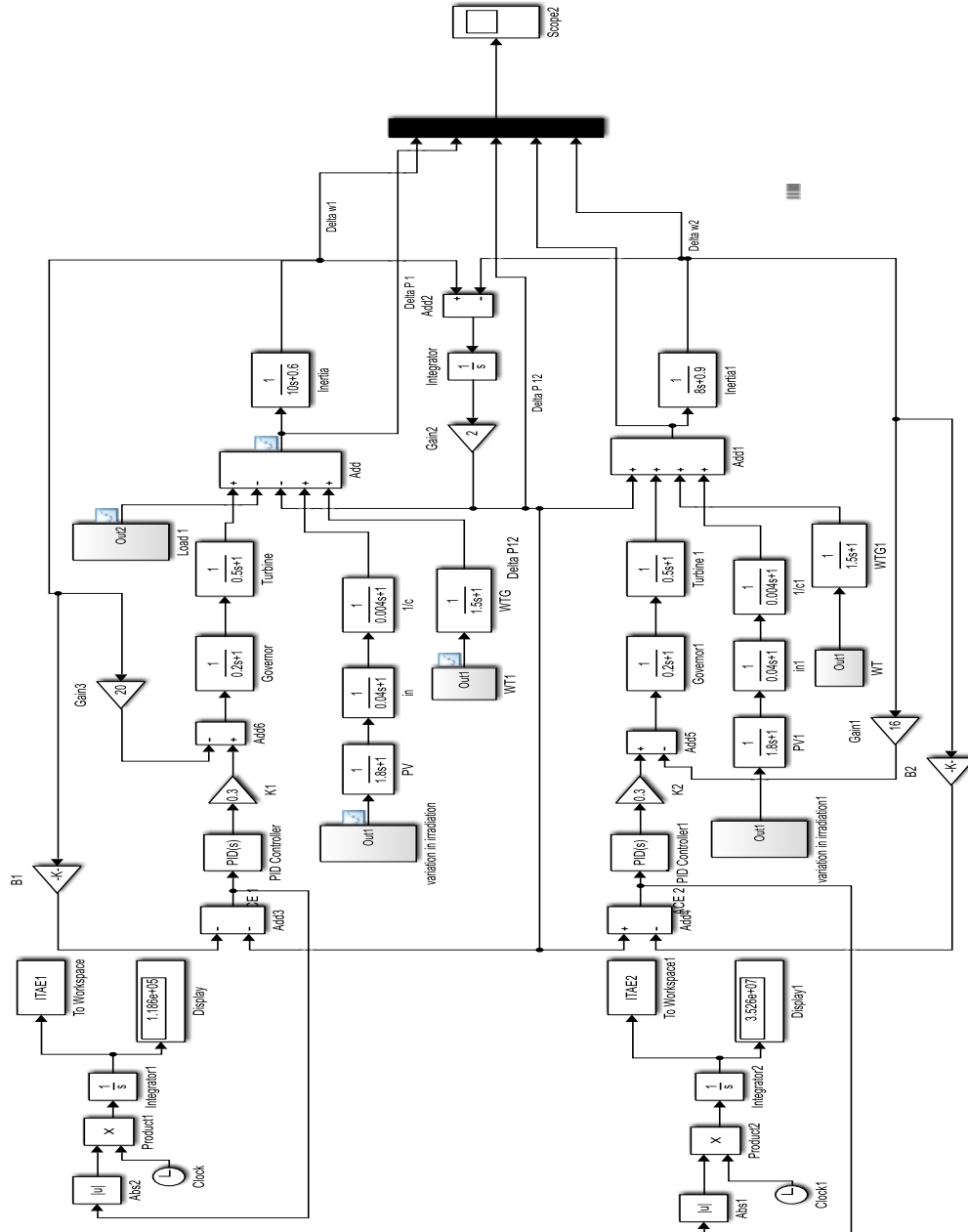


Figure 26. Integration of RES into the System model in both areas and Load disturbance in Area-1

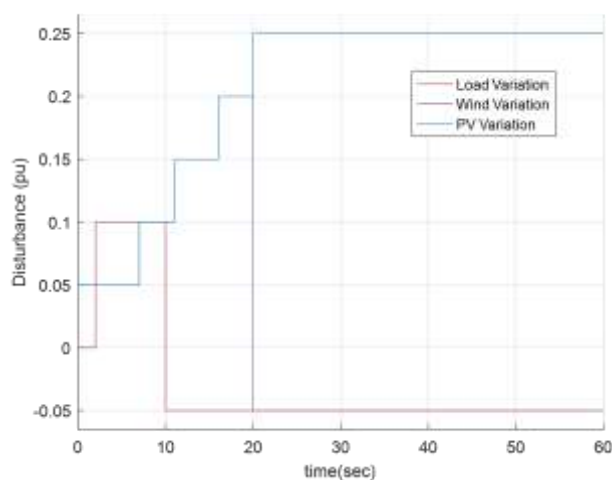


Figure 27. The disturbances applied to the system

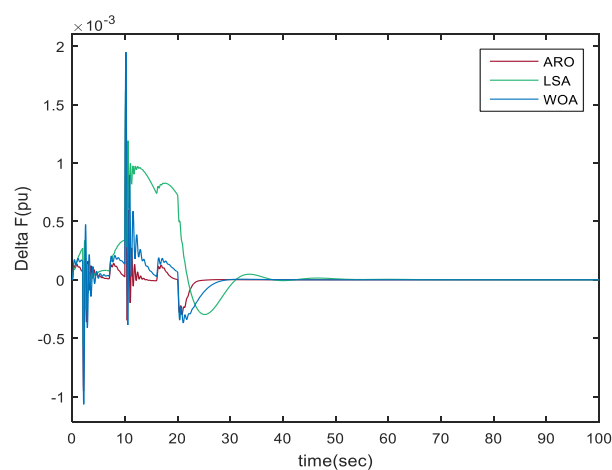


Figure 28. Comparison of frequency deviation optimizations in Area-1

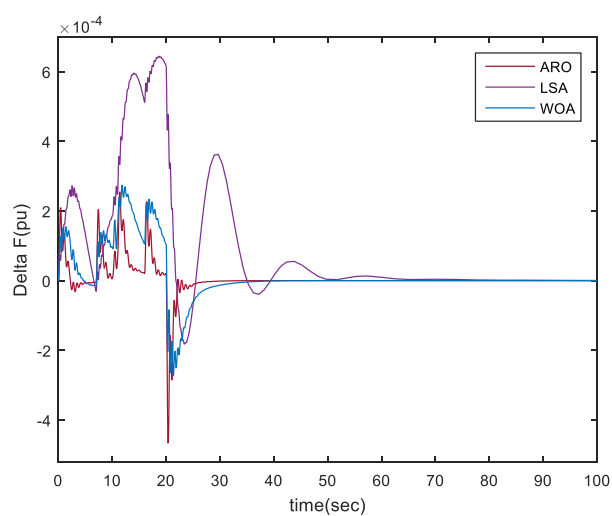


Figure 29. Comparison of frequency deviation optimizations in Area-2

3.8. Case 8

Under constant PV, WT, and variable load, the two-area system is tested by charging and discharging FESS. The responses are presented in Figures 30, 31, and 32. Also under variable load and RES conditions, the responses are illustrated in Figures 33, 34, and 35. Numerous research papers explore the technology of charging and discharging ESS. On the other hand, especially, FESS can be preferred due to its fast response and durability (Nguyen and Hoang, 2020). The smoother response of FESS in the charging phase can be compared to the discharging state. Both charging and discharging states are effective but the intrinsic characteristics of charging tend to result in smoother damping of oscillations (Canizares et al., 2021; Xie et al., 2023).

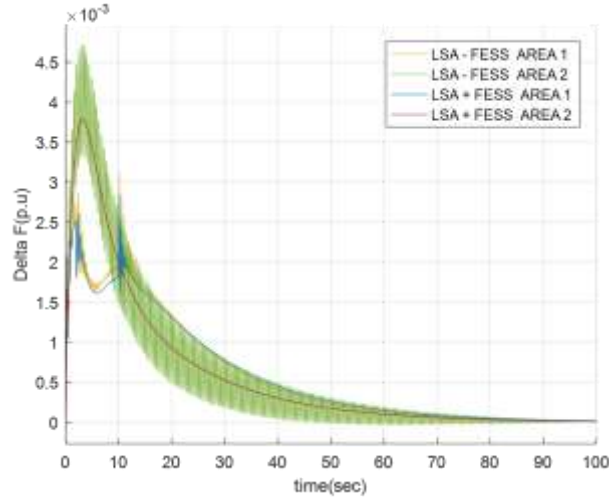


Figure 30. Frequency deviation comparison under LSA on charging and discharging of FESS

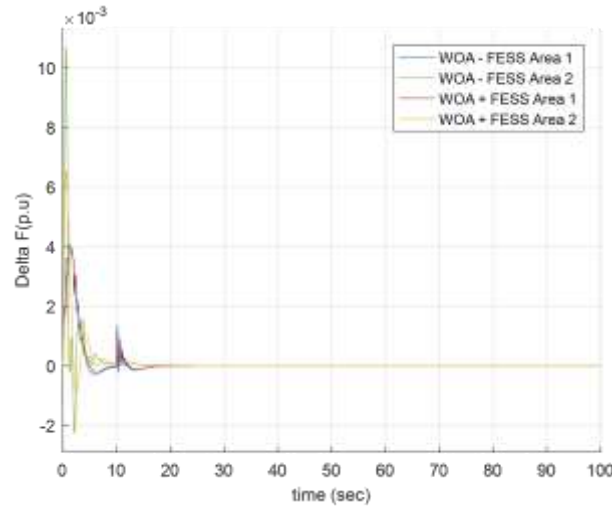


Figure 31. Frequency deviation comparison under WOA on charging and discharging of FESS

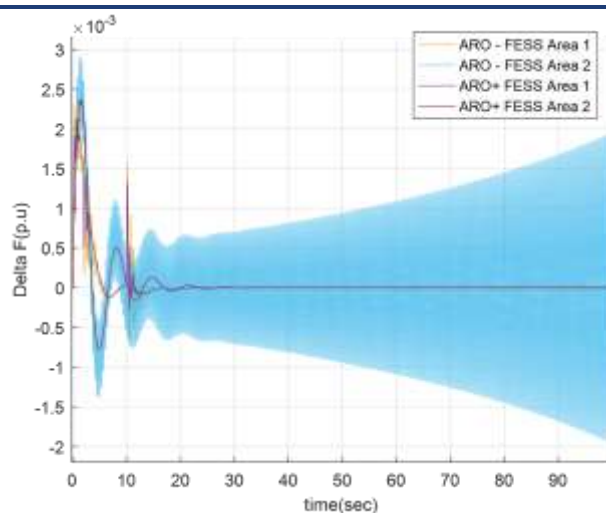


Figure 32. Frequency deviation comparison under ARO on charging and discharging of FESS

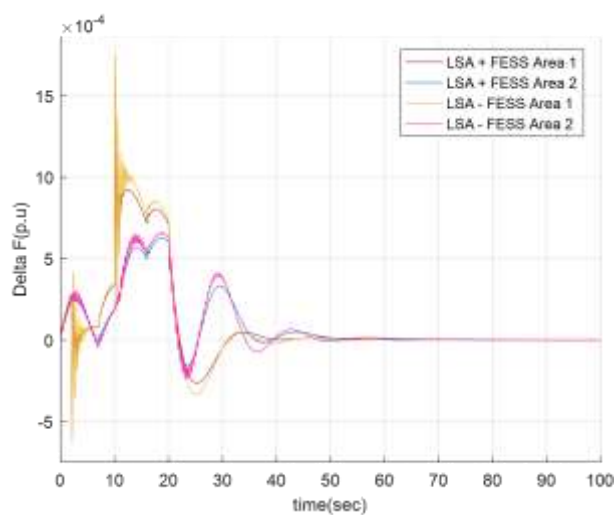


Figure 33. Frequency deviation comparison under LSA on charging and discharging of FESS

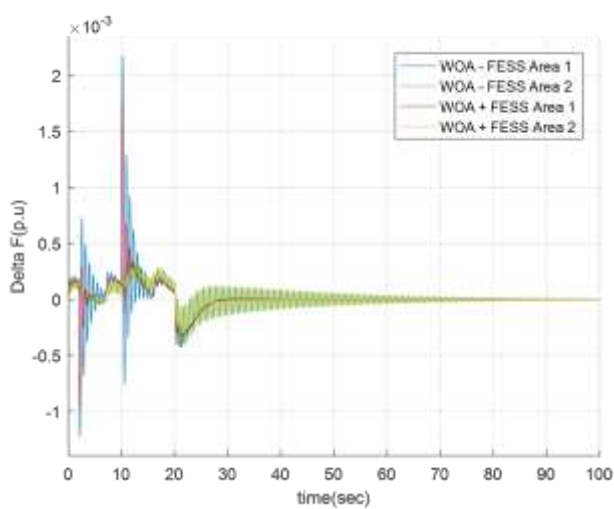


Figure 34. Frequency deviation comparison under WOA on charging and discharging of FESS

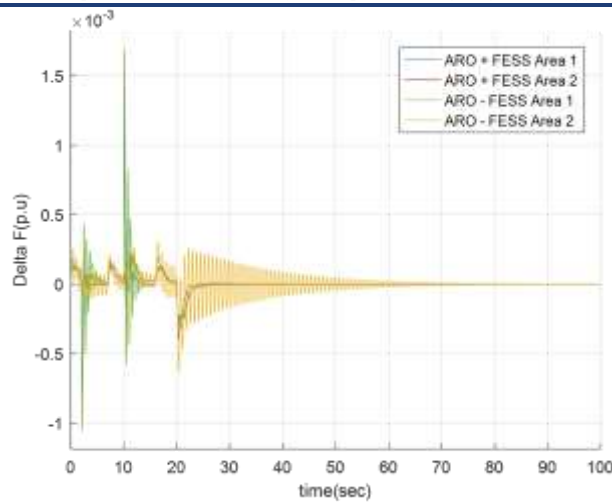


Figure 35. Frequency deviation comparison under ARO on charging and discharging of FESS

4. Conclusion

This study emphasizes the advantage of effective frequency regulation in modern power systems, especially with the increasing integration of RES, such as PV and WT systems. The variability and uncertainty in RES outputs, together with dynamic load changes, create significant challenges to maintaining system stability. This research evaluates the performance of three optimization methods (ARO, LSA, and WOA) to improve the tuning of PID controllers for frequency control in both single-area and two-area test systems. The findings demonstrate ARO's superior robustness in mitigating frequency instability caused by severe load perturbations and variable RES inputs. The study further highlights the impact of ESS such as BESS, FESS, and SMESS on system stability. The FESS stands out as the most effective ESS in reducing frequency oscillations and improving transient stability. However, all ESSs introduce a trade-off by increasing the system settling time. The combination of optimized PID control and ESS deployment offers a reliable solution to address the challenges posed by the variability of RES and dynamic load changes in power systems.

The overall deduction ascertains that there is no single “superior” energy storage system- each excels in different applications and economic feasibility. BESS has environmental concerns but is best for grid-scale energy storage. FESS has a high cost but supplies high power and a long lifespan. Finally, SMESS has high costs and cooling requirements but offers the highest efficiency.

Ethics Permissions

This paper does not require ethics committee approval.

Author Contributions

A. Garba Ibrahim conceived and designed the experiments; A. Mete Vural and A. Garba Ibrahim proposed the methods and analyzed the data; A. Garba Ibrahim drafted the manuscript. A. Mete Vural revised the manuscript and edited English language. All authors read and approved the final version.

Conflict of Interest

The authors declare that the research was conducted in the absence of any commercial or financial relationships that could be construed as a potential conflict of interest.

References

- Akram, U., Nadarajah, M., Shah, R., and Milano, F. (2020). A review on rapid responsive energy storage technologies for frequency regulation in modern power systems. *Renewable and Sustainable Energy Reviews*, 120, 109626. <https://doi.org/10.1016/j.rser.2019.109626>
- Ali, G., Aly, H., and Little, T. (2024). Automatic generation control of a multi-area hybrid renewable energy system using a proposed novel GA-fuzzy logic self-tuning PID controller. *Energies*, 17(9), 2000. <https://doi.org/10.3390/en17092000>

- Altayf, A., Trabelsi, H., Hmad, J., and Benachaiba, C. (2024). Multi-criteria decision-making approach to the intelligent selection of PV-BESS based on cost and reliability. *International Journal of Energy Production and Management*, 9(2), 83–96. <https://doi.org/10.18280/ijepm.090203>
- Cañizares, C. A., E, N. S. G., Bhattacharya, K., and Sohm, D. (2021). Frequency regulation model of bulk power systems with energy storage. *IEEE Transactions on Power Systems*, 37(2), 913–926. <https://doi.org/10.1109/TPWRS.2021.3108728>
- Hutchinson, A. J., Harrison, C. M., Bryden, T. S., Alahyari, A., Hu, Y., Gladwin, D. T., ... and Forsyth, A. (2025). A comprehensive review of modeling approaches for grid-connected energy storage technologies. *Journal of Energy Storage*, 109, 115057. <https://doi.org/10.1016/j.est.2024.115057>
- Cansiz, A., Faydaci, C., Qureshi, M. T., Usta, O., and McGuinness, D. T. (2017). Integration of a SMES–battery-based hybrid energy storage system into microgrids. *Journal of Superconductivity and Novel Magnetism*, 31(5), 1449–1457. <https://doi.org/10.1007/s10948-017-4338-4>
- El-Saady, G., Ibrahim, E. A., and Okilly, A. H. (2018). HVDC FACTS controller for load frequency control system. In *Proceedings of the Fourth International Conference on Energy Engineering (ICEE-4)*, Aswan University, Egypt.
- Elsisi, M., Aboelela, M., Soliman, M., and Mansour, W. (2018). Design of optimal model predictive controller for LFC of nonlinear multi-area power system with energy storage devices. *Electric Power Components and Systems*, 46(11–12), 1300–1311. <https://doi.org/10.1080/15325008.2018.1469056>
- Georgious, R., Refaat, R., Garcia, J., and Daoud, A. A. (2021). Review on energy storage systems in microgrids. *Electronics*, 10(17), 2134. <https://doi.org/10.3390/electronics10172134>
- Hajiaghahi, S., Salemnia, A., and Hamzeh, M. (2019). Hybrid energy storage system for microgrids applications: A review. *Journal of Energy Storage*, 21, 543–570. <https://doi.org/10.1016/j.est.2018.12.017>
- Ibraheem, M. I., Edrisi, M., Gholipour, M., and Alhelou, H. H. (2022). A novel frequency regulation in islanded microgrid using sliding mode control with disturbance observers considering storages and EVs. *Computers and Electrical Engineering*, 105, 108537. <https://doi.org/10.1016/j.compeleceng.2022.108537>
- Chakraborty, M. R., Dawn, S., Saha, P. K., Basu, J. B., and Ustun, T. S. (2022). A comparative review on energy storage systems and their application in deregulated systems. *Batteries*, 8(9), 124. <https://doi.org/10.3390/batteries8090124>
- Ibrahim, L. O., In-Young, C., Jang, Y., Shim, J. W., Sung, Y. M., Yoon, M., and Suh, J. (2022). Coordinated frequency control of an energy storage system with a generator for frequency regulation in a power plant. *Sustainability*, 14(24), 16933. <https://doi.org/10.3390/su142416933>
- Jaffal, H., Guanetti, L., Rancilio, G., Spiller, M., Bovera, F., and Merlo, M. (2024). Battery energy storage system performance in providing various electricity market services. *Batteries*, 10(3), 69. <https://doi.org/10.3390/batteries10030069>
- Julius, A., Corigliano, S., Merlo, M., and Dan, Z. (2022). BESS primary frequency control strategies for West African power pool. *Energies*, 15, 990. <https://doi.org/10.3390/en15030990>
- Ramesh Kumar, S., and Ganapathy, S. (2013). Design of load frequency controllers for interconnected power systems with superconducting magnetic energy storage units using bat algorithm. *IOSR Journal of Electrical and Electronics Engineering*, 6(4), 42–47.
- Khalil, A. E., Boghdady, T. A., Alham, M. H., and Ibrahim, D. K. (2023). Enhancing the conventional controllers for load frequency control of isolated microgrids using proposed multi-objective formulation via artificial rabbits optimization algorithm. *IEEE Access*, 11, 3472–3493. <https://doi.org/10.1109/ACCESS.2023.3234043>
- Li, M., Shan, R., Abdullah, A., Tian, J., and Gao, S. (2023). High energy capacity or high energy rating: Which is the more important performance metric for battery energy storage systems at different penetrations of variable renewables? *Journal of Energy Storage*, 59, 106560. <https://doi.org/10.1016/j.est.2022.106560>
- Lin, X., and Zamora, R. (2022). Controls of hybrid energy storage systems in microgrids: Critical review, case study and future trends. *Journal of Energy Storage*, 47, 103884. <https://doi.org/10.1016/j.est.2021.103884>
- Lu, R. (2022). Sustainability and environmental efficiency of superconducting magnetic energy storage (SMES) technology. *Highlights in Science, Engineering and Technology*, 26, 365–371. <http://dx.doi.org/10.54097/hset.v26i.4005>
- McIlwaine, N., Foley, A. M., Kez, D. A., Best, R., Lu, X., and Zhang, C. (2021). A market assessment of distributed battery energy storage to facilitate higher renewable penetration in an isolated power system. *IEEE Access*, 10, 2382–2398. <https://doi.org/10.1109/ACCESS.2021.3139159>

- Mirjalili, S., and Lewis, A. (2016). The whale optimization algorithm. *Advances in Engineering Software*, 95, 51–67. <https://doi.org/10.1016/j.advengsoft.2016.01.008>
- Moradi-Shahrbabak, Z., and Jadidoleslam, M. (2023). A new index for techno-economical comparison of storage technologies considering effect of self-discharge. *IET Renewable Power Generation*, 17, 1699–1712. <https://doi.org/10.1049/rpg2.12704>
- Mugyema, M., Botha, C. D., Kamper, M. J., Wang, R.-J., and Sebitosi, A. B. (2023). Levelised cost of storage comparison of energy storage systems for use in primary response application. *Journal of Energy Storage*, 59, 106568. <https://doi.org/10.1016/j.est.2022.106573>
- Nguyen, X. P., and Hoang, A. T. (2020). The flywheel energy storage system: An effective solution to accumulate renewable energy. In *2020 6th International Conference on Advanced Computing and Communication Systems (ICACCS)* (pp. 1322–1328). IEEE. <https://doi.org/10.1109/ICACCS48705.2020.9074469>
- Nguyen-Huu, T., Nguyen, V. T., Hur, K., and Shim, J. W. (2020). Coordinated control of a hybrid energy storage system for improving the capability of frequency regulation and state-of-charge management. *Energies*, 13(23), 6304. <https://doi.org/10.3390/en13236304>
- Oskouei, M. Z., Seker, A. A., Tunçel, S., Demirbaş, E., Gözel, T., Hocaoglu, M. H., ... and Mohammadi-Ivatloo, B. (2022). A critical review on the impacts of energy storage systems and demand-side management strategies in the economic operation of renewable-based distribution network. *Sustainability*, 14, 2110. <https://doi.org/10.3390/su14042110>
- Patel, V., Guha, D., and Purwar, S. (2019). Frequency regulation of an islanded microgrid using integral sliding mode control. In *2019 8th International Conference on Power Systems (ICPS)* (pp. 1–6). IEEE. <https://doi.org/10.1109/ICPS48983.2019.9067402>
- Peralta, D., Canizares, C., and Bhattacharya, K. (2021). Practical modeling of flywheel energy storage for primary frequency control in power grids. In *2021 IEEE Power and Energy Society General Meeting (PESGM)* (pp. 1–5). IEEE. <https://doi.org/10.1109/PESGM.2018.8585844>
- Qu, H., and Ye, Z. (2023). Comparison of dynamic response characteristics of typical energy storage technologies for suppressing wind power fluctuation. *Sustainability*, 15(3), 2437. <https://doi.org/10.3390/su15032437>
- Ray, P. K., and Mohanty, A. (2019). A robust firefly–swarm hybrid optimization for frequency control in wind/PV/FC based microgrid. *Applied Soft Computing*, 85, 105823. <https://doi.org/10.1016/j.asoc.2019.105823>
- Rouniyar, A., and Karki, M. (2021, October). Energy management system for hybrid PV-Wind-Battery based standalone system. In *Proceedings of the 10th IOE Graduate Conference*. (pp. 131–138). <https://conference.ioe.edu.np/ioegc10/papers/ioegc-10-018-10024.pdf>
- Saadat, H. (2002). *Power system analysis* (2nd ed.). McGraw-Hill.
- Sahu, R. K., Gorripotu, T. S., and Panda, S. (2015). Automatic generation control of multi-area power systems with diverse energy sources using Teaching Learning Based Optimization algorithm. *Engineering Science and Technology, an International Journal*, 19(1), 113–134. <http://dx.doi.org/10.1016/j.jestech.2015.07.011>
- Santhi, R. V., Sudha, K., and Devi, S. P. (2013). Robust load frequency control of multi-area interconnected system including SMES units using type-2 fuzzy controller. In *2022 IEEE International Conference on Fuzzy Systems (FUZZ-IEEE)* (Vol. 5, pp. 1–7). <https://doi.org/10.1109/FUZZ-IEEE.2013.6622324>
- Sassi, A., Zaidi, N., Nasri, O., and Slama, J. B. H. (2017). Energy management of PV/wind/battery hybrid energy system based on batteries utilization optimization. In *2017 International Conference on Green Energy Conversion Systems (GECS)* (pp. 1–7). <https://doi.org/10.1109/GECS.2017.8066133>
- Shareef, H., Ibrahim, A. A., and Mutlag, A. H. (2015). Lightning search algorithm. *Applied Soft Computing*, 36, 315–333. <https://doi.org/10.1016/j.asoc.2015.07.028>
- Simpa, N. P., Solomon, N. N. O., Adenekan, N. O. A., and Obasi, N. S. C. (2024). The safety and environmental impacts of battery storage systems in renewable energy. *World Journal of Advanced Research and Reviews*, 22(2), 564–580. <https://doi.org/10.30574/wjarr.2024.22.2.1398>
- Vishnuvardhan, V. Y., and Saravanan, B. (2023). Multimachine stability improvement with hybrid energy renewable system using a superconducting magnetic energy storage in power systems. *Journal of Energy Storage*, 57, 106255. <https://doi.org/10.1016/j.est.2022.106255>

- Wang, S., Li, F., Zhang, G., and Yin, C. (2022a). Analysis of energy storage demand for peak shaving and frequency regulation of power systems with high penetration of renewable energy. *Energy*, 267, 126586. <https://doi.org/10.1016/j.energy.2022.126586>
- Wang, L., Cao, Q., Zhang, Z., Mirjalili, S., and Zhao, W. (2022b). Artificial rabbits optimization: A new bio-inspired meta-heuristic algorithm for solving engineering optimization problems. *Engineering Applications of Artificial Intelligence*, 114, 105082. <https://doi.org/10.1016/j.engappai.2022.105082>
- Worku, M. Y. (2022). Recent advances in energy storage systems for renewable source grid integration: A comprehensive review. *Sustainability*, 14, 5985. <https://doi.org/10.3390/su14105985>
- Xie, D., Wei, X., Ning, Y., Yang, S., and Zhou, Z. (2023). Power system restoration method with the flywheel energy storage support. In *2023 8th International Conference on Power and Renewable Energy (ICPRE)* (pp. 1028–1032). <https://doi.org/10.1109/ICPRE59655.2023.10353641>
- Yao, J., Yu, M., Gao, W., and Zeng, X. (2016). Frequency regulation control strategy for PMSG wind-power generation system with flywheel energy storage unit. *IET Renewable Power Generation*, 11(8), 1082–1093. <https://doi.org/10.1049/IET-RPG.2016.0047>
- Zhang, K., Mo, J., Liu, Z., Yin, W., Wu, F., and You, J. (2025). Life cycle environmental and economic impacts of various energy storage systems: Eco-efficiency analysis and potential for sustainable deployments. *Integrated Environmental Assessment and Management*. <https://doi.org/10.1093/inteam/vjaf035>

New Approaches for Evaluation Indeterminate Limits for Multivariable Functions in Undergraduate Mathematics Courses

Çiğdem DİNÇKAL^{1*}

Keywords

*Zero divided by zero,
L'Hôpital rule,
Central finite
differences, Forward
finite differences,
Backward finite
differences,
Richardson
extrapolation method*

Abstract – Zero divided by zero is one of the most important indeterminate forms obtained when evaluating limits for single variable functions and series in calculus education. Well-known method; L'Hôpital rule and its generalized form have been employed to simplify and resolve the indeterminate form such that zero divided by zero in terms of quotients of their derivatives for single variable functions as well as for multivariable functions. Nevertheless, L' Hôpital rule is impractical for the indeterminate limit forms of two variable functions in some cases such that isolated and nonisolated singularities, requirement of application of L'Hôpital rule more than once and complexity of taking derivative for some multivariable functions. So L'Hôpital rule cannot be preferred due to these reasons. By considering all these facts, new approaches including Finite Differences such as Central (CFD), Forward (FFD), Backward (BFD), High Accurate Central (HACFD), High Accurate Forward (HAFFD), High Accurate Backward (HABFD) methods, and Richardson Extrapolation method are presented that provide efficient ways to solve these limits instead of using L' Hôpital rule. Error analysis is also performed. All these methods are compared with each other in terms of accuracy and computational efficiency. It is observed that these approaches will be good alternatives instead of L'Hôpital rule for indeterminate form of two variable functions in calculus courses for both instructors and their students. Numerical examples are presented for this purpose.

1. Introduction

In calculus, the most famous and well-known method is L'Hôpital rule for evaluating the limits of indeterminate form: $0/0$, for single variable functions. It has been employed comprehensively in the literature for this purpose and also for various applications (Aczel, 1990; Cooke, 1988; Corona-Corona, 2018; Duran, 1992; Estrada and Pavlovic, 2017; Gordon, 2017; Hartig, 1991; Huang, 1988; Muntean, 1993; Popa, 1999; Shishkina, 2007; Spigler and Vianello, 1993; Szabo, 1989; Takeuchi, 1995; Tian, 1993; Vianello, 1992; Vyborny and Nester, 1989; Zlobec, 2012). Besides, another significant and feature topic of interest in calculus is multivariable functions and their indeterminate form such that $0/0$ (Fine and Kass, 1966; Ivlev, 2013; Young, 1910). L'Hôpital rule and its generalized form have been employed to overcome the complexity of indeterminate limit form: $0/0$ by use of differentiation of both numerator and denominator (Ivlev and Shilin, 2014; Lawlor, 2020).

These methods often involve complex and lengthy processes that take derivative for some multivariable functions, especially for isolated and non isolated singularities. So applying L'Hôpital rule becomes inefficient and impractical method in these cases. It is the first time that Zlobec (2012) used L'Hôpital rule without derivative by employing Lagrange multiplier for only $0/0$ indeterminate limit form for only single variable functions.

There is no other alternative numerical method instead of L'Hôpital rule taught in calculus courses for problem of indeterminate forms of multivariable functions in literature. This is why, new approaches including FFD, BFD, HAFFD, HABFD, CFD, HACFD techniques and Richardson Extrapolation methods (Chapra and Canale, 2010) are presented for the form: $0/0$ of two variable functions to overcome the complexity and impossibility of

^{1*}Corresponding Author. Ankara Medipol University, Ankara, Türkiye. E-mail: cigdem.dinckal@ankaramedipol.edu.tr  ORCID: 0000-0002-1201-0885

Citation: Dinçkal, Ç. (2025). New approaches for evaluation indeterminate limits for multivariable functions in undergraduate mathematics courses. Natural Sciences and Engineering Bulletin, 2(1), 56-74.

L'Hôpital rule and its generalized form in this study. For the first time in literature Dinçkal (2024) introduced and employed finite difference methods for the solution of indeterminate problems of single variable functions.

There are three ways to get more accurate results when employing finite difference methods. One of them is to decrease step size. Other one is to employ a higher order formula which uses more points. Another one is to use the results of these finite difference methods to get more accurate approximations. For this reason, Richardson Extrapolation methods based on these finite difference methods are proposed, described and also compared with other finite difference method results.

Taking derivative and using Lagrange multiplier are not required in all approaches. These numerical techniques with proper step size here can be applied to all indeterminate limits for two variable functions conveniently.

After description of the methods proposed, numerical results from various complicated two variable functions are presented to prove the applicability of them.

2. Materials and Methods

2.1. L'Hôpital rule

Well-known rule; L'Hôpital rule for two variables functions has some steps and shown as follows (Dinçkal, 2024; Ivlev and Shilin, 2014; Lawlor, 2020)

$$\lim_{(x,y) \rightarrow (x_0, y_0)} \frac{f(x,y)}{g(x,y)} \quad (1)$$

where $\lim_{(x,y) \rightarrow (x_0, y_0)} f(x,y) = 0$ or a number and $\lim_{(x,y) \rightarrow (x_0, y_0)} g(x,y) = 0$. So one should take partial derivative with respect to x and y , at points (x_0, y_0) respectively (Ivlev and Shilin, 2014; Lawlor, 2020)

$$\frac{f_x(x_0, y_0)}{g_x(x_0, y_0)} \quad (2a)$$

$$\frac{f_y(x_0, y_0)}{g_y(x_0, y_0)} \quad (2b)$$

Provided that (2a) should be equal to (2b) such that

$$\frac{f_x(x_0, y_0)}{g_x(x_0, y_0)} = \frac{f_y(x_0, y_0)}{g_y(x_0, y_0)} = k_1 \quad (3)$$

Currently, if indeterminate form is found again as a result of (3), second order partial derivatives should be taken (Ivlev and Shilin, 2014):

$$\frac{f_{xx}(x_0, y_0)}{g_{xx}(x_0, y_0)} = \frac{f_{xy}(x_0, y_0)}{g_{xy}(x_0, y_0)} = \frac{f_{yx}(x_0, y_0)}{g_{yx}(x_0, y_0)} = \frac{f_{yy}(x_0, y_0)}{g_{yy}(x_0, y_0)} = k_2 \quad (4)$$

L'Hôpital rule for multivariable functions confirms the rules of partial derivation. So this method can be considered as being one more rule of partial derivation. However, this approach remains inadequate for isolated and non-isolated singularities.

2.2. Numerical methods

In some cases such as isolated and non isolated singularities, taking derivative is ineffective and impractical. Furthermore, sometimes, it is required to apply L'Hôpital rule more than once to overcome indeterminate limits. For this reason, new approaches including CFD, HACFD, FFD, HAFFD, BFD, HABFD and Richardson Extrapolation methods are proposed in this paper, correspondingly.

The assumptions have been made by changing x variable and not changing y variable in Taylor series expansions for all proposed methods. On the contrary, changing y variable and not changing x variable in Taylor series expansions do not change the results.

The originating idea of CFD, HACFD, FFD, HAFFD, BFD and HABFD techniques is based on well-known Taylor series.

2.2.1. CFD, HACFD, indeterminate limit formulations based on CFD and HACFD

Taylor series for forward form can be formulated as follows: by defining a step size $h = x_{i+1} - x_i$ and expressing as

$$(x_{i+1}, y) = f(x_i, y) + f'(x_i, y)h + \frac{f''(x_i, y)}{2!}h^2 + \frac{f^{(3)}(x_i, y)}{3!}h^3 + \dots + \frac{f^{(n)}(x_i, y)}{n!}h^n + R_n \quad (5)$$

The remainder term for variables x and y is defined as

$$R_n = \frac{f^{(n+1)}(\varepsilon_1, \varepsilon_2)}{(n+1)!}h^{n+1} \quad (6)$$

The term in (6) corresponds to $O((x_{i+1} - x_i)^{n+1}, (y_{i+1} - y_i)^{n+1})$ which is $O(h^{n+1})$ called as error.

For backward form, Taylor series in (5) can be formulated as

$$f(x_{i-1}, y) = f(x_i, y) - f'(x_i, y)h + \frac{f''(x_i, y)}{2!}h^2 - \frac{f^{(3)}(x_i, y)}{3!}h^3 + \dots \quad (7)$$

One of the ways to approximate the first derivative is to take differences of (7) and (5) to obtain:

$$f(x_{i+1}, y) = f(x_{i-1}, y) + 2f'(x_i, y)h + \frac{2f^{(3)}(x_i, y)}{3!}h^3 + \dots \quad (8)$$

This can be solved for

$$f'(x_i, y) = \frac{f(x_{i+1}, y) - f(x_{i-1}, y)}{2h} - \frac{f^{(3)}(x_i, y)}{3!}h^2 - \dots \quad (9)$$

Equation (9) can be also rewritten as

$$f'(x_i, y) = \frac{f(x_{i+1}, y) - f(x_{i-1}, y)}{2h} + O(h^2) \quad (10)$$

By substituting (10) into (3), one can get the combination of L'Hopital rule and CFD. As a result, one of the methods including CFD for solving indeterminate limit is formulated as

$$\lim_{(x,y) \rightarrow (x^*, y^*)} \frac{f(x, y)}{g(x, y)} = \frac{\frac{f(x_{i+1}^*, y) - f(x_{i-1}^*, y)}{2h} + O(h^2)}{\frac{g(x_{i+1}^*, y) - g(x_{i-1}^*, y)}{2h} + O(h^2)} \quad (11)$$

Both numerator and denominator in terms of CFD have errors which are $O(h^2)$. This demonstrates that errors are proportional to the square of the same step size for both $f(x, y)$ and $g(x, y)$. Error is of the order of h^2 in spite of the backward and forward approximations that are of the order of h . Therefore, Taylor series approximations yield the significant information that the centered formula is the most accurate demonstration of the derivative (Chapra and Canale, 2010; Dinçkal, 2024).

Level of accuracy depends on decreasing the step size and also increases the number of terms of the Taylor series. Hence, it is possible to reconstruct more accurate formulas called as HACFD by withholding more terms.

By substituting first order derivative in (10) into (5), CFD representation of the second order derivative based on error $O(h^2)$ can be found as

$$f''(x_i, y) = \frac{f(x_{i+1}, y) - 2f(x_i, y) + f(x_{i-1}, y))}{h^2} \quad (12)$$

Third order derivative based on error $O(h^2)$ by use of CFD:

$$f^{(3)}(x_i, y) = \frac{f(x_{i+2}, y) - 2f(x_{i+1}, y) + 2f(x_{i-1}, y) - f(x_{i-2}, y))}{2h^3} \quad (13)$$

To find the high-accurate form of first derivative based on error $O(h^4)$, one should use both (12) and (13), and substitute them into (5):

$$f(x_{i+1}, y) = f(x_i, y) + f'(x_i, y)h + \frac{f(x_{i+1}, y) - 2f(x_i, y) + f(x_{i-1}, y))}{2!}h^2 + \frac{f(x_{i+2}, y) - 2f(x_{i+1}, y) + 2f(x_{i-1}, y) - f(x_{i-2}, y))}{3!}h^3 + \dots$$

(14)

So $f'(x_i)$ based on error $O(h^4)$ can be obtained from (14) which is

$$f'(x_i, y) = \frac{-f(x_{i+2}, y) + 8f(x_{i+1}, y) - 8f(x_{i-1}, y) + f(x_{i-2}, y))}{12h} + O(h^4)$$

(15)

By use of (15) and put into (3), one can get the final form of transition of L'Hopital rule and HACFD. Finally, one of the methods including HACFD for solving indeterminate limit becomes

$$\lim_{(x,y) \rightarrow (x^*, y^*)} \frac{f(x, y)}{g(x, y)} = \frac{\frac{-f(x_{i+2}, y) + 8f(x_{i+1}, y) - 8f(x_{i-1}, y) + f(x_{i-2}, y))}{12h} + O(h^4)}{\frac{-g(x_{i+2}, y) + 8g(x_{i+1}, y) - 8g(x_{i-1}, y) + g(x_{i-2}, y))}{12h} + O(h^4)}$$

(16)

2.2.2. FFD, HAFFD, indeterminate limit formulations based on FFD and HAFFD

By recalling the formulation given in (5), first derivative by FFD based on $O(h)$ can be found as (Chapra and Canale, 2010)

$$f'(x_i, y) = \frac{f(x_{i+1}, y) - f(x_i, y)}{h} + O(h).$$

(17)

By use of (3) and (17), the transition from L'Hopital rule and FFD technique can be obtained. Solution for indeterminate limit is

$$\lim_{(x,y) \rightarrow (x^*, y^*)} \frac{f(x, y)}{g(x, y)} = \frac{\frac{f(x_{i+1}, y) - f(x_i, y)}{h} + O(h)}{\frac{g(x_{i+1}, y) - g(x_i, y)}{h} + O(h)}$$

(18)

By substituting first order derivative in (17) into (5), FFD representation of the second order derivative based on error $O(h^2)$ can be obtained as

$$f''(x_i, y) = \frac{f(x_{i+2}, y) - 2f(x_{i+1}, y) + f(x_i, y))}{h^2}$$

(19)

Third order derivative based on error $O(h^2)$ by use of FFD:

$$f^{(3)}(x_i, y) = \frac{f(x_{i+3}, y) - 3f(x_{i+2}, y) + 3f(x_{i+1}, y) - f(x_i, y))}{h^3}$$

(20)

To find the high-accurate form of first derivative by FFD based on error $O(h^2)$, one should employ both (19) and (20), and substitute them into (5):

$$f'(x_i, y) = \frac{-f(x_{i+2}, y) + 4f(x_{i+1}, y) - 3f(x_i, y))}{2h} + O(h^2)$$

(21)

By substituting (21) into (3), the transition from L'Hopital rule to HAFFD method can be obtained. So indeterminate limit formulation based on HAFFD become

$$\lim_{(x,y) \rightarrow (x^*, y^*)} \frac{f(x, y)}{g(x, y)} = \frac{\frac{-f(x_{i+2}, y) + 4f(x_{i+1}, y) - 3f(x_i, y))}{2h} + O(h^2)}{\frac{-g(x_{i+2}, y) + 4g(x_{i+1}, y) - 3g(x_i, y))}{2h} + O(h^2)}$$

(22)

2.2.3. BFD, HABFD, indeterminate limit formulations based on BFD and HABFD

By use of (7), first derivative by BFD based on $O(h)$ can be obtained as (Chapra and Canale, 2010)

$$f'(x_i, y) = \frac{f(x_i, y) - f(x_{i-1}, y)}{h} + O(h)$$

(23)

By use of both (3) and (23), final form of the proposed BFD technique with combination of L'Hopital rule can be found for solution of indeterminate limit. It is given as

$$\lim_{(x,y) \rightarrow (x^*, y^*)} \frac{f(x,y)}{g(x,y)} = \frac{\frac{f(x^*_i, y) - f(x^*_{i-1}, y)}{h} + O(h)}{\frac{g(x^*_i, y) - g(x^*_{i-1}, y)}{h} + O(h)} \quad (24)$$

By substituting first order derivative in (23) into (7), BFD representation of the second order derivative based on error $O(h^2)$ can be obtained as

$$f''(x_i, y) = \frac{f(x_i, y) - 2f(x_{i-1}, y) + f(x_{i-2}, y)}{h^2} \quad (25)$$

Third order derivative based on error $O(h^2)$ by BFD computation:

$$f^{(3)}(x_i, y) = \frac{f(x_i, y) - 3f(x_{i-1}, y) + 3f(x_{i-2}, y) - f(x_{i-3}, y)}{h^3} \quad (26)$$

To find the high-accurate form of first derivative by BFD based on error $O(h^2)$, one should use both (25) and (26), and substitute them into (7). So accurate form of BFD becomes

$$f'(x_i, y) = \frac{3f(x_i, y) - 4f(x_{i-1}, y) + f(x_{i-2}, y)}{2h} + O(h^2) \quad (27)$$

To get the final form of L'Hopital rule transition to HABFD (27) should be substituted into (3). The following formulation can be obtained:

$$\lim_{(x,y) \rightarrow (x^*, y^*)} \frac{f(x,y)}{g(x,y)} = \frac{\frac{3f(x^*_i, y) - 4f(x^*_{i-1}, y) + f(x^*_{i-2}, y)}{2h} + O(h^2)}{\frac{3g(x^*_i, y) - 4g(x^*_{i-1}, y) + g(x^*_{i-2}, y)}{2h} + O(h^2)} \quad (28)$$

2.2.4. Richardson extrapolation based on CFD and HACFD, indeterminate limit formulations

To improve CFD and HACFD results, Richardson Extrapolation can be employed, conveniently. Target is to get more accurate results. For this reason, following steps are performed (Chapra and Canale, 2010):

$$C \cong C(h_2) + \frac{1}{\left(\left(\frac{h_1}{h_2}\right)^2 - 1\right)} (C(h_2) - C(h_1)) \quad (29)$$

where $h_2 = \frac{h_1}{2}$, by rearranging (29), final form of Richardson extrapolation can be found. It is

$$C \cong \frac{4}{3} C(h_2) - \frac{1}{3} C(h_1) \quad (30)$$

$C(h_2)$ and $C(h_1)$ can be obtained from the (10) for CFD based computation. If one can prefer computations based on HACFD, then $C(h_2)$ and $C(h_1)$ can be obtained from the (15) for HACFD based computation. Final form of transition from L'Hopital rule to new proposed method based on CFD with use of (3) and (10), one can obtain

$$\lim_{(x,y) \rightarrow (x^*, y^*)} \frac{f(x,y)}{g(x,y)} = \frac{\frac{4}{3}C1(h_2) - \frac{1}{3}C1(h_1) + O(h^2)}{\frac{4}{3}C2(h_2) - \frac{1}{3}C2(h_1) + O(h^2)} \quad (31)$$

where C1 is CFD based results for function $f(x, y)$ and C2 is CFD based results for function $g(x, y)$.

For CFD approximations, $O(h^2)$ yield a new estimate of new accuracy $O(h^4)$.

Final form of transition from L'Hopital rule to new proposed method based on HACFD with employ of (3) and (15), one can found the following formulation:

$$\lim_{(x,y) \rightarrow (x^*, y^*)} \frac{f(x,y)}{g(x,y)} = \frac{\frac{4}{3}C11(h_2) - \frac{1}{3}C11(h_1) + O(h^4)}{\frac{4}{3}C22(h_2) - \frac{1}{3}C22(h_1) + O(h^4)} \quad (32)$$

where C11 is HACFD based results for function $f(x, y)$ and C22 is HACFD based results for function $g(x, y)$. For HACFD approximations, $O(h^4)$ yield a new estimate of new accuracy $O(h^6)$.

2.2.5. Richardson extrapolation based on FFD and HAFFD, indeterminate limit formulations

To enhance FFD and HAFFD results and get more accurate results, Richardson Extrapolation can be employed. The steps are similar to those for CFD and HACFD based computations.

$$F \cong F(h_2) + \frac{1}{\left(\left(\frac{h_1}{h_2}\right)^2 - 1\right)} (F(h_2) - F(h_1)) \quad (33)$$

where $h_2 = \frac{h_1}{2}$, by rewriting (33), final form of Richardson extrapolation can be obtained which is

$$F \cong \frac{4}{3}F(h_2) - \frac{1}{3}F(h_1) \quad (34)$$

$F(h_2)$ and $F(h_1)$ can be computed from the (17) for FFD based computation. If one can choose computations based on HAFFD, then $F(h_2)$ and $F(h_1)$ can be obtained from the (21) for HAFFD based computation. Final form of transition from L'Hopital rule to new proposed method based on FFD with use of (3) and (17), one can obtain

$$\lim_{(x,y) \rightarrow (x^*, y^*)} \frac{f(x,y)}{g(x,y)} = \frac{\frac{4}{3}F1(h_2) - \frac{1}{3}F1(h_1) + O(h)}{\frac{4}{3}F2(h_2) - \frac{1}{3}F2(h_1) + O(h)} \quad (35)$$

Where F1 is FFD based results for function $f(x, y)$ and F2 is FFD based results for function $g(x, y)$.

For FFD approximations, $O(h)$ yield a new estimate of new accuracy $O(h^2)$.

Final form of transition from L'Hopital rule to new proposed method based on HACFD with employ of (3) and (21), one can obtain the following formulation:

$$\lim_{(x,y) \rightarrow (x^*, y^*)} \frac{f(x,y)}{g(x,y)} = \frac{\frac{4}{3}F11(h_2) - \frac{1}{3}F11(h_1) + O(h^2)}{\frac{4}{3}F22(h_2) - \frac{1}{3}F22(h_1) + O(h^2)} \quad (36)$$

Where F11 is HAFFD based results for function $f(x, y)$ and F22 is HAFFD based results for function $g(x, y)$. For HAFFD approximations, $O(h^2)$ yield a new estimate of new accuracy $O(h^4)$.

2.2.6. Richardson extrapolation based on BFD and HABFD, indeterminate limit formulations

To upgrade BFD and HABFD results, Richardson extrapolation can be used, conveniently. Main aim is to get more accurate results. For this reason, following steps are executed (Chapra and Canale, 2010):

$$B \cong B(h_2) + \frac{1}{\left(\left(\frac{h_1}{h_2}\right)^2 - 1\right)} (B(h_2) - B(h_1)) \quad (37)$$

where $h_2 = \frac{h_1}{2}$, by rearranging (37), final form of Richardson extrapolation can be obtained as

$$B \cong \frac{4}{3}B(h_2) - \frac{1}{3}B(h_1) \quad (38)$$

$B(h_2)$ and $B(h_1)$ can be obtained from the (23) for BFD based computation. If one can prefer computations based on HABFD, then $B(h_2)$ and $B(h_1)$ can be obtained from the (27) for HABFD based computation. Final form of transition from L'Hopital rule to new proposed method based on BFD with use of (3) and (23), one can get

$$\lim_{(x,y) \rightarrow (x^*, y^*)} \frac{f(x,y)}{g(x,y)} = \frac{\frac{4}{3}B1(h_2) - \frac{1}{3}B1(h_1) + O(h)}{\frac{4}{3}B2(h_2) - \frac{1}{3}B2(h_1) + O(h)} \quad (39)$$

where B1 is BFD based results for function $f(x, y)$ and B2 is BFD based results for function $g(x, y)$.

For BFD approximations, $O(h)$ yield a new estimate of new accuracy $O(h^2)$.

Final form of transition from L'Hopital rule to new proposed method based on HABFD with employ of (3) and (27), one can found the following formulation:

$$\lim_{(x,y) \rightarrow (x^*, y^*)} \frac{f(x,y)}{g(x,y)} = \frac{\frac{4}{3}B11(h_2) - \frac{1}{3}B11(h_1) + O(h^2)}{\frac{4}{3}B22(h_2) - \frac{1}{3}B22(h_1) + O(h^2)} \quad (40)$$

where B11 is HABFD based results for function $f(x, y)$ and B22 is HABFD based results for function $g(x, y)$. For HABFD approximations, $O(h^2)$ yield a new estimate of new accuracy $O(h^4)$.

3. Error Analysis

The condition and stability analysis of a problem relates to its sensitivity to changes in its input values. It is clear that a computation is numerically unstable if the uncertainty of the input values is over exaggerated by the numerical method (Chapra and Canale, 2010). Taylor series for two variables without second order and higher order terms can be written as:

$$f(x_{i+1}, y_{i+1}) = f(x_i, y_i) + f'(x_i, y)(x_{i+1} - x_i) + f'(x, y_i)(y_{i+1} - y_i) + \dots \quad (41)$$

Where estimates of the errors in x is $(x_{i+1} - x_i)$ and y is $(y_{i+1} - y_i)$, respectively. These are assumed to be equal and denoted as h .

Equation (41) can be rearranged as

$$f(x_{i+1}, y_{i+1}) - f(x_i, y_i) = (f'(x_i, y) + f'(x, y_i))h + \dots \quad (42)$$

In (42),

$$f(x_{i+1}, y_{i+1}) - f(x_i, y_i) = \Delta f(\tilde{x}, \tilde{y})$$

For all examples, the function values are equal to 0 to become indeterminate limit condition.

An algorithm is stable if the following equality holds:

$$h = \frac{f(x_{i+1}, y_{i+1}) - f(x_i, y_i)}{(f'(x_i, y) + f'(x, y_i))} \quad (43)$$

If the numerator in (43) converges to 0, the problem becomes stable and well conditioned. This also leads to indeterminate limit form. For this reason, h is selected as very small values closer to 0.

This situation also fits with smaller step size selection in Taylor series.

Dropping the second and higher-order terms and rearranging (42) yields:

$$\Delta f(\tilde{x}, \tilde{y}) = (f'(x_i, y) + f'(x, y_i))h. \quad (44)$$

It is possible to determine bounds for exact solutions of finite difference approaches by use of (44)

$$f(x_{i+1}, y_{i+1}) = f(x_{i+1}, y_{i+1}) \pm (f'(x_i, y) + f'(x, y_i))h \quad (45)$$

Since, $f(x_{i+1}, y_{i+1}) = 0$ to make the limits indeterminate, upper and lower bounds should involve 0. So h should be selected as minimum as possible to involve exact solution for higher accuracy and sensitivity. As a result h should converge to 0. For this reason, $h=10^{-4}$ is selected as tolerance amount for step size choice such that h less than this amount, it is accepted that exact results can be always obtained.

4. Numerical Results and Discussion

Examples for indeterminate limit form: $\frac{0}{0}$ is presented in Table 1. A general code is generated for application of the proposed methods in Matlab R2022a. Numerical results are analyzed in terms of accuracy, error and computational time. These are presented in following subsections, respectively.

Table 1. Examples for indeterminate form: $\frac{0}{0}$

Example	Limit
1	$\lim_{(x,y) \rightarrow (1,-1)} \frac{(x^3+y^3)}{x+y}$
2	$\lim_{(x,y) \rightarrow (1,1)} \frac{(x^2-y^2)}{x-y}$
3	$\lim_{(x,y) \rightarrow (1,1)} \frac{(x^4 - y^4)}{(\ln(x) - \ln(y))}$
4	$\lim_{(x,y) \rightarrow (0,0)} \frac{(x - y)}{(\sin(x) - \sin(y))}$
5	$\lim_{(x,y) \rightarrow (0,0)} \frac{(x - \sin(y))}{(\sin(x) - y)}$
6	$\lim_{(x,y) \rightarrow (1,-1)} \frac{(x + y)}{(x^2 - y^2)}$

4.1. Accuracy

For the examples presented in Table 1, indeterminate limits are computed by each method and displayed in Figures 1-6.

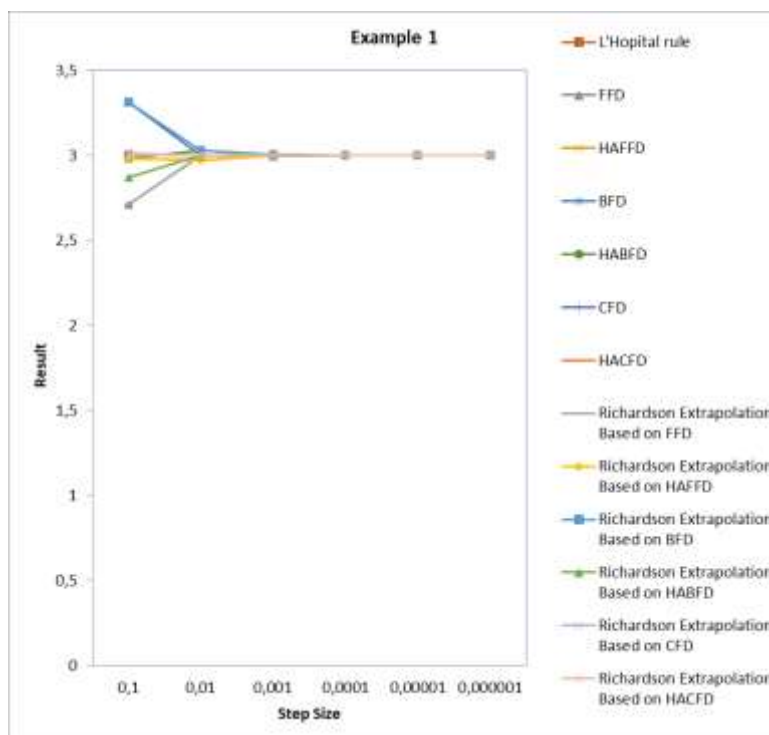


Figure 1. Computation results by all methods for Example 1

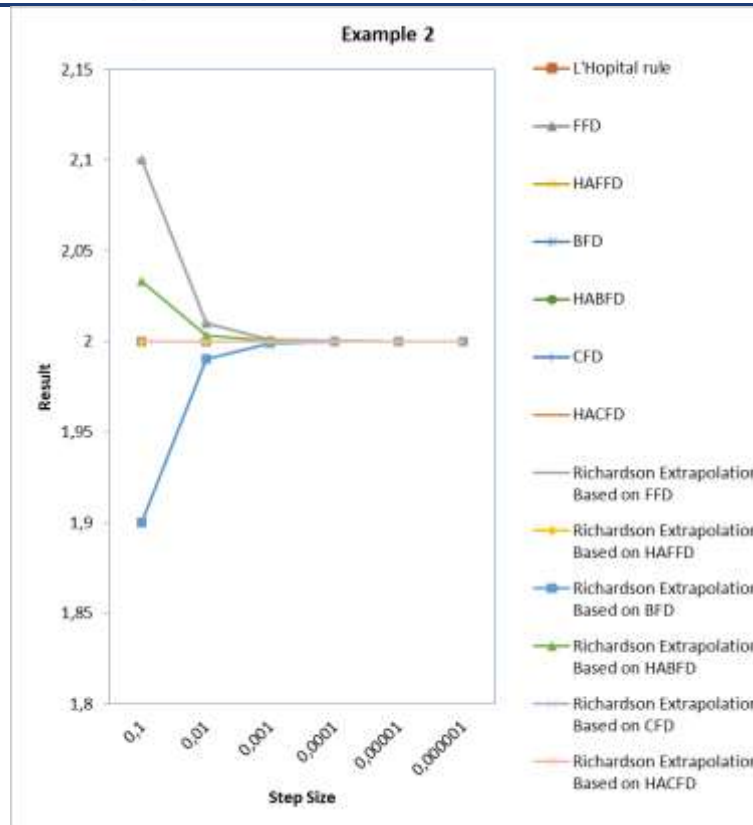


Figure 2. Computation results by all methods for Example 2

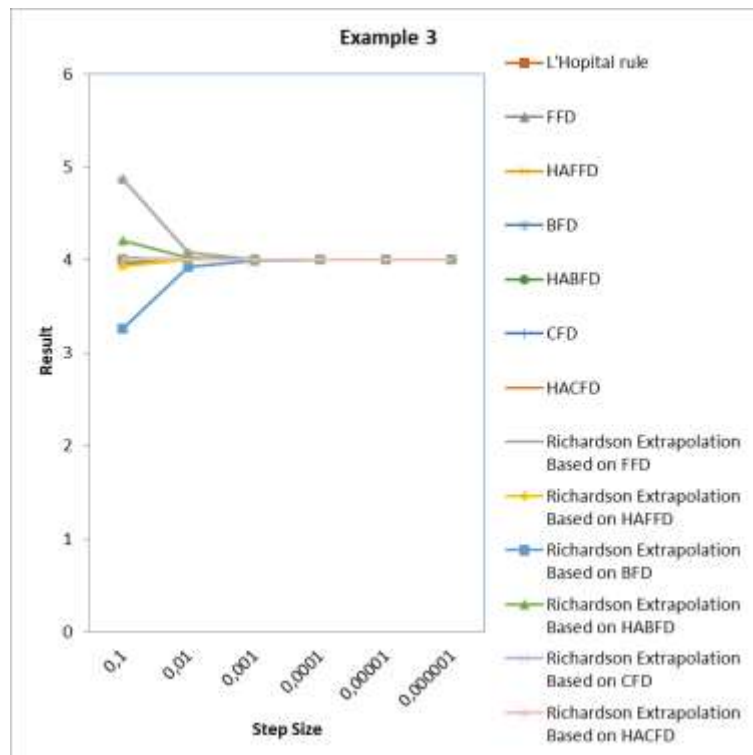


Figure 3. Computation results by all methods for Example 3

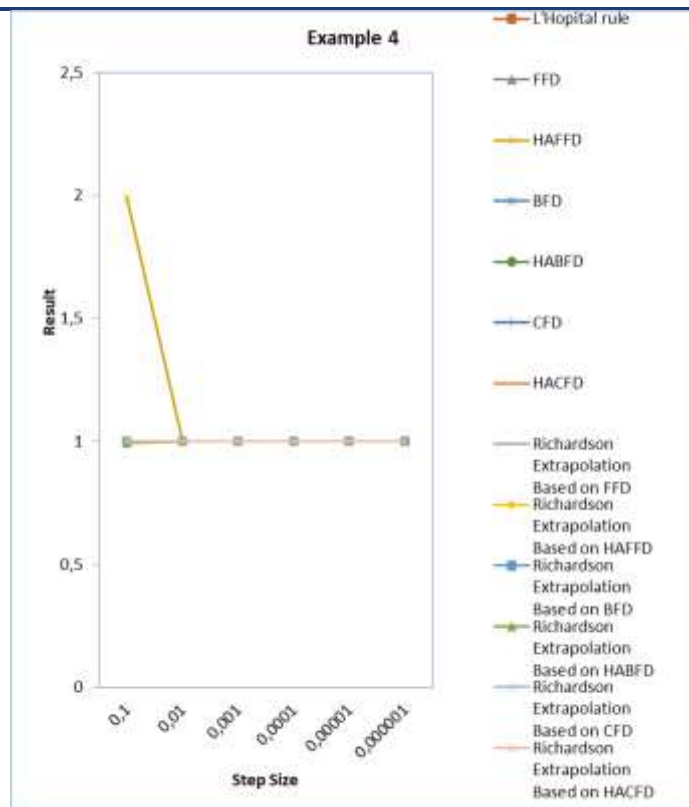


Figure 4. Computation results by all methods for Example 4

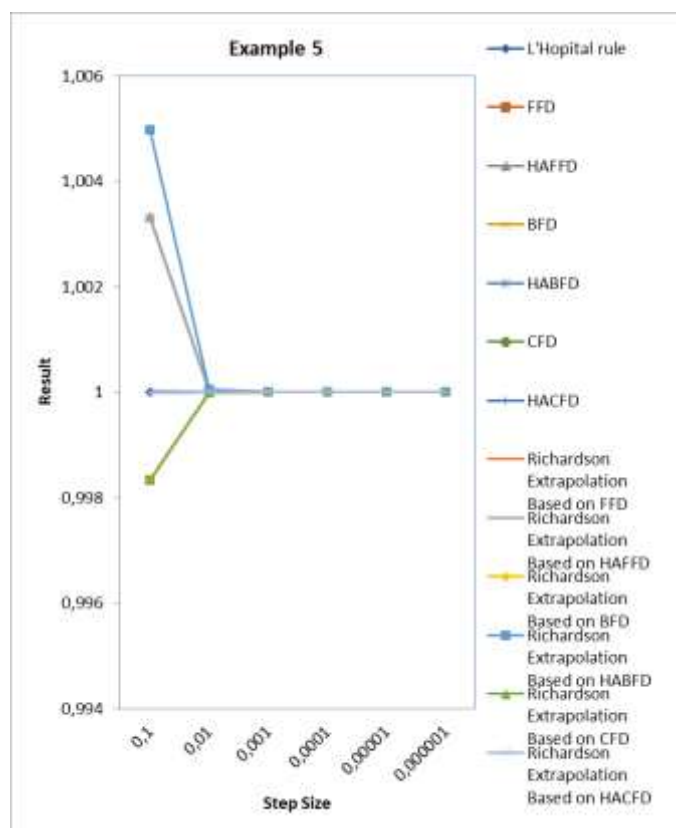


Figure 5. Computation results by all methods for Example 5

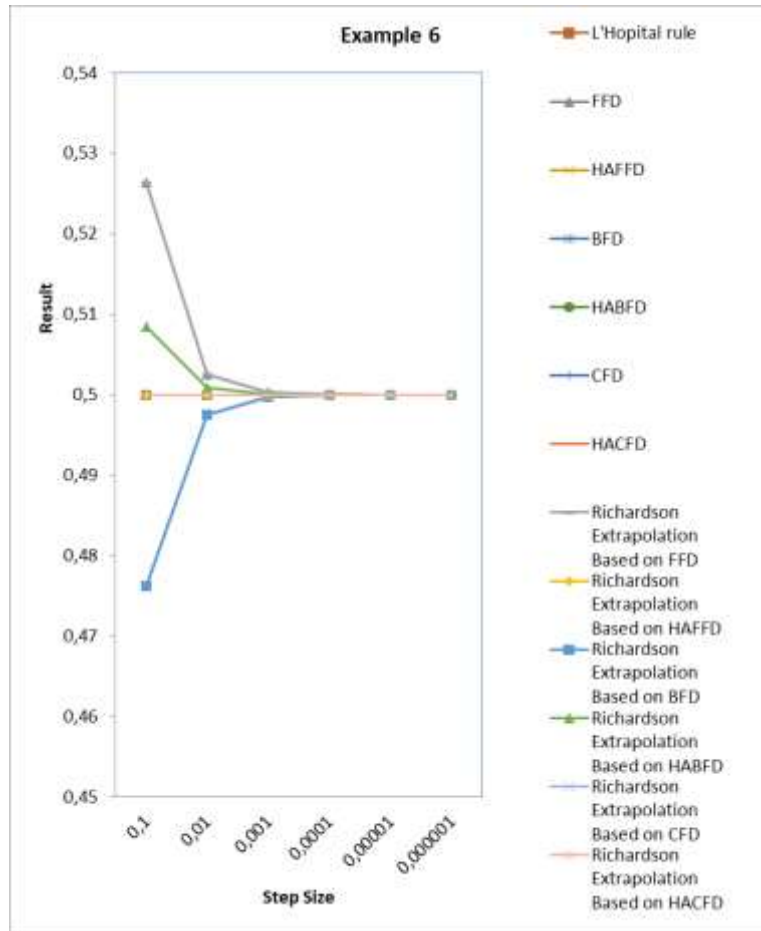


Figure 6. Computation results by all methods for Example 6

In common for Figures 1-6, when step size is 10^{-4} , exact results can be found for all examples in Table 1. For less amount of step size, FFD, BFD, Richardson Extrapolation based on BFD and FFD methods yield results diverge from true values. Notwithstanding, L'Hôpital rule HACFD, Richardson Extrapolation based on HABFD, HACFD and HAFD converge to exact results fastly, even if step size is 10^{-1} .

4.2. Error

Error is computed in terms of true percent relative error. It is given as

$$\text{Error} = \left| \frac{\text{True Value} - \text{Approximation}}{\text{True Value}} \right| \times 100 \quad (46)$$

By using the formula in (46), amount of error for each example in Table 1 can be computed. The results for each example are displayed in Figures 7-12, respectively.

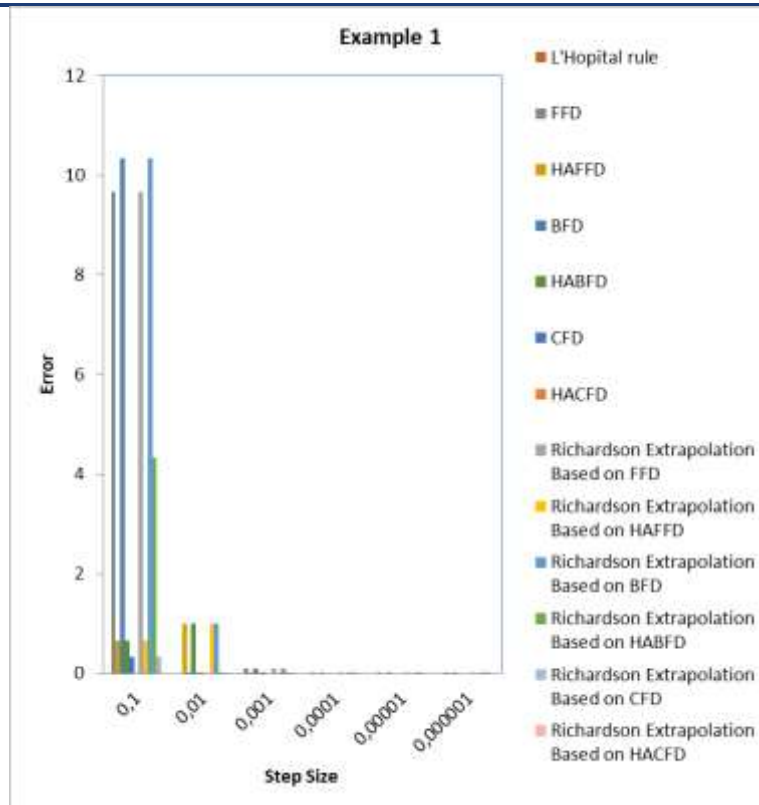


Figure 7. Error computation for Example 1

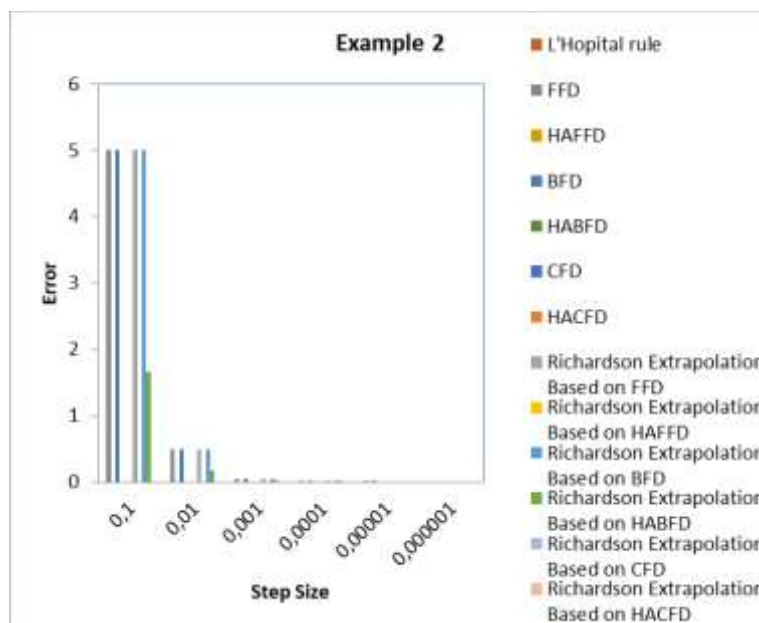


Figure 8. Error computation for Example 2

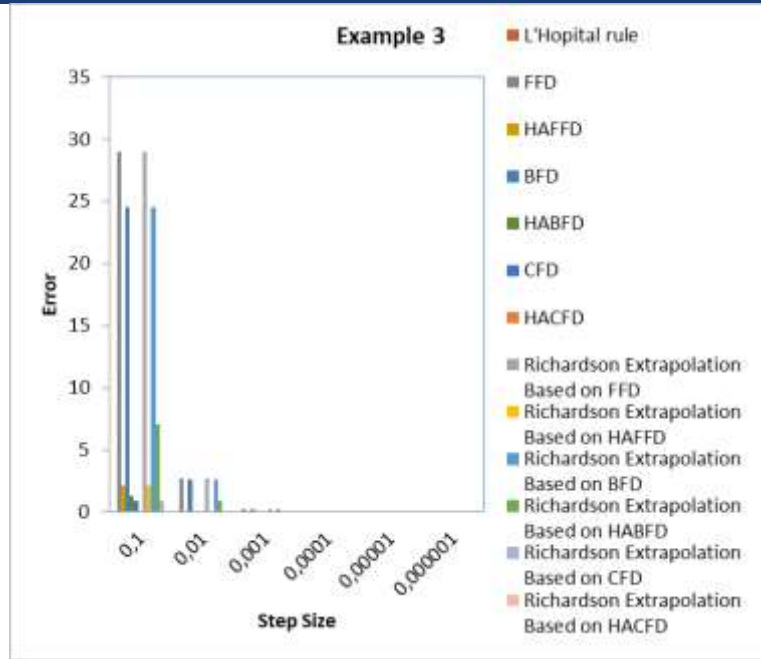


Figure 9. Error computation for Example 3

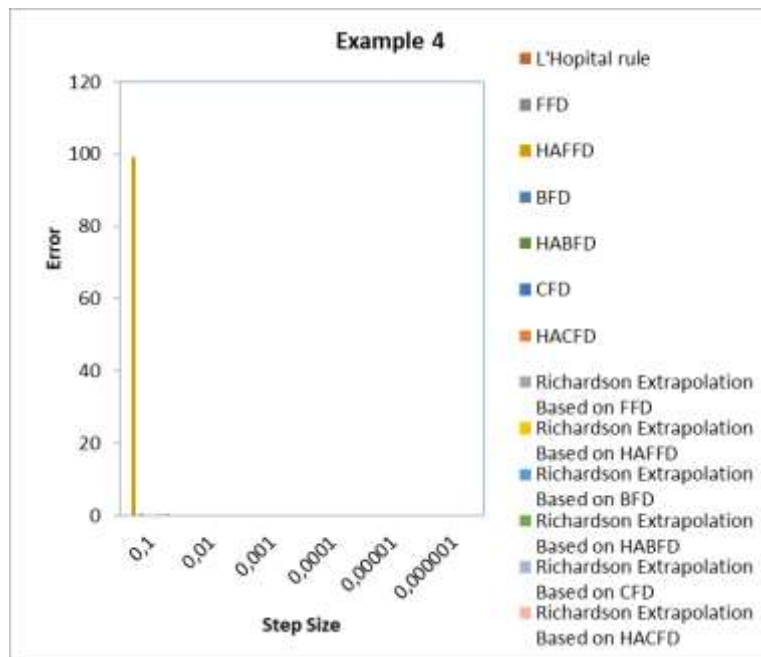


Figure 10. Error computation for Example 4

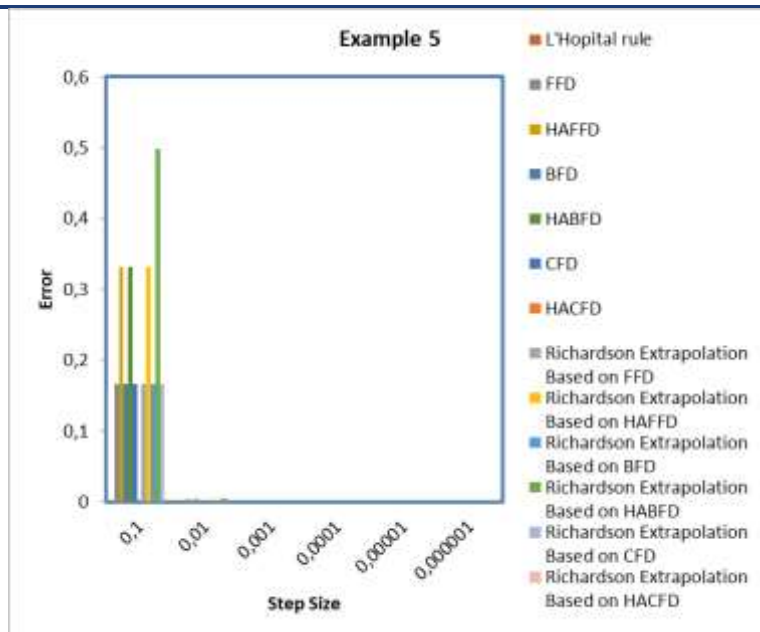


Figure 11. Error computation for Example 5

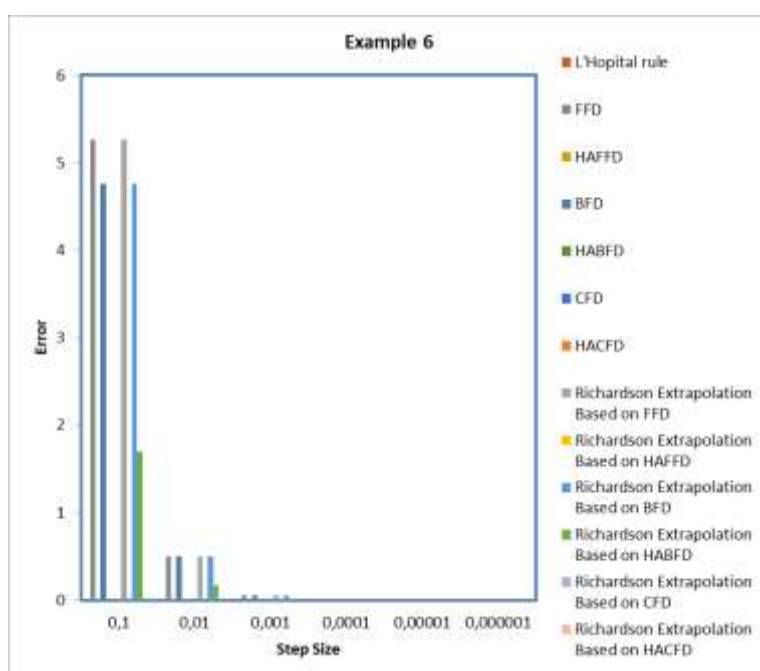


Figure 12. Error computation for Example 6

It is obvious that error is 0 when step size is 10^{-4} for all methods in Figures 7-12. Nevertheless, for h values less than 10^{-4} , there exists error amounts, especially for methods; BFD, FFD, Richardson extrapolation based on BFD and FFD.

4.3. Computational time

For the performance of the algorithm, computational time is measured with use of all numerical methods as well as L'Hôpital rule. The results are presented in Figures 13-18 for each example.

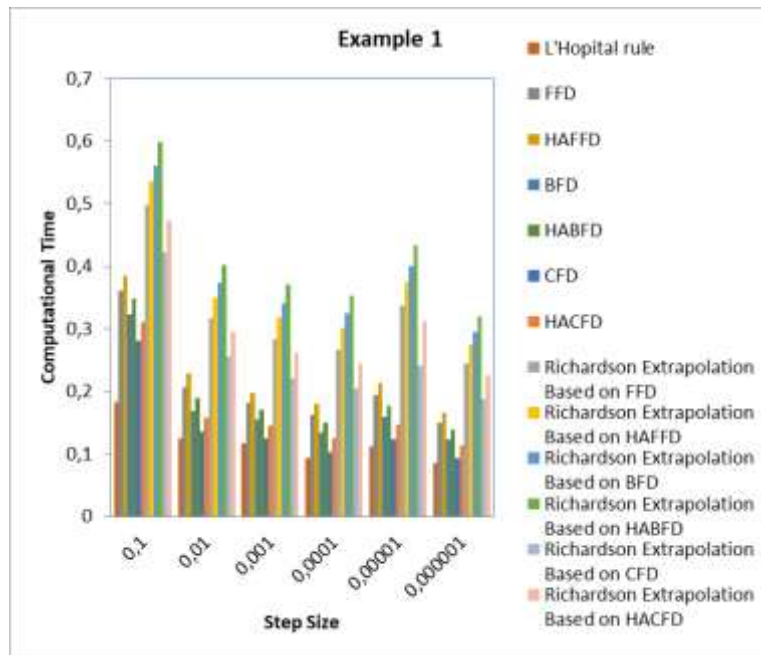


Figure 13. Computational time for Example 1

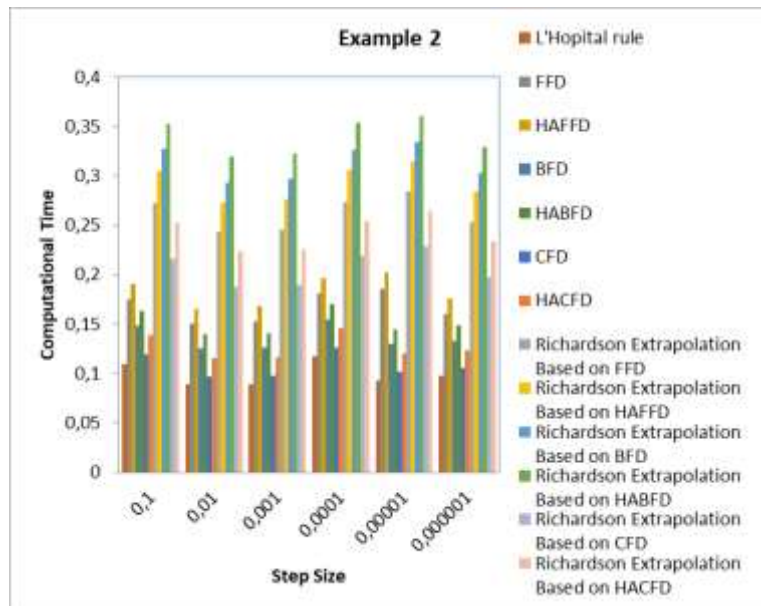


Figure 14. Computational time for Example 2

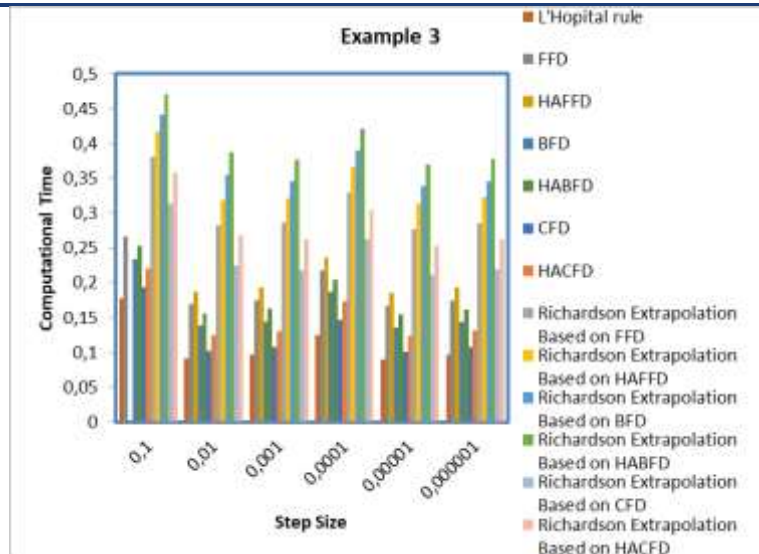


Figure 15. Computational time for Example 3

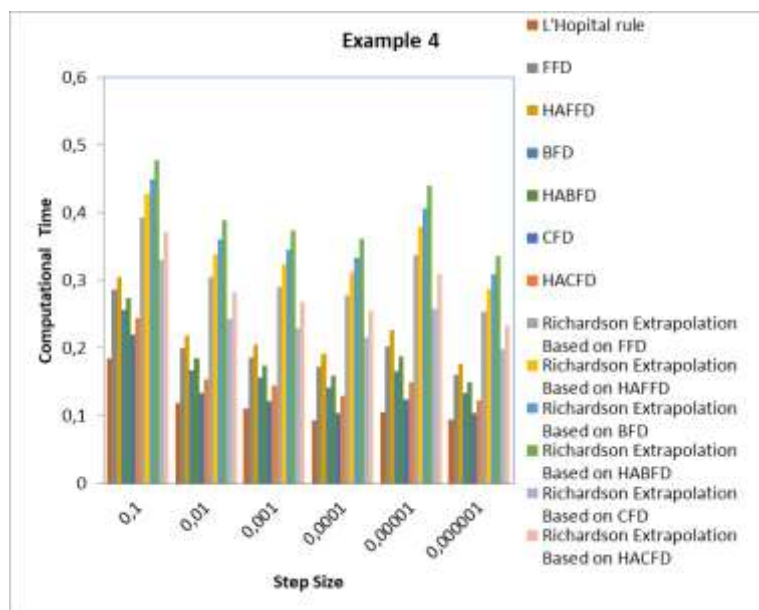


Figure 16. Computational time for Example 4

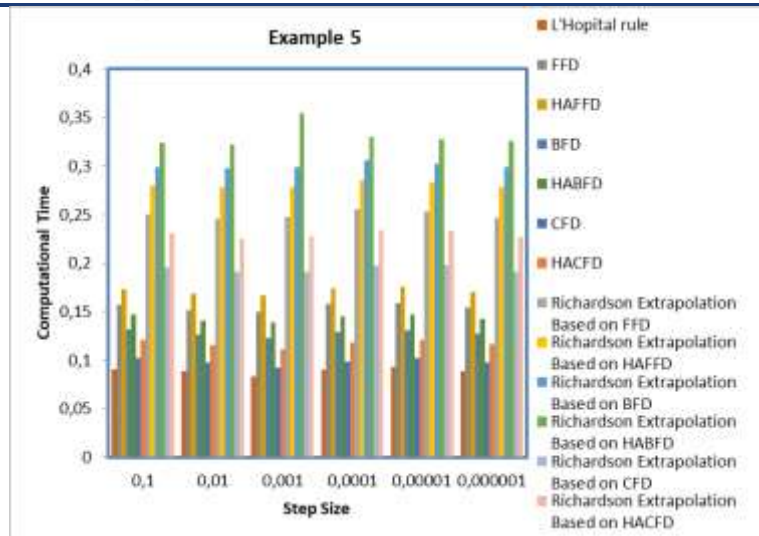


Figure 17. Computational time for Example 5

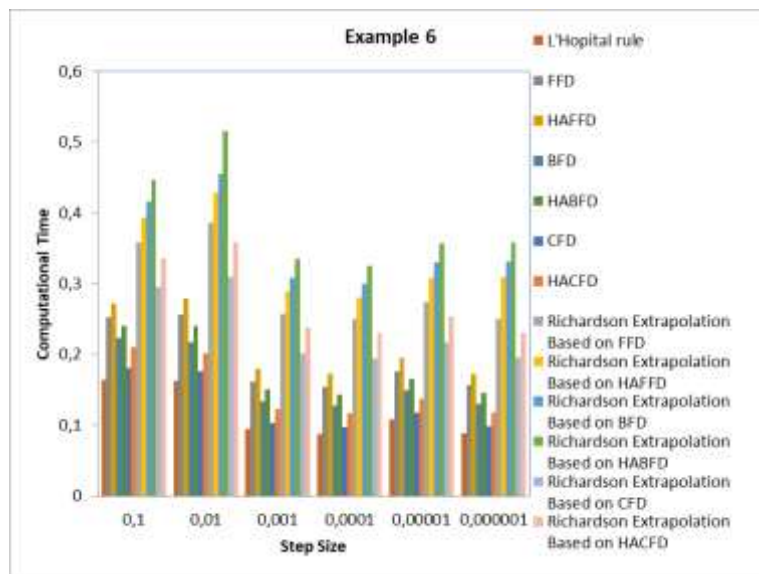


Figure 18. Computational time for Example 6

For each example, less amount of step size leads to a decrease in computational time for all methods. L' Hôpital rule spends the least amount of time while Richardson Extrapolation method based on HABFD spends the most computational time for each example. These situations are proved in Figures 13-18.

Furthermore, examples and numerical results for other indeterminate forms of small functions with isolated and non isolated singularities are also illustrated in Table 2.

Table 2. Numerical results for other indeterminate forms of small functions

Example	FFD	HAFFD	BFD	HABFD	Richardson Extrapolation Based on FFD	Richardson Extrapolation Based on HAFFD	Richardson Extrapolation Based on BFD	Richardson Extrapolation Based on HABFD
$\lim_{(x,y) \rightarrow (0,0)} \frac{x^\alpha y}{x^6 + x^2 y^2 + y^6}$ $0 \leq \alpha \leq 7$	0	0	0	0	0	0	0	0
$\lim_{(x,y) \rightarrow (0,0)} \frac{(x^2 - y^2)^2}{x^4 + 2(\sin(x))^2(\sin(y))^2 + y^4}$	1	1	1	1	1	1	1	1
$\lim_{(x,y) \rightarrow (0,0)} \frac{x^\alpha y}{x^4 + y \sin(y)}$ $0 \leq \alpha \leq 4$	0	0	0	0	0	0	0	0

According to Table 2; L' Hôpital rule, CFD, HACFD, Richardson Extrapolation based on CFD and HACFD methods are inapplicable for indeterminate limit form: $\frac{0}{0}$. Even so, FFD, HAFFD, BFD, HABFD, Richardson Extrapolation based on FFD, HAFFD, BFD, HABFD techniques can be used conveniently for all step sizes ($h \leq 0.1$). These methods give the same exact result. Computational time is in the interval such that at minimum: 0.0156 seconds and maximum: 0.1200 for the examples in Table 2.

Moreover, the effect of decreasing step size significantly causes accuracy for all methods proposed. This situation is proved by Figures 1-12.

5. Conclusion

This paper presents alternative methods with use of CFD, BFD, FFD, HACFD, HABFD, HAFFD, Richardson Extrapolation methods based on BFD, FFD, HACFD, HABFD and HAFFD for: $0/0$ of two variable functions with isolated and also non isolated singularities. So, there is no need to use L' Hôpital rule with taking partial derivatives. Two variable functions are selected according to the difficulty and not applicability of L' Hôpital rule. Numerical results for some two variable functions are given for proof of the purpose of this study. It is the first time in the literature that numerical differentiation techniques are employed for indeterminate limits of two variable functions. L'Hôpital rule is impractical and complicated for evaluations of limits for some functions.

It is also shown that FFD, HAFFD, BFD, HABFD, Richardson Extrapolation methods based on BFD, FFD, HABFD and HAFFD can be applied to: $0/0$ of both functions of two variables with isolated and non isolated singularities. According to error tolerance, step size selection should be at least 10^{-4} .

As one of the future works; functions with more than two variables can be employed for indeterminate limit computations. These methods can be applied to these cases. This leads to additional computational effort. For these reasons, new algorithms can be designed to simplify computations. Other future work is to employ adaptive step size such that step size can be adjusted according to error computation for each iteration with use of same methods. This situation can also be adapted to functions with more than two variables.

Other indeterminate limit forms such as: $\frac{\infty}{\infty}$, $0 \cdot \infty$ can be considered. All these numerical differentiation methods can be applied to these forms.

As potential real-world applications, the proposed methods in this paper can be used conveniently by instructors and students in calculus courses for all multivariable functions with also both isolated and non isolated singularities. So these methods can be covered in lecture books and notes as a chapter in calculus lectures. New algorithms can be designed also simplify the computation overload and minimize the computation cost and time. These algorithms can also be an additional topic to be covered in calculus lectures and recitations. Beside well-known methods, these methods proposed in this study will be a good contribution to calculus lectures.

Ethics Permissions

There is no need for ethics committee permission in this study.

Conflict of Interest

There is no conflict of interest.

References

- Aczél, J. (1990). Functional equations and L'Hôpital's rule in an exact Poisson derivation. *American Mathematical Monthly*, 97(5), 423–426.
- Chapra, S. C., and Canale R. P. (2010). *Numerical Methods for Engineers*, Sixth Edition, Mc Graw Hill, New York.
- Cooke, W. P. (1988). The Teaching of Mathematics: L'Hopital's Rule in a Poisson Derivation. *American Mathematical Monthly*, 95(3), 253–254.
- Corona-Corona, G. (2018). About the Proof of the L'Hôpital's Rule. *American Scientific Research Journal for Engineering, Technology, and Sciences (ASRJETS)*, 41(1), 240-245.
- Dinçkal, Ç. (2024). Additional chapter for evaluation indeterminate limits of functions and series in teaching mathematics for engineering education. *International Journal of Engineering, Science and Technology*, 16(4), 20-28.
- Durán, A. L. (1992). The converse of de L'Hôpital's rule. *Ciencia e Tecnica*, 16, 111-119.
- Estrada, R., and Pavlović, M. (2017). L'Hôpital's monotone rule, Gromov's theorem, and operations that preserve the monotonicity of quotients. *Publications de l'Institut Mathématique*, 101(115), 11-24.
- Fine, A. I., and Kass, S. (1966). Indeterminate forms for multi-place functions. *Annales Polonici Mathematici*, 1(18), 59-64.
- Gordon, S. P. (2017). Visualizing and understanding L'hospital's rule. *International Journal of Mathematical Education in Science and Technology*, 48(7), 1096-1105.
- Hartig, D. (1991). L'Hôpital's rule via integration American. *Mathematical Monthly*, 98(2), 156–157.
- Huang, X. C. (1988). A discrete L' Hôpital's rule. *College Mathematics Journal*, 19(4), 321–329. <https://doi.org/10.1080/07468342.1988.11973132>
- Ivlev, V. V. (2013). Mathematical analysis: Multivariable functions, Moskow, IKAR in Russian.
- Ivlev V. V., Shilin, I. A. (2014). On generalization of L'Hôpital's rule for multivariable functions, arXiv: 1403.3006v1.
- Lawlor, G. R. (2020). L'Hôpital's rule for multivariable functions. *American Mathematical Monthly*, 127(8), 717-725 <https://doi.org/10.1080/00029890.2020.1793635>.
- Muntean, L. (1993). *L'Hôpital's rules with extreme limits*, Seminar on Mathematical Analysis (Cluj-Napoca, 1992–1993), Babe-Bolyai Univ., Cluj-Napoca 11–28, Preprint: 93-7
- Popa, D. (1999). On the vector form of the Lagrange formula, the Darboux property and l'Hôpital's rule, *Real Analysis Exchange*. 25(2): 787-794
- Shishkina, A. V. (2007). On the inversion of the L'Hôpital rule for functions holomorphic in the ball. (Russian), *Izvestiya Vyssh. Uchebn. Zaved. Mat.* 2006, no. 6, 78-84; translation in *Russian Mathematics* (Iz. VUZ), 50(6): 76–82.
- Spigler, R., and Vianello, M. (1993). Abstract Versions of L' Hôpital' s Rule for Holomorphic Functions in the Framework of Complex B-Modules. *Journal of Mathematical Analysis and Applications*, 180(1), 17-28.
- Szabó, G. (1989). A note on the L'Hôpital's rule. *Elemente der Mathematik*, 44, 150–153.
- Takeuchi, Y. (1995). L'Hôpital's rule for series. *Bol. Mat.*, 1/2. 2(1), 17-33.
- Tian, Y. X. (1993). L'Hôpital rules for conjugate analytic functions. *Sichuan Shifan Daxue Xuebao Ziran Kexue Ban*, 16, 53-56.
- Vianello, M. (1992). A generalization of l'Hôpital's rule via absolute continuity and Banach modules. *Real Analysis Exchange*, 18(2), 1992/93, 557-56
- Vyborny, R., and Nester, R. (1989). L'Hôpital's rule, a counterexample. *Elemente der Mathematik*, 44, 116-121.
- Young, W. H. (1910). On indeterminate forms. *Proceedings of the London Mathematical Society*, 2(1), 40-76.
- Zlobec, S. (2012). L'Hôpital's rule without derivatives. *Mathematical Communications*, 17(2), 665-672.

Wear Behaviour of Non-Heat Treated, Hardened and PVD Coated Steel Cams

Ersin ARSLANBULUT^{1*}, Burhan SELÇUK²

Keywords

Wear,
Camshaft,
PVD coating


Abstract – In this experimental study, the wear behaviour of AISI 1050 steel camshaft cams subjected to different surface treatments was systematically investigated. The cam samples were divided into three distinct groups: non-heat treated, induction hardened, and CrN coated using the physical vapor deposition (PVD) method. The aim was to evaluate and compare the tribological performance of each treatment type under dry sliding conditions. As the counterface material, HS10.4-3-10 high-speed steel, commercially known as lathe tool steel, was selected due to its high hardness and abrasion resistance, making it suitable for simulating real-life contact conditions. Wear tests were carried out using a cam profile measuring device adapted as a wear tester. Each cam sample was subjected to abrasion for a total duration of three hours under varying test conditions, specifically under three different normal loads (4 N, 8 N, and 12 N) and three different rotational speeds (85 rpm, 100 rpm, and 115 rpm). This setup resulted in nine test configurations per sample group. During the tests, the weight loss of the samples was recorded at one-hour intervals using a high-precision analytical balance. The experimental results revealed that the CrN-coated samples exhibited the lowest amount of wear, demonstrating the effectiveness of the PVD coating in enhancing surface durability under dry friction conditions.

1. Introduction


Cam mechanisms are basic machine elements that convert rotary motion into linear or oscillatory motion depending on a specific timing. These mechanisms have a wide range of uses, especially in internal combustion engines, automation systems, and industrial applications requiring high precision (Litvin and Fuentes, 2004). The main function of cams is to ensure that the controlled motion is transmitted repeatedly, stably and efficiently. However, cam parts operating under difficult tribological conditions such as high surface pressure, sudden load changes and continuous contact encounter serious wear problems over time (Dowson, 1998; Hutchings and Shipway, 2017).

Wear is defined as the material loss that occurs during the relative movement of material surfaces with respect to each other, and this process depends on many parameters such as surface roughness, hardness, microstructure, temperature, load, speed and environmental conditions (Stachowiak and Batchelor, 2005). Especially in systems with inadequate lubrication conditions, adhesion, abrasion and surface fatigue wear mechanisms are among the main causes of wear (Bhushan, 2013; Jahanmir and Beltz, 2000). This situation is a critical problem that affects not only the efficiency of the mechanism but also the maintenance frequency and the overall life of the system.

The durability and wear resistance of cam mechanisms largely depend on the type of steels used in their manufacture and the microstructural properties of these steels. Cams are usually manufactured from low alloy carbon or medium alloy structural steels because these materials offer suitable mechanical properties in terms of both hardenability and impact resistance (Totten and Howes, 1997). For example, steels such as 42CrMo4 and 16MnCr5 are widely preferred in cam manufacturing due to their suitability for both heat treatment and surface

^{1*}**Corresponding Author.** Sivas Cumhuriyet University, Sivas Vocational School of Technical Sciences, Department of Machinery and Metal Technologies, 58140 Sivas, Türkiye. E-mail: arslanbulut@cumhuriyet.edu.tr  ORCID: 0000-0002-0607-6159

²Sivas Cumhuriyet University, Engineering Faculty, Department of Mechanical Engineering, 58140 Sivas, Türkiye. E-mail: selcuk@cumhuriyet.edu.tr

 ORCID: 0000-0001-5617-8674

Citation: Arslanbulut, E., and Selcuk, B. (2025). Wear behaviour of non-heat treated, hardened and PVD coated steel cams. *Natural Sciences and Engineering Bulletin*, 2(1), 75-82.

hardening processes (ASM International, 1990). However, since the surface properties of these steels directly determine the wear performance, surface engineering applications are of great importance in preventing wear.

Surface treatments applied to reduce wear have been developed to increase surface hardness, reduce the coefficient of friction and keep surface roughness under control. Wear-resistant hard phases are formed on steel surfaces with surface hardening methods (e.g. plasma nitriding, induction hardening, cementation) (Vöhringer, 2001). In addition, with modern coating technologies such as physical vapor deposition (PVD), thin film coatings such as TiN, CrN, TiAlN and DLC with high hardness are applied to cam surfaces and improve tribological performance in both dry and oily conditions (Holmberg and Matthews, 2009; Podgornik et al., 2004).

The compatibility of PVD coatings, especially with steel substrates, enables the combination of hard coating and toughness, minimizing negativities such as microcracking and delamination (Zhang et al., 2011). The effects of surface modifications on microstructure, hardness profile and wear morphology have also been confirmed by experimental studies (Gharbi et al., 2015).

In this study, the wear behaviours of cam samples obtained from AISI 1050 manufacturing steel improved by surface hardening and PVD coating processes were comparatively investigated with the dry friction block-on-ring method. The obtained results are aimed to contribute to academic literature.

2. Materials and Method

Reducing the wear of machine components and minimizing the resulting economic losses have long been among the primary goals of engineers working in the field of tribology. Wear not only leads to material degradation but also incurs significant financial costs associated with the repair, maintenance, or replacement of damaged equipment. These cumulative effects represent a considerable burden on the global economy. While conducting wear experiments under actual operating conditions would provide the most accurate and relevant results, replicating such conditions in a laboratory environment is often technically challenging and resource-intensive. Therefore, it becomes essential to investigate the wear behaviour of commonly used machine parts, such as camshafts, through controlled experimental setups. Such studies can provide valuable insights into the mechanisms of wear and offer guidance for the development of more durable materials and surface treatments.

2.1. Selection of Materials

AISI 1050 steel was used as the cam sample material. HS 10.4-3-10 high speed steel, known as lathe tool in the market, was used as the abrasive counter element. The chemical structures and mechanical properties of these two materials are given in Table 1. The values of the cam material were taken from the manufacturer company that produces the camshaft.

Table 1. Chemical structures and mechanical properties of the cam material and the counter abrasive element

Materials	Chemical composition									Mechanical properties			
	C	Si	Mn	Cr	Cu	Mo	V	W	Co	σ_{φ}	σ_a	E	Hard.
	%	%	%	%	%	%	%	%	%	(MPa)	(MPa)	(MPa)	HV
AISI1050	0.5	0.3	0.75	-	-	-	-	-	-	650	360	190	240
HS10.4-3-10	1.28	0.45	0.4	4.15	-	3.9	3.25	9.5	10	617	445	630	950

2.2. Preparation of Samples

The samples were prepared by Estaş company, a camshaft manufacturer, according to the dimensions given in Figure 1. After the shafts were manufactured, their cams were cut and holes were drilled in their centers to make them suitable for the wear test bench. Their surface qualities are close to each other. The average surface roughness of the samples, which are 27 in total, is $R_a = 0.3 \mu\text{m}$ and their surface hardness is around 240 HV.

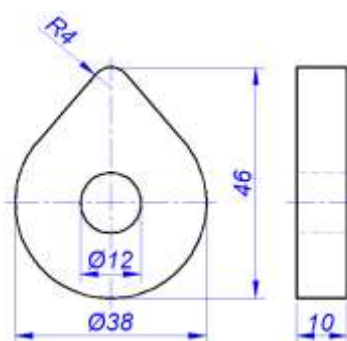


Figure 1. Shape and dimensions of the cam sample

2.3. Heat treatment

The total number of samples is 27. 18 of them were induction hardened. This process, with hardening parameters of 3 s at 870 °C, was carried out at Estaş, the company that produces the cams. 9 of the 18 hardened samples were coated with PVD-CrN. This process was carried out at 400°C; a hardness of over 2000HV was achieved. Figure 2 shows that the thickness of the PVD coating is over 7 µm.

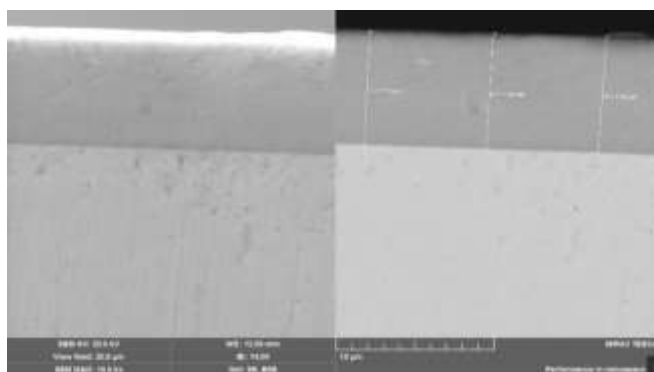


Figure 2. SEM image of the PVD coating

Microstructure images were taken with an optical microscope at Sivas Cumhuriyet University, Mechanical Engineering Laboratory. Figure 3 shows the optical microscope images of the hardened and PVD coated samples.

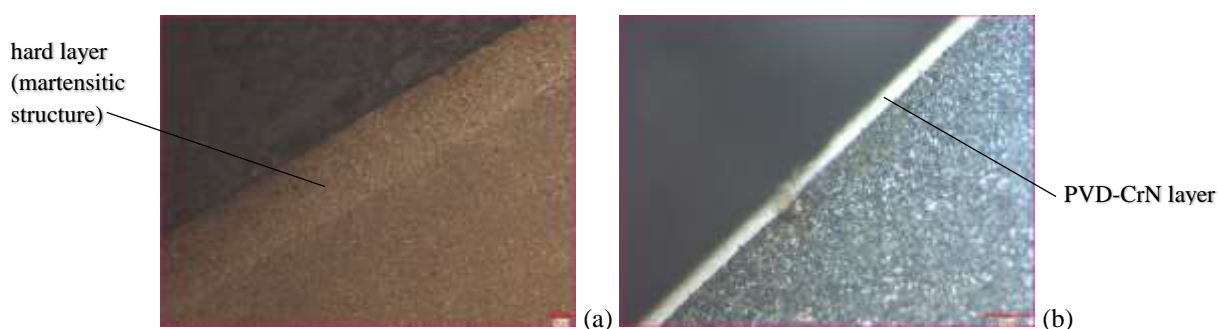


Figure 3. Optical microscope microstructure images a) induction hardened sample (100x) b) PVD coated sample (500x)

Three types of samples were used: non-heat treated, induction hardened and post-hardened PVD coated steel. Since the surface quality of the samples varied regionally, roughness measurements were taken from ten separate points for each sample and the average was taken. While the surface roughness of the non-heat treated and induction hardened samples was approximately 0.3, the surface roughness value decreased to 0.2 after PVD.

2.2. Wear test setup and conduct of the experiment

In this research, block-on-ring contact configuration was employed in the experimental setup due to its resemblance to the cam-follower mechanism as seen in Figure 4. This configuration provides a linear contact interface.

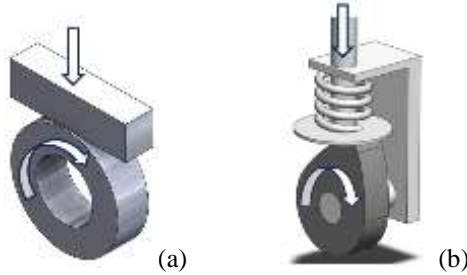


Figure 4. a) Block-on-ring wear test model and b) cam-follower mechanism

The wear tester used for the experiments is illustrated in Figure 5. Wear tests were carried out using a cam profile measuring device adapted as a wear tester.



Figure 5. Wear tester

During testing, external loads of 4 N, 8 N, and 12 N were applied. The spring used in the system has a constant of 5.4 kN/m. The spring force acting on the cam samples varies depending on the cam profile and consists of two components. The first component arises from the initial compression of the spring during assembly, corresponding to the spring force at the cam's bottom dead center. This force is incorporated into the total mechanism weight, which is fixed at 24 N for all tests. The second component results from the cam profile's displacement between the bottom and top dead centers—a distance of 8 mm. Figure 6 presents the total force applied to the specimen. The samples were prepared by Estaş company, a camshaft manufacturer, according to the dimensions given.

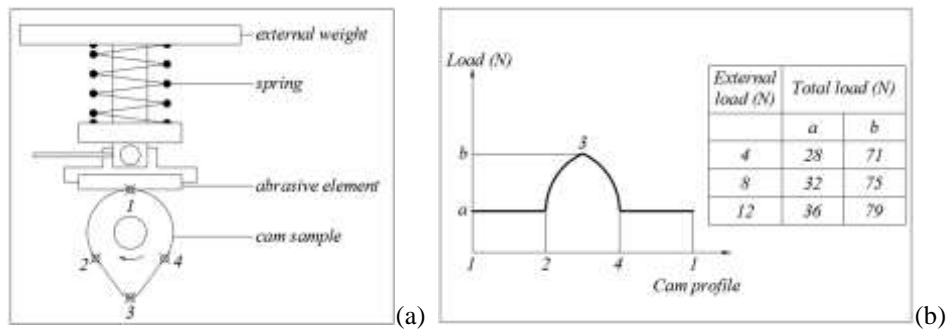


Figure 6. a) Schematic view of wear tester b) Force distribution on the cam sample in experimental setup

The cam sample and the abrasive counterface were weighed using a high-precision balance. For this procedure, an Axis brand balance with an accuracy of ± 0.1 mg which is shown in Figure 6 and housed in the Mechanical Engineering Laboratory at Sivas Cumhuriyet University, was employed. Calibration was performed using external weights. The experiment commenced after setting the rotational speed with a tachometer, and the friction distance corresponding to roughly one hour of operation was used as the reference. Once the desired friction distance was achieved, the machine was halted, and the weights of both the cam sample and the abrasive element were recorded using the same precision balance. This one-hour wear cycle was repeated twice more, with weight measurements and photographs taken after each cycle.

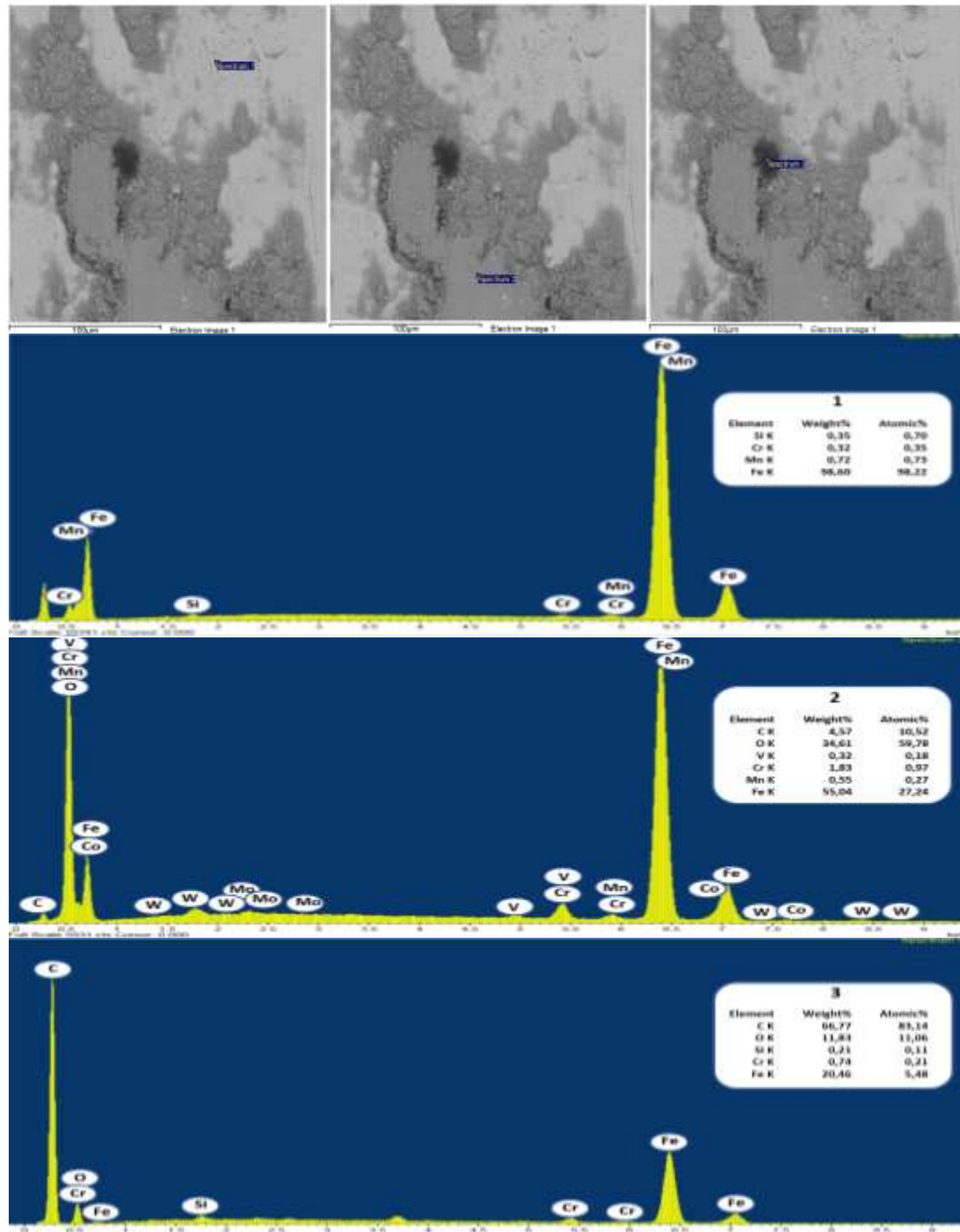


Figure 7. SEM image of the PVD coated sample after wear and EDX analysis taken from three different points

3. Results and Discussion

Following the wear tests, SEM imaging was conducted on the worn surfaces of the PVD-coated steel samples, and EDX analyses were carried out as displayed in Figure 7. The bright regions correspond to exposed, worn metal and are relatively hard. EDX results revealed a very small amount of chromium in these areas, suggesting that the PVD coating was worn away at those locations. Meanwhile, the dark regions, rich in carbon and oxygen, point to oxidation and thermal damage caused by frictional heating. Furthermore, given that the counterface material is high-speed steel, the presence of alloying elements such as cobalt (Co), vanadium (V), molybdenum (Mo), and tungsten (W) suggests material transfer through adhesive wear mechanisms.

Table 2. Wear losses of samples after (a) 1 hour, (b) 2 hours, (c) 3 hours

Velocity (rpm)	Load (N)	Non-heat treated (mg)	Hardened (mg)	PVD + Hardened (mg)
85	4	28.5	5.2	3.3
85	8	29.0	5.0	3.5
85	12	32.4	5.6	3.8
100	4	38.3	7.5	5.3
100	8	40.3	7.8	5.1
100	12	41.2	7.6	5.4
115	4	52.8	9.5	6.2
115	8	55.5	11.0	6.2
115	12	58.1	11.5	6.4
(a)				
Velocity (rpm)	Load (N)	Non-heat treated (mg)	Hardened (mg)	PVD + Hardened (mg)
85	4	55.5	11.7	7.5
85	8	55.0	13.5	8.0
85	12	58.4	13.3	8.2
100	4	69.2	14.4	9.2
100	8	75.6	15.6	9.8
100	12	74.5	17.8	9.5
115	4	90.8	17.4	10.2
115	8	93.1	17.7	10.1
115	12	98.1	19.0	10.8
(b)				
Velocity (rpm)	Load (N)	Non-heat treated (mg)	Hardened (mg)	PVD + Hardened (mg)
85	4	84.8	18.1	10.8
85	8	86.0	21.5	11.5
85	12	92.4	21.6	12.6
100	4	113.4	23.4	11.1
100	8	118.3	25.4	15.2
100	12	118.0	27.8	15.8
115	4	131.0	24.6	16.0
115	8	133.5	29.4	16.2
115	12	135.0	29.5	17.5
(c)				

The wear losses obtained at one-hour intervals for different rotational speeds and different external loads for steel with three different surfaces are given in Table 2 and Figure 8. In general, as the rotational speed and

external weight increased, the amount of wear also increased. However, only a few measurements showed results contrary to expectations. For example, in the hardened sample, wear under 8 N load at 100 rpm was measured as 7.8 mg after 1 hour, while in Table 2(a), wear under 12 N load was measured as 7.6 mg. Similarly, in the PVD-coated sample, wear under 8 N load at 100 rpm was measured as 9.8 mg and under 12 N load after 2 hours, wear was measured as 9.5 mg in Table 2(b). These samples returned to normal after 3 hours, i.e., the amount of wear increased as the load increased. In Table 2(c), only the amount of wear in the unheated sample was measured as 118.3 mg at 8 N and 118 mg at 12 N at 100 rpm after 3 hours. This situation can be interpreted as follows. While the external weight increases by 50%, the load on the sample increases from 32 N to 36 N in the circular area of the cam; and from 75 N to 79 N at the top of the cam, approximately 5%. Since these values are very small, it is normal to see such unexpected results.

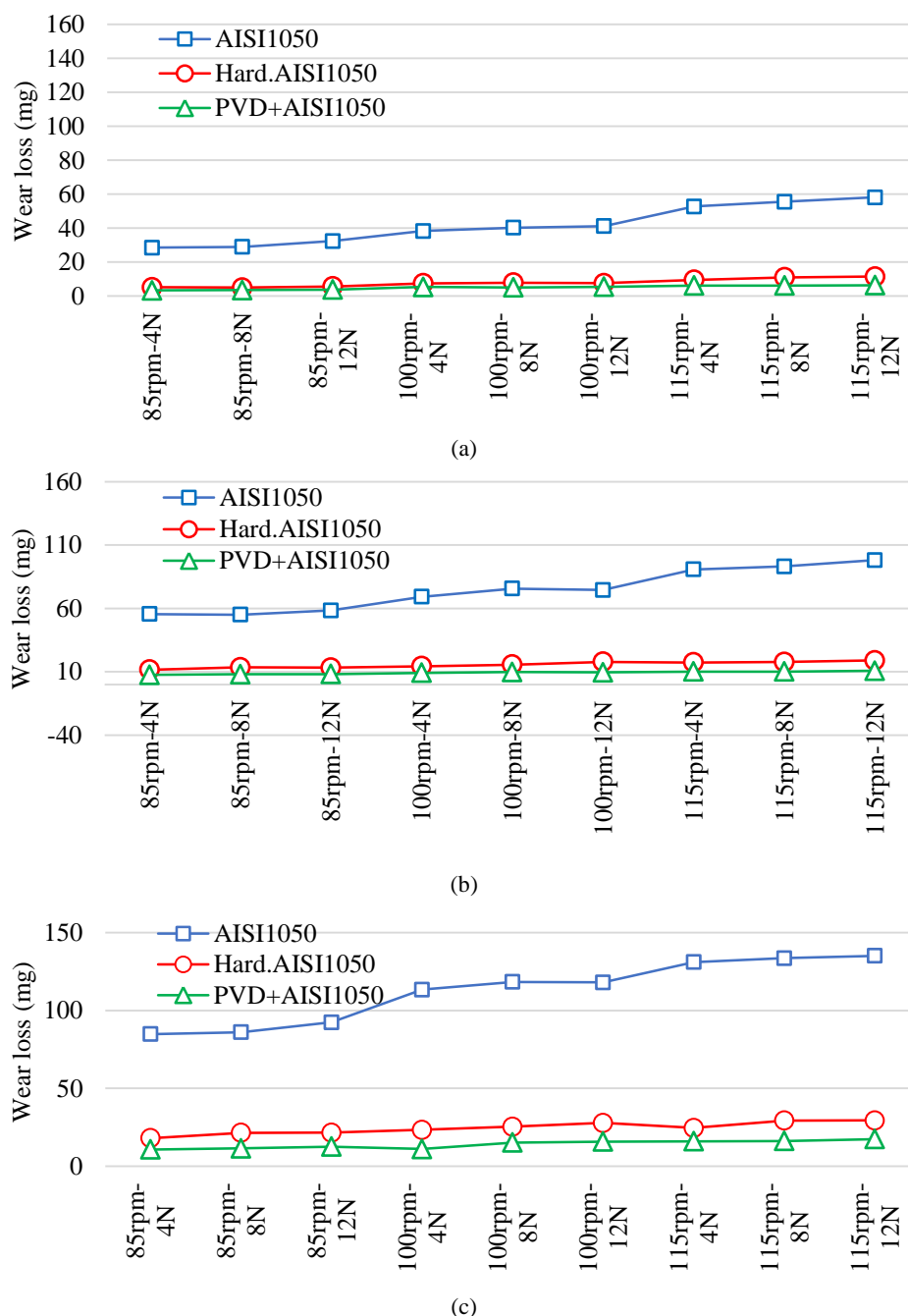


Figure 8. Wear losses of samples after (a) 1 hour, (b) 2 hours, (c) 3 hours

In the experiments, the wear in induction hardened steels compared to non-heat-treated steels was approximately 80% less, as calculated from Table 2. In order for the PVD coating to be applied, the surface must be somewhat hard. Therefore, induction hardening was performed before the PVD coating. When the PVD coating was calculated as induction hardened, Wang and his colleagues (2023) found similar results using the same coating material.

4. Conclusion

Normally, heat treated steels such as AISI 1050 without heat treatment are not used as materials for parts exposed to wear. It was used here only for comparison. In the experiments, wear in induction hardened steels was 80% less than in non-heat treated steels. When PVD coating was applied, surface roughness was reduced by approximately 30%, and wear was reduced by approximately 35% compared to induction hardened samples. If too much cost is not desired, induction hardening is satisfactory. However, if more hardness and longer life are desired, PVD coating will definitely meet the need.

Ethics Permissions

This paper does not require ethics committee approval.

Author Contributions

The topic was determined by Burhan Selçuk in his capacity as a consultant, who also oversaw the material selection. Ersin Arslanbulut performed the experiments and was responsible for writing the article.

Conflict of Interest

Authors declare that there is no conflict of interest for this paper.

References

- ASM International. (1990). *ASM Handbook, Volume 1: Properties and Selection: Irons, Steels, and High-Performance Alloys*. ASM International.
- Bhushan, B. (2013). *Introduction to Tribology*. (2nd ed.). Wiley.
- Dowson, D. (1998). *History of Tribology*. (2nd ed.) Professional Engineering Publishing.
- Gharbi, F., Kapsa, P., Nouveau, C., and Paulin, C. (2015). Influence of surface texturing on friction and wear under dry contact for automotive application. *Tribology International*, 89, 172–182.
- Holmberg, K., and Matthews, A. (2009). *Coatings Tribology: Properties, Mechanisms, Techniques and Applications in Surface Engineering*. (2nd ed.). Elsevier.
- Hutchings, I. M., and Shipway, P. (2017). *Tribology: Friction and Wear of Engineering Materials* (2nd ed.). Butterworth-Heinemann.
- Jahanmir, S., and Beltz, G. (2000). Wear mechanisms and modeling. *Wear*, 245(1–2), 53–67.
- Litvin, F. L., and Fuentes, A. (2004). *Gear Geometry and Applied Theory* (2nd ed.). Cambridge University Press.
- Podgornik, B., Vižintin, J., Hogmark, S., and Jacobson, S. (2004). Wear behaviour of hard coatings on soft substrates. *Wear*, 256(1–2), 168–175.
- Stachowiak, G. W., and Batchelor, A. W. (2005). *Engineering Tribology* (3rd ed.). Butterworth-Heinemann.
- Totten, G. E., and Howes, M. A. H. (1997). *Steel Heat Treatment Handbook*. CRC Press.
- Vöhringer, O. (2001). Changes in the mechanical properties of metals due to cryogenic treatment. *Cryogenics*, 41(3), 157–178.
- Wang, Y., Li, D., Nie, C., Gong, P., Yang, J., Hu, Z., Li, B., and Ma, M. (2023). Research progress on the wear resistance of key components in agricultural machinery. *Materials*, 16(24), 7646.
- Zhang, S., Li, X., and Zhang, X. (2011). Toughening of hard nanostructural thin films: A critical review. *Surface and Coatings Technology*, 204(11), 1832–1840.